FLUID STRUCTURE COUPLED ANALYSIS OF AN AERODYNAMIC SURFACE

A THESIS SUBMITTED TO
THE GRADUATE SCHOOL OF NATURAL AND APPLIED SCIENCES
OF
MIDDLE EAST TECHNICAL UNIVERSITY

BY

BÜLENT SÜMER

IN PARTIAL FULFILLMENT OF THE REQUIREMENTS
FOR
THE DEGREE OF MASTER OF SCIENCE
IN
AEROSPACE ENGINEERING

NOVEMBER 2004

Approval of the Graduate School of Natural and Applied Sciences

_____

Prof. Dr. Canan ÖZGEN

Director

I certify that this thesis satisfies all the requirements as a thesis for the degree of Master of Science.

_____

Prof. Dr. Nafiz ALEMDAROĞLU

Head of Department

This is to certify that we have read this thesis and that in our opinion it is fully adequate, in scope and quality, as a thesis for the degree of Master of Science.

_____	_____
Prof. Dr. İsmail H. TUNCER	Prof. Dr. Mehmet A. AKGÜN
Co-Supervisor	Supervisor

Examining Committee Members

Assoc. Prof. Dr. Yusuf ÖZYÖRÜK	(METU – AEE)	_____
Prof. Dr. Mehmet A. AKGÜN	(METU – AEE)	_____
Prof. Dr. İsmail H. TUNCER	(METU – AEE)	_____
Assoc. Prof. Dr. Altan KAYRAN	(METU – AEE)	_____
Asst. Prof. Dr. Serkan DAĞ	(METU – ME)	_____

I hereby declare that all information in this document has been obtained and presented in accordance with academic rules and ethical conduct. I also declare that, as required by these rules and conduct, I have fully cited and referenced all material and results that are not original to this work.

Name, Last name: Bülent SÜMER

Signature :

ABSTRACT

FLUID STRUCTURE COUPLED ANALYSIS OF AN AERODYNAMIC SURFACE

Sümer, Bülent
M.Sc., Department of Aerospace Engineering
Supervisor: Prof. Dr. Mehmet A. AKGÜN
Co-Supervisor: Prof. Dr. İsmail H. TUNCER

November 2004, 144 pages

In this thesis a 3-D Euler flow solver is coupled with a finite element program in order to solve static aeroelastic problems involving aircraft wings. A loosely coupled approach based on an iterative solution procedure is used to solve the coupled field problem. Because of deformation of the underlying structure over which the flow is solved, Computational Fluid Dynamics mesh has to move at each computational aeroelastic iteration in order to conform to the new shape of the aerodynamic surface. As a part of this work, a procedure is developed in order to move fluid grid points, which views the whole computational domain as an isotropic elastic medium and solves it using finite element method. A matching discrete interface is defined; displacement and pressure data exchange is accomplished at this interface. AGARD Wing 445.6 and an elastic supercritical

wing is modeled and solved with the developed computational procedure and the obtained results are compared with numerical and wind tunnel data.

Keywords: Computational Aeroelasticity, Computational Fluid Dynamics, Finite Element Analysis, Loosely Coupled Approach, AGARD Wing 445.6.

ÖZ

AERODİNAMİK BİR YÜZEYİN AKIŞKAN KATI ETKİLEŞİMLİ ANALİZİ

Sümer, Bülent
Y.Lisans, Havacılık ve Uzay Mühendisliği Bölümü
Tez Yöneticisi: Prof. Dr. Mehmet A. AKGÜN
Ortak Tez Yöneticisi: Prof. Dr. İsmail H. TUNCER

Kasım 2004, 144 sayfa

Bu tezde kanat üzerindeki durağan aeroelastisite problemlerini çözmek amacıyla üç boyutlu bir Euler akış çözücüsü ile bir sonlu elemanlar programı birleştirilmiştir. Birleştirilmiş alan problemini çözmek için tekrarlı bir çözüm prosedürüne dayalı gevşek bağlı yaklaşım kullanılmıştır. Akışın çözüldüğü yüzey altındaki yapının deformasyonu sebebiyle Hesaplamalı Akışkanlar Dinamiği çözüm ağı her bir hesaplamalı aeroelastik tekrarlama sonrasında aerodinamik yüzeyin yeni şekline uyacak şekilde hareket ettirilmelidir. Bu çalışmanın bir parçası olarak akışkan çözüm ağı noktaları hareket ettirmek amacıyla, bütün çözüm alanını izotropik elastik bir ortam olarak görüp sonlu elemanlar metoduyla çözen bir prosedür geliştirilmiştir. Eşleşmeli bir arayüz tanımlanmış, basınç ve yer değiştirme verilerinin alışverişi bu arayüzde yapılmıştır. AGARD 445.6 kanadı ve Elastik

süperkritik bir kanat modellenmiş ve geliştiren hesaplama yöntemi ile çözülmüş, elde edilen sonuçlar sayısal veriler ve rüzgar tüneli verileri ile karşılaştırılmıştır.

Anahtar Kelimeler: Hesaplamalı Aeroelastisite, Sonlu Eleman Analizi, Hesaplamalı Akışkanlar Dinamiği, Gevşek Bağlı Yaklaşım, AGARD 445.6 Kanadı.

To my family

ACKNOWLEDGEMENTS

I would like to express my appreciation to my advisor Prof. Dr. Mehmet A. Akgün for his prompt responses to my questions and submitted work, understanding and guidance throughout the study. I am grateful to Prof. Dr. İsmail H. Tuncer for his guidance, support, and encouragement.

I wish to thank Dr. Mehmet Ali Ak and Mr. L. Oktay Gönç for their invaluable support and discussion on the subject. I would like to thank my brother Bilsay for finding some of the reference papers, and my friends, especially to Mr. Özgür Demir, for his great friendship and support.

Finally, I would like to thank Özlem for her understanding, patience and support.

TABLE OF CONTENTS

PLAGIARISM…….. iii

ABSTRACT…….. iv

ÖZ…….. vi

ACKNOWLEDGEMENTS……. ix

TABLE OF CONTENTS……. x

LIST OF TABLES……... xiii

LIST OF FIGURES……. xiv

LIST OF SYMBOLS……... xviii

CHAPTERS

1. INTRODUCTION…… 1

1.1 FINITE ELEMENT METHOD FOR STRUCTURAL ANALYSIS…….... 3

1.2 COMPUTATIONAL FLUID DYNAMICS METHOD FOR AERODYNAMIC ANALYSIS…… 4

1.3 COMPUTATIONAL AEROELASTICITY…….. 5

1.4 CFD MESH DEFORMATION……. 5

1.5 LITERATURE REVIEW…….. 5

2. DEFORMATIONS OF AIRCRAFT WINGS AND COMPUTATIONAL AEROELASTIC PROCEDURE……... 10

2.1 DEFORMATIONS OF AIRCRAFT WINGS AND THE CONCEPT OF ELASTIC AXIS…… 10

2.1.1 Elastic Axis…… 13

2.2 STATIC AEROELASTIC PHENOMENA……... 14

2.3 COMPUTATIONAL AEROELASTIC PROCEDURE…… 17

2.4 COUPLED FIELD SOLUTION OF STATIC AEROELASTIC PROBLEM…… 20

2.5 FLOW SOLVER- SET3D…….. 21

2.5.1 Governing Equations…….. 21

2.5.2 Numerical Method, Upwind Differencing and Time Integration…….... 23

2.5.3 Geometry and Grid Generation……..... 24

2.5.4 Implementation of Boundary Conditions……... 27

2.6 STRUCTURE SOLVER-ANSYS…….. 28

2.6.1 Governing Equations…….. 28

2.6.2 Finite Element Method and ANSYS Finite Element Solver…….. 29

2.6.3 ANSYS Finite Elements Used in Structural Analysis…… 30

2.7 CFD GRID DEFORMATION METHOD…… 33

2.7.1 A Finite Element Based Method for Grid Deformation……. 37

2.8 LOAD AND MOTION TRANSFER METHODS……..…….. 46

2.8.1 Motion Transfer Method……..……... 48

2.8.2 Load Transfer Method……..……... 49

2.9 COUPLING ENVIRONMENT, ANSYS INPUT FILES AND PERL SCRIPTING LANGUAGE……... 50

3. TEST CASE I – AGARD WING 445.6…….. 52

3.1 INTRODUCTION…….. 52

3.2 AGARD WING 445.6 CFD ANALYSIS ……..…… 56

3.2.1 Grid Sensitivity Study…… 56

3.2.2 CFD Analysis- Comparison of Results……..…… 76

3.3 AGARD WING 445.6 MODAL ANALYSIS……... 80

3.4 AGARD WING 445.6 STATIC AEROELASTIC ANALYSIS ……... 89

4. TEST CASE II- AEROELASTIC RESEARCH WING 2 (ARW-2)….. 100

4.1 INTRODUCTION……... 100

4.2 ARW-2 WIND TUNNEL MODEL DEFINITION AND STRUCTURAL PROPERTIES……... 101

4.2.1 Wind Tunnel Model……... 101

4.2.2 Wing Structural Properties……..... 101

4.3 ARW-2 FINITE ELEMENT MODEL …….. 103

4.3.1 1-D Finite Element Model of the Wing……..... 103

4.3.2 3-D Finite Element Model of the Wing ……..... 106

4.4 ARW-2 COMPUTATIONAL FLUID DYNAMICS MODEL…….. 113

4.5 ARW-2 STATIC AEROELASTIC ANALYSIS…….…….. 115

5. CONCLUSION AND RECOMMENDATIONS……... 124

REFERENCES……. 127

APPENDICES

A. ANSYS INPUT FILE FOR DEFINING THE MATERIAL PROPERTIES OF CFD COMPUTATIONAL DOMAIN……... 133

B. PERL SCRIPT……. 134

C. ANSYS INPUT FILE FOR STRUCTURAL ANALYSIS……... 136

D. ANSYS INPUT FILE FOR CFD GRID DEFORMATION ANALYSIS……... 143

LIST OF TABLES

TABLE

3.1	Mechanical Properties of Laminated Mahogany…….	55
3.2	Mechanical Properties for the Weakened AGARD Wing 445.6 ……	56
3.3	Number of Triangles and Nodes for Different CFD Grids……..	59
3.4	Number of Field Elements and Nodes for Different CFD Grids…….	60
3.5	Number of SOLID187 Elements used in Finite Element Models……..	82
3.6	Calculated Natural Frequencies for Weakened AGARD Wing 445.6….	83
3.7	Percent Error Values for Finite Element Models…….	83
3.8	Comparison of Minimum Deflection Values……...	84
3.9	Comparison of Rigid Wing and Elastic Wing Lift Coefficients……..	91
4.1	Bending and Torsional Stiffness Values for 1-D Finite Element Model.	103
4.2	Deflection and Angle of Twist Values for 1-D Finite Element Model…	106
4.3	Comparison of Bending Deflections of 1-D Model and 3-D Model…...	111
4.4	Comparison of Angle of Twist of 1-D Model and 3-D Model……	111
4.5	Relative Angle of Twist Error in Bending……...	112
4.6	Relative Angle of Twist Error in Torsion……	112

LIST OF FIGURES

FIGURE

1.1 Varying Levels of Accuracy in Modeling Fluids and Structures..... 2

2.1 Airplane Wing under Distributed Side Load……... 12

2.2 Elastically Supported Rigid Airfoil Section……. 14

2.3 Streamwise and Chordwise Segments of Swept Wing…… 16

2.4 Flowchart of the Computational Aeroelastic Procedure…….. 19

2.5 Loosely Coupled Approach……. 20

2.6 Mapped and Free Surface Triangulations…… 24

2.7 Solution Domain Divided into Smaller Computational Volumes and Resulting Computational Domain…….. 26

2.8 ANSYS SOLID187 Element……... 31

2.9 ANSYS SHELL63 Element……. 32

2.10 ANSYS BEAM4 Element…… 33

2.11 Spring Analogy Method for CFD Grid Deformation……... 35

2.12 Torsional Spring Analogy Method for CFD Grid Deformation…….. 36

2.13 ANSYS SOLID45 Element…….…… 38

2.14 Geometry of the Solution Domain for NACA0012 Airfoil……. 39

2.15 Computational Grid for NACA0012 Airfoil ……... 39

2.16 Deformed and Undeformed Computational Domains near Airfoil Geometry…… 41

2.17 Undeformed Computational Domain (A Close Look at Leading Edge).. 41

2.18 Deformed Computational Domain (A Close Look at Leading Edge)….. 42

2.19 Undeformed Computational Domain (A Close Look at Trailing Edge).. 42

2.20 Deformed Computational Domain (A Close Look at Trailing Edge)….. 43

2.21 Deformed Computational Domains with n=2 and n=6…… 44

2.22 Deformed Computational Domain Leading Edge n=2 ……... 45

2.23 Deformed Computational Domain Trailing Edge n=2…… 46

2.24 Fluid and Structure Meshes with Non-Matching Interfaces…… 47

2.25 Fluid and Structure Meshes with Matching Interfaces……..... 48

2.26 Pressure Distribution over a Triangular Element……..... 50

3.1 AGARD Wing 445.6 Planform…… 52

3.2 Solid AGARD Wing 445.6…….. 53

3.3 Weakened AGARD Wing 445.6…….. 54

3.4 Dimensions of the Computational Domain…….. 57

3.5 Half Cylinder Computational Domain……. 57

3.6 Wing Surface Triangulations……... 58

3.7 Unstructured Volume Grids……. 59

3.8 Wing Cp Distribution at 34 % Semispan (M=0.85 $\alpha=5^{o}$)…… 61

3.9 Wing Cp Distribution at 67 % Semispan (M=0.85 $\alpha=5^{o}$)…… 62

3.10 Pressure Coefficient Contours over AGARD Wing 445.6 (M=0.85 $\alpha=5^{o}$)……... 63

3.11 Wing Cp Distribution at 26 % Semispan (M=0.96 $\alpha=0^{o}$)…… 64

3.12 Wing Cp Distribution at 50.4 % Semispan (M=0.96 $\alpha=0^{o}$)…… 65

3.13 Wing Cp Distribution at 75.5 % Semispan (M=0.96 $\alpha=0^{o}$)……. 67

3.14 Pressure Coefficient Contours over AGARD Wing 445.6 (M=0.96 $\alpha=0^{o}$)……... 68

3.15 Mach Contours over AGARD Wing 445.6 (M=0.96 $\alpha=0^{o}$)……. 69

3.16 Wing Cp Distribution at 26 % Semispan (M=1.141 $\alpha=0^{o}$)…….. 70

3.17 Wing Cp Distribution at 50.4 % Semispan (M=1.141 $\alpha=0^o$)…….. 71

3.18 Wing Cp Distribution at 75.5 % Semispan (M=1.141 $\alpha=0^o$)…….. 73

3.19 Pressure Coefficient Contours over AGARD Wing 445.6 (M=1.141 $\alpha=0^o$)……... 74

3.20 Mach Contours over AGARD Wing 445.6 (M=1.141 $\alpha=0^o$)…….. 75

3.21 Comparison of Cp Distribution at 34 % Semispan (M=0.85 $\alpha=5^o$)……. 77

3.22 Comparison of Cp Distribution at 67 % Semispan (M=0.85 $\alpha=5^o$)……. 77

3.23 Comparison of Cp Distribution at 26 % Semispan (M=1.141 $\alpha=0^o$)….. 79

3.24 Comparison of Cp Distribution at 50.4 % Semispan (M=1.141 $\alpha=0^o$)… 79

3.25 Comparison of Cp Distribution at 75.5 % Semispan (M=1.141 $\alpha=0^o$)… 80

3.26 Finite Element Models of AGARD Wing 445.6…….. 81

3.27 Mode Shape 1……... 85

3.28 Mode Shape 2……... 86

3.29 Mode Shape 3……... 87

3.30 Mode Shape 4……... 88

3.31 Convergence History for Rigid and Elastic Wings…….. 90

3.32 Lift Coefficients for Rigid and Elastic Wings……. 90

3.33 Elastic and Rigid Wing Cp Distributions at 34 % Span…….. 92

3.34 Elastic and Rigid Wing Cp Distributions at 67 % Span…….. 92

3.35 Elastic and Rigid Wing Non-dimensional Pressure Contours……. 93

3.36 Comparison of Elastic Wing Cp Distribution at 34 % Span…… 94

3.37 Comparison of Elastic Wing Cp Distribution at 67 % Span…… 94

3.38 Initial and Equilibrium Positions of AGARD Wing 445.6…….. 95

3.39 Leading Edge Out-of-Plane Deformation of AGARD Wing 445.6……. 96

3.40 Trailing Edge Out-of-Plane Deformation of AGARD Wing 445.6……. 97

3.41 Equivalent Von-Misses Stress Distribution on AGARD Wing 445.6…. 98

4.1 ARW-2 Wing Platform…… 100

4.2 Calculated and Measured Torsion and Bending Stiffness Data..... 102

4.3 1-D Wing Finite Element Model …… 104

4.4 1-D Wing Finite Element Model under 100 lb Tip Load ……... 105

4.5 1-D Wing Finite Element Model under 100 lb.in. Tip Torque ……... 105

4.6 3-D Wing Geometry……. 107

4.7 3-D Wing Finite Element Model …… 107

4.8 3-D Wing Model with 100 lb Load at the Tip……. 110

4.9 Dimensions of the Computational Domain…….. 114

4.10 Wing Surface Triangulation……..... 114

4.11 Unstructured Volume Grid……... 115

4.12 Lift Coefficient for Rigid and Elastic Wings……... 116

4.13 Convergence History for Rigid and Elastic Wings…….. 116

4.14 Non-dimensional Pressure Contours Over Rigid Wing……... 117

4.15 Non-dimensional Pressure Contours Over Elastic Wing……. 117

4.16 Pressure Coefficient Distribution at 23.4 % Semispan……... 118

4.17 Pressure Coefficient Distribution at 47.6 % Semispan……... 118

4.18 Pressure Coefficient Distribution at 59.9 % Semispan……... 119

4.19 Pressure Coefficient Distribution at 70.7 % Semispan……... 119

4.20 Pressure Coefficient Distribution at 87.1 % Semispan……... 120

4.21 Pressure Coefficient Distribution at 97.2 % Semispan…… 120

4.22 Initial and Equilibrium Positions of ARW-2……... 121

4.23 Initial and Equilibrium Positions of ARW-2 (View from Trailing edge) 122

4.25 Comparison of Front Spar Shapes M=0.8 q_∞=100 psf $\alpha=0^o$…… 122

4.26 Comparison of Rear Spar Shapes M=0.8 q_∞=100 psf $\alpha=0^o$……. 123

LIST OF SYMBOLS

a	Speed of sound
A_i	Area of element i
AGARD	Advisory Group for Aerospace Research and Development
ALE	Arbitrary Lagrangian Eulerian
ARW-2	Aeroelastic Research Wing-2
B	Body Force per Unit Mass
c	Chord Length
C	Material Constant
C_{ij}	Flexibility Influence Coefficient
$C_{\theta\theta}$	Torsional spring Flexibility Influence Coefficient
CAE	Computational Aeroelasticity
CFD	Computational Fluid Dynamics
CFL	Courant-Friedrich-Levy Number
C_L	Lift Coefficient
C_{LR}	Rigid Wing Lift Coefficient
C_{LE}	Elastic Wing Lift Coefficient
C_{MAC}	Wing Moment Coefficient about the Aerodynamic Center
C_P	Pressure Coefficient
C_{Pmax}	Maximum Pressure Coefficient
[D]	Damping Matrix
DAST	Drones for Aerodynamic and Structural Testing
e	Distance between Elastic Axis and Aerodynamic Center

E_i	Elasticity Modulus of element i
EI	Bending Stiffness
F	Convective Flux Vector
FVM	Finite Volume Method
FDM	Finite Difference Method
{F}	Force Vector
G_i	Shear modulus of element i
GJ	Torsional stiffness
M	Mach Number
[K]	Stiffness Matrix
[M]	Mass Matrix
n	Unit Normal Vector associated with a face
numel	Number of elements
p	Non-dimensional Pressure
rot_x	Rotation along x-axis
q	Deflection
q_∞	Freestream Dynamic Pressure
Q	Applied Force
Q	Fluid Solution Vector
S	Area of the Wing Segment
T	Aerodynamic Moment about the Elastic Axis
T	Non-dimensional temperature
TDT	Langley Transonic Dynamics Tunnel
u	displacement
u, v, w	Velocity components in x, y, and z directions
u_y	Translation in y direction

$\{u\}$	Displacement Vector
V_i	Volume of Element i
$Z(x,y)$	Distributed Force
x, y, z	Cartesian Coordinates
$w(x,y)$	Deformation of Elastic Wing Under the Influence of a Distributed Force
$w(y)$	Bending Displacement
w.o.z	Wind-off zero
α	Angle of Attack
α^r	Rigid Angle of Attack
θ	Elastic Twist
$\theta(y)$	Twisting Displacement
γ	Specific Heat Ratio, C_P/C_V
ε_{ij}	Strain Tensor
η	Fraction of Wing Semispan
ρ	Non-dimensional Density
ρu	Non-dimensional Momentum in x-direction
ρv	Non-dimensional Momentum in y-direction
ρz	Non-dimensional Momentum in z-direction
ρe_o	Non-dimensional Energy
λ,μ	Lame's Constants
Ω	Finite Volume – Domain of Integration
Γ_m	Moving Boundary

CHAPTER 1

INTRODUCTION

The main objective of this thesis is to couple a high-fidelity Computational Fluid Dynamics (CFD) solver with a high-fidelity Finite Element solver in order to solve static aeroelasticity problems involving aircraft wings.

Aeroelastic problems would not exist if airplane structures were perfectly rigid. Modern airplanes are flexible and this flexibility is the fundamental cause of various types of aeroelastic phenomena [1]. Problems with strong coupling between steady aerodynamics and steady structural deformations are generally referred to as static aeroelastic problems [2]. Wing divergence, elastic load distribution, control effectiveness, control system reversal are some of the fields in which the interaction of aerodynamic and elastic forces become important.

During high-speed flight, deflections of structures tend to redistribute the air loads, and may cause their distribution to be significantly different from that computed on the assumption of complete rigidity. It is important to predict this redistribution and design structural members accordingly [1].

Several methods have been developed to solve fluid and structure problems separately. Fluid problems can be solved using linear analytical methods with low accuracy or they can be solved using Navier/Stokes equations with high accuracy. Similarly structural problems can be solved with shape functions with low accuracy or they can be solved with detailed 3-D finite elements with high accuracy. As the

level of accuracy increases, complexity in physics and geometry increases. Figure 1.1 illustrates the typical levels of modeling complexities involved for both fluids and structures.

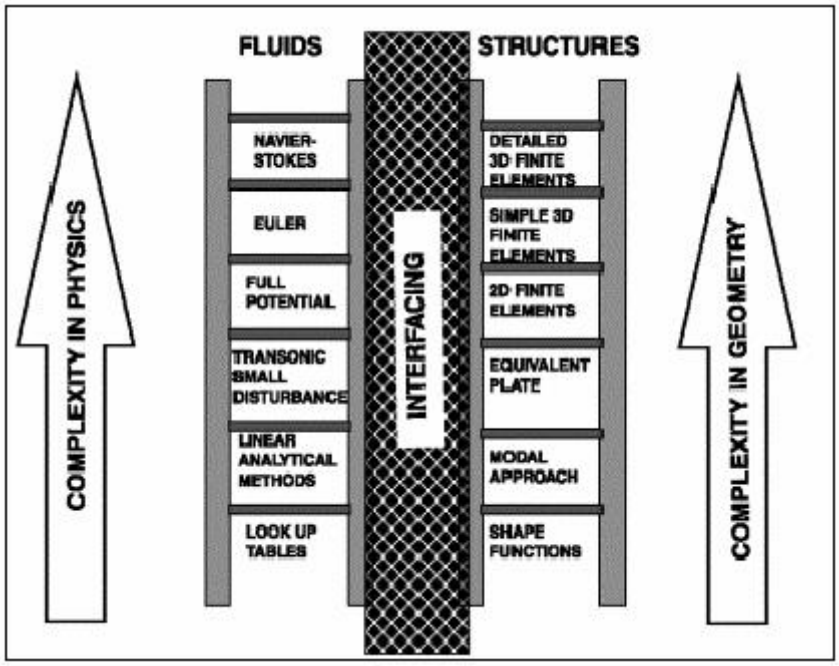

Figure 1.1 Varying Levels of Accuracy in Modeling for Fluids and Structures [3]

However, the nature of aeroelastic problems calls for a coupling between two systems. Methods for coupling a fluid system and a structure system by using low-accuracy methods are well advanced [3]. These predictions can be used in the preliminary design stage. However, more accurate predictions such as Euler

solutions for fluids and finite element solutions for structures are needed for detailed design stage.

The flow over the wing of a fighter aircraft operating in transonic regime can not be modeled by linear theories, because of the existing strong shocks and flow separations, which cause drastic changes in the pressure distribution over the wing surface.

On the other hand, the increase in the use of composite materials in aerospace structures, the research for aeroelastic tailoring in order to achieve desired aerodynamic characteristics, and the stress constraints for an optimization problem call for a more detailed representation of a structural system.

1.1 FINITE ELEMENT METHOD FOR STRUCTURAL ANALYSIS

"The limitations of human mind are such that it can not grasp the behavior of its surroundings in one operation. Thus the process of subdividing all systems into their components or 'elements', whose behavior is readily understood, and then rebuilding the original system from its components to study its behavior is a natural way in which the engineer or the scientist proceeds" [4].

Zienkiewich [4] explains why the finite element method is required for structural analysis with the above words. In solid mechanics, closed form solutions of partial differential equations are available for limited number of problems. Most of the problems cannot be solved with the analytical methods. So the continuum is divided into a finite number of elements (finite elements). The problem is solved for each and every one of these elements. At the end, the governing partial differential equations turn into a set of algebraic equations.

Aerospace structures consisting of spars, ribs, skin panels and stiffeners, with arbitrary loading conditions, can be easily modeled and solved using the finite element method.

In recent years commercial Finite Element Analysis programs (ANSYS, NASTRAN, ABAQUS, etc) implementing the finite element method in order to solve structural mechanics problems have become widespread. The types of problems that can be solved with these programs are open ended. Some of the above mentioned programs even have formal optimization routines embedded into the finite element solver.

1.2 COMPUTATIONAL FLUID DYNAMICS METHODS FOR AERODYNAMIC ANALYSIS

CFD Methods are used to solve external flow problems over aeronautical vehicles and internal flow problems. These methods have the ability to capture the nonlinear behavior of aerodynamics in the transonic regime and, therefore, accurately predict load distribution over lifting bodies.

CFD methods also call for the discretization of a continuum. The Finite Volume (FVM) and Finite Difference Methods (FDM) are the most commonly used methods in solving the partial differential equations associated with fluid flow over arbitrary bodies. But the FVM have the unique advantage over the FDM in that the continuum can be divided into finite volumes in an unstructured fashion, yet structured meshes can also be used.

Using a structured or unstructured discretization of the continuum and the finite volume method, even the most complicated viscous Navier-Stokes equations with turbulent models can be solved in reasonable accuracy.

1.3 COMPUTATIONAL AEROELASTICITY

When CFD methods are coupled with structural mechanics in computational process, it is generally referred to as Computational Aeroelasticity (CAE) [5].

Computational Aeroelasticity is divided into two major classifications; Coupled Analysis and Uncoupled Analysis. Coupled analysis is further divided as fully coupled and loosely coupled analyses. In uncoupled analysis, the fluid system and structural system are treated as two separate modules with only external interaction between them. In fully coupled analysis, the governing equations for fluids and structures are combined into one set of equations and these equations are solved simultaneously. In the loosely coupled analysis, the fluid system and structural system are modeled and solved using separate tools and coupling is achieved by exchanging information at the fluid/structure interface.

1.4 CFD MESH DEFORMATION

In CAE studies, the computational grid for the flow solution has to be deformed so that it conforms to the deformed shape of the structure. In most of the approaches the deforming mesh algorithm is embedded in the fluid solver and the coupled aeroelastic problem viewed as a two-field problem, the fluid field and the structure field. Farhat et al. has formulated the moving mesh as a pseudo-structural system with its own dynamics, and formulated the coupled transient aeroelastic problem as a three-field rather than two-field problem: the fluid, the structure and the dynamic mesh [7, 8].

1.5 LITERATURE REVIEW

In this section a detailed literature review of computational aeroelasticity approaches is given.

Felker [9, 10] used 2-dimensional Navier-Stokes Equations and a finite element model to solve the coupled aeroelasticity problem over a transonic convergent-

divergent nozzle. The discretized fluid and structure equations are regarded as a single set of coupled nonlinear algebraic equations and solved with Newton-Raphson Method. The walls of the nozzle were modeled using two dimensional beam elements, and assumed to be cantilevered from the inlet. As the flexibility of the nozzle walls come in to the scene, some convergence problems was encountered with respect to the rigid wall case.

Bendiksen [11] treated the entire fluid-structure system as a continuum dynamics problem by using an Arbitrary Lagrangian Eulerian (ALE) formulation. He switched from Eulerian description to Lagrangian description at the fluid structure interface. He used the formulation in order to model the transonic wing flutter of typical sections with camber bending and the flutter behavior of cascaded airfoils.

Schuster et al. [12] used the Lockheed Martin Three-Dimensional Euler/Navier-Stokes Code (ENS3D) and a structural influence coefficient model to solve the static aeroelastic phenomena over a fighter model. In order to deform the grid, they adopted a simple algebraic shearing procedure that preserves the initial quality of the grid.

Guruswamy and Byun coupled the flow solver ENSAERO with the plate finite elements and shell finite elements in order to solve dynamic aeroelasticity problems. A shell/plate finite element was model directly coupled with an Euler/Navier-Stokes solver for the first time in this study. An analytical moving grid technique is used to deform the aerodynamic grid based on the structural deflections at the end of each time step. A virtual surface method is used to transfer aerodynamic loads and structural deformations from one domain to another. The results were compared with the validated modal analysis methods. The Finite Element approach gives displacements about 0.1 % higher than the modal approach [13, 14].

MacMurdy et al. modeled a wing box structure with membrane, shear panel and truss finite elements and coupled them with a 3-D Navier-Stokes solver, ENSAERO, to solve the static aeroelastic problem. The structural modeling was based on the ANALYZE program but the entire code was rewritten as a set of subroutines and incorporated into ENSAERO. The aerodynamic grid was deformed according to the motion of the wing using the leading edge displacement and the twist angle distribution along the span. The aerodynamic loads were calculated at the fluid grid points and transformed to structural nodes. Errors occurred due to the load transfer algorithm used, mainly due to the dissimilar aerodynamic and structural model platforms. The aeroelastic iterations were turned on after a rigid wing solution was obtained, a spike occurred on CFD residual upon the start of aeroelastic iterations. Aeroelastic iterations continued until the CFD residuals drop back to rigid wing solution residuals [15].

Robinson et al. [16] incorporated the aeroelastic equations of motion within an unsteady Euler/Navier-Stokes code, CFL3D. The equations of motion were derived by assuming that the general motion of a wing is described by a separation of time and space variables in a finite modal series. They developed and implemented a deforming mesh algorithm to move the fluid mesh so that it continuously conforms to the instantaneous shape of the aeroelastically-deforming wing. The deforming mesh algorithm was based on a network of interconnected springs in each edge of a hexahedral cell. The stiffness of the springs was modeled as inversely proportional to the length of the edge. As a result, the collision of any two vertices of an element was prevented in large motions, but this method fails in large amplitude motions in that it does not take into account a vertex crossing the edge facing it.

The main deficiency in the lineal spring analogy for two dimensional (three dimensional) modeling is that the stiffness of the edges is related neither to the areas (volumes) of the connected triangles (tetrahedrons), nor to the angles of these triangles (tetrahedrons). Whether attached to the edge of a triangle in two

dimensions or that of a tetrahedron in three dimensions, a lineal spring with a stiffness coefficient that varies inversely proportionally to the length of the edge which it is connected to can not prevent a vertex to edge or vertex to face penetration. Farhat et al. took the spring network methodology of Batina and added torsional springs at each edge of a cell to prevent a vertex colliding with the edge(s) (faces) facing it [17, 18].

Newman III et.al. solved the static aeroelastic problem over a 20 m span wing which has NACA 0012 airfoil at every wing section. Aerodynamic analysis was based on solving the Euler equations on unstructured tetrahedral meshes. The aerodynamic grid consisted of 18856 field cells and 2116 boundary faces. The structure of the wing was modeled using finite elements. Some interaction parameters were proposed in order to increase the efficiency of the coupling procedure. The geometry of the wing and some structural properties were well defined but this study cannot be used for validation purposes in the present study since the wing inner structural details were not given in the paper [19].

There are some recent efforts to predict the static aeroelastic characteristics of transonic transport models using CFD coupled with structural plate technique [20]. A steady-state unstructured-grid Euler flow solver (USM3D) coupled with an interacting boundary layer was used to obtain flow solutions. Roe's upwind flux splitting was used for inviscid flux computations across cell faces. Static aeroelastic deformations were calculated relative to the unloaded wing shape by using an equivalent plate method. The Rayleigh-Ritz technique was employed in equivalent plate solver in order to obtain the structural solution for a specified wing load distribution. The overall lift coefficient was overpredicted by a small amount when compared with the wind tunnel data.

Wind tunnel experiments were made on AGARD Wing 445.6 in order to predict the dynamic response characteristics and the flutter boundary [21]. There were

numerous efforts to solve flutter characteristics of AGARD Wing 445.6 with CAE methods [22, 23]. Static aeroelastic characteristics of AGARD Wing 445.6 were also studied by some researchers [24, 25]. AGARD Wing 445.6 is used as a test case in the present study.

Besides the computational efforts to accurately predict the aeroelastic characteristics of elastic bodies in fluid flow, both wind tunnel tests and flight tests have also been conducted.

In the late 70's NASA initiated a test program, namely Drones for Aerodynamic and Structural Testing (DAST), which uses an unmanned target drone aircraft for special high-risk flight tests and provides a test method that is a strong complement to wind tunnel and full scale piloted testing [26]. Aeroelastic Research Wing-2 (ARW-2), which was used in DAST program, provided a focus for studies on the benefits and applicability of multiple-active controls for fuel conservative transport type aircraft.

A delay in the NASA program DAST made the ARW-2 available for testing in the Langley Transonic Dynamics Tunnel (TDT). Numerous tests were conducted in TDT with ARW-2; both steady and unsteady pressure measurements were made in order to provide an early assessment of the wing aeroelastic stability over a wide range of angle of attack and wind tunnel data comparison with planned flight test data [27, 28, and 29].

Close range photogrammetric measurements were also made for the lower surface of the ARW-2. The measurements were made during wind-tunnel tests of quasi-steady pressure distributions on the wing. Representative data were presented as a graphical overview to show variations and trends of spar deflections with test variables. Comparative test data were presented for photogrammetric and cathetometric results of measurements of the wing tip deflections [30, 31]. The ARW-2 is used as a test case in the present study.

CHAPTER 2

DEFORMATIONS OF AIRCRAFT WINGS AND THE COMPUTATIONAL AEROELASTIC PROCEDURE

All aircraft parts are prone to structural deformations; wings, fuselage, empennage, etc. The deformation of an airframe depends on inertial loading distribution and surface loading distribution as well as on structural stiffness distribution.

The main difficulty in analyzing the effects of structural deformation is the mutual interaction between deformation and the aerodynamic lift; a wing deformation changes the wing shape, which affects the aerodynamic loading, which in turn affects the wing deformation.

In this chapter, a brief introduction to deformations of elastic wing and the static aeroelastic phenomena is given, then the numerical methods employed in order to solve the present aeroelastic problem are explained.

2.1 DEFORMATIONS OF AIRCRAFT WINGS AND THE CONCEPT OF ELASTIC AXIS

The geometry of an aerodynamic surface varies widely in shape. The wing shape can be of a high aspect ratio, which resembles slender beams, or like a delta wing, which resembles plates.

Under the assumption of a perfectly elastic structure, experiments have indicated that an applied force, Q, and its resulting deflection, q, are related by

$$q = C.Q \tag{2.1}$$

C is a constant of proportionality. Since the load and deflection are linearly dependent, the resulting structure may be handled as a linear system.

For linear systems, in which the principle of superposition applies, the total linear and angular deflection at any point can be expressed as the sum of the deflections at that point produced by individual forces and moments.

In the general case of an aircraft at which various loads and moments act on the structure, the total linear or angular deflection at any point can be expressed as the sum of deflections at that point produced by the individual forces and moments. Applying the principle of superposition the displacement of the point of application of the i^{th} force due to n forces is given by

$$q_i = \sum_{j=1}^{n} C_{ij}.Q_j \tag{2.2}$$

where the constants C_{ij} are called flexibility influence coefficients.

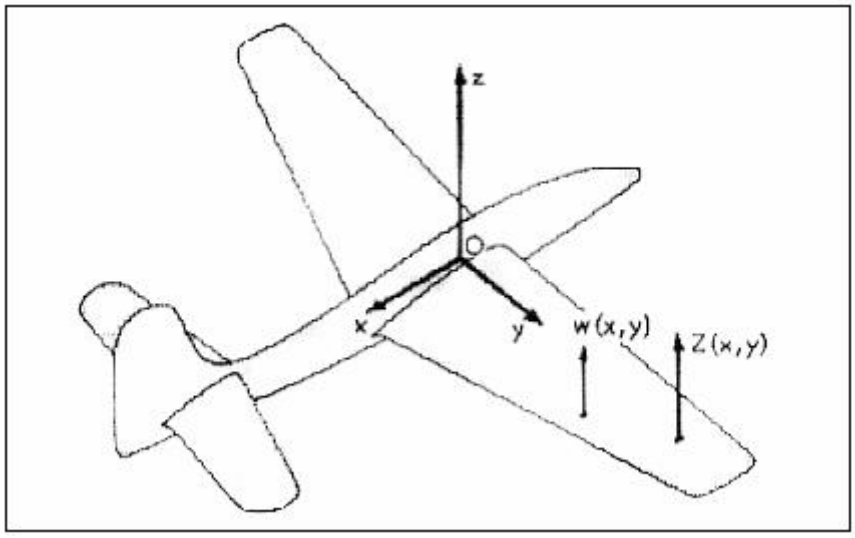

Figure 2.1 Airplane Wing under Distributed Side Load [1]

The deformation of an elastic wing under the influence of a distributed normal force Z(x, y) can be expressed by a single function w(x, y) (Figure 2.1). But the complexity of aircraft structures calls for some simplifications. An aircraft structure can be simplified into a set of intersecting elastic lines. The deformation of each line can be described by two linear displacements and an angular displacement. If the chordwise bending of the wing is negligible, the displacement of the cross section at a point y can be expressed as the combination of two linear and ((w(y), u(y)) and one angular displacement (θ(y)). For those cases where the wing is sufficiently slender so that chordwise segments of the wing parallel to the x axis can be assumed rigid, and neglecting the chordwise drag loads one can obtain the expressions for bending and twisting displacements as follows; [1]

$$w(y) = \int_0^1 C^{zz}(y,\eta).Z(\eta).d\eta + \int_0^1 C^{z\theta}(y,\eta).t(\eta).d\eta \qquad (2.3)$$

$$\theta(y) = \int_0^l C^{\theta z}(y,\eta).Z(\eta).d\eta + \int_0^l C^{\theta\theta}(y,\eta).t(\eta).d\eta \tag{2.4}$$

where the influence functions are defined by

$C^{pq}(y,\eta)$ =linear or angular deflection in the p-direction at y due to a unit force or torque in the q direction at η, and

$$Z(\eta) = \int_{chord} Z(\xi,\eta).d\xi \tag{2.5}$$

$$t(\eta) = -\int_{chord} \xi.Z(\xi,\eta).d\xi \tag{2.6}$$

The terms $C^{z\theta}$, and $C^{\theta z}$ are coupling terms for bending and twisting deformations.

2.1.1 Elastic Axis

Forces applied to a wing on the elastic axis produce pure translation of all sections and no rotations, and the torques applied about that axis produce pure rotations. In the case of a wing in which all forces and moments are resolved into forces along and torques about elastic axis, the applied forces produce pure translations and the torques produce pure rotations, as a result the coupling terms in the Equations 2.3 and 2.4 drop and the equations take the following forms.

$$w(y) = \int_0^l C^{zz}(y,\eta).Z(\eta).d\eta \tag{2.7}$$

$$\theta(y) = \int_0^l C^{\theta\theta}(y,\eta).t(\eta).d\eta \tag{2.8}$$

2.2 STATIC AEROELASTIC PHENOMENA

Consider the rigid section shown in Fig. 2.2, which is attached to a torsional spring of flexibility influence coefficient $C_{\theta\theta}$. The wing has constant chord c and area S and the distance between elastic axis and the aerodynamic center is given as e

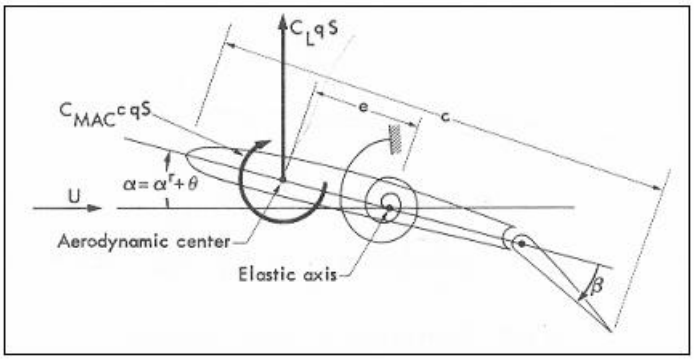

Figure 2.2 Elastically Supported Rigid Airfoil Section [1]

For the rigid section the angle of attack is now a function of the spring stiffness and can be written as the sum of rigid angle of attack (α^r) and the elastic twist (θ).

$$\alpha = \alpha^r + \theta \tag{2.9}$$

The elastic twist is a function of torque about elastic axis (T), which is a representation of wing loading, and the flexibility influence coefficient ($C^{\theta\theta}$), which is a measure of the wing stiffness.

$$\theta = C^{\theta\theta} T \tag{2.10}$$

The aerodynamic moment about the elastic axis can be written as

$$T = (C_L e + C_{MAC} c) qS \tag{2.11}$$

where C_L is the wing lift coefficient, C_{MAC} is the wing moment coefficient about the aerodynamic center, q is the dynamic pressure and S is the area of the rigid wing segment. Wing lift coefficient is further related to the total angle of attack and can be written as

$$C_L = \frac{\partial C_L}{\partial \alpha} (\alpha^r + \theta) \tag{2.12}$$

It is apparent from Eqn 2.12 that the loading on a wing is actually a function of the twist deformation. With the use of Eqn 2.12 and Eqn 2.11 the elastic twist can be rewritten as

$$\theta = C^{\theta\theta} \left[\frac{\partial C_L}{\partial \alpha} (\alpha^r + \theta) e + C_{MAC} c \right] qS \tag{2.13}$$

and the final equation for the elastic twist is as follows

$$\theta = \frac{C^{\theta\theta} \left[(\frac{\partial C_L}{\partial \alpha}) e \alpha^r + C_{MAC} c \right] qS}{1 - C^{\theta\theta} (\frac{\partial C_L}{\partial \alpha}) qSe} \tag{2.14}$$

A close look at Eqn. 2.14 reveals the fact that for a predefined geometry denominator can be zero for certain values of the dynamic pressure. This dynamic pressure is called the divergence dynamic pressure and the corresponding speed is

called the divergence speed. Divergence is not a problem when the aerodynamic center falls onto the elastic axis or aft of it, since the denominator of Eqn. 2.14 has no chance to be zero in these conditions.

For a three dimensional slender straight wing the torsional divergence speed is found from the lowest eigenvalue of dynamic pressure obtained from the equations of equilibrium. In slender straight wings the aeroelastic effects are mainly due to the wing twist about the elastic axis and wing bending is not a factor.

However, for the case of swept wings, bending deformation of the wing has important effects on the aeroelastic behavior. When an upward force is applied to the elastic axis of a swept wing, the points A and B (Fig 2.3) deflect by the same amount but point C shows a smaller deflection, as a result the angle of attack of section BC is reduced. The reduction in the angle of attack results in a decrease in the lift, and the wing bends and twists less in magnitude; this smaller deformation leads to a smaller change in angle of attack.

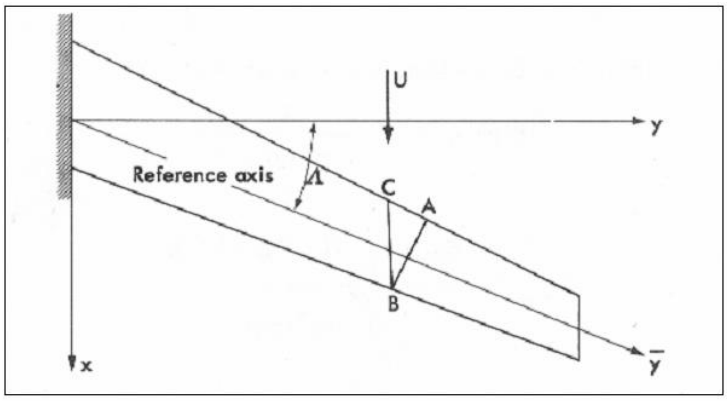

Figure 2.3 Streamwise and Chordwise Segments of Swept Wing [1]

2.3 COMPUTATIONAL AEROELASTIC PROCEDURE

The reliability of an aeroelastic analysis strongly depends on how one calculates the aerodynamic loads over the aerodynamic surface. For many years linear aerodynamic theories have been used for load prediction. Commercial codes like NASTRAN, ASTROS, etc utilize these linear aerodynamic theories in order to predict aeroelastic characteristics of aircraft structures. The linear theories are mostly rely on the thin airfoil theory, the speeds are low and the flow can be assumed incompressible, assumption of small disturbances is valid and skin friction effects are neglected. Most of these theories are modified using empirical relations in order to have more accurate predictions. Today the CFD methods utilize the mass momentum and energy conservation, plus the equation of state in order to predict the motion of a fluid over internal and external bodies. The Navier-Stokes equations are solved to fully define a laminar viscous flow. Turbulence modeling can also be added by using some semi-empirical methods. Reduced form of N-S equations, such as Euler Equations, which assumes inviscid flow, gives reasonable results.

No closed form solution is available in most of the cases; as a result the equations are discretized and numerically solved. A grid is formed and the equations are solved at each point or cell of the grid. After a certain number of iterations the change in the solutions fall below a specified limit and the flow is said to have converged.

The difficulty in using the CFD as a load prediction tool for aeroelastic analysis comes from the fact that the CFD grid has to be deformed to conform to the deformed shape of the aerodynamic surface. A computational aeroelastic procedure was developed as a part of the present work in order to solve the static aeroelastic problems over aircraft wings.

In this study, well-established finite element and CFD solvers are coupled in an iterative fashion. Aerodynamic pressure vector was calculated using a three-

dimensional Euler code (SET3D) in a parallel computing environment. The computed pressures were then mapped into structural nodes and corresponding structural deformation was calculated using ANSYS commercial finite element program. Because of deformation of the underlying structure, the aerodynamic surface over which the flow was solved changed at every iteration. In order to account for this change calculated structural displacements were mapped into the fluid grid and an updated fluid grid was calculated by modeling the fluid grid as an isotropic elastic medium. The fluid flow was then solved over the conformed grid and a new pressure vector was calculated which causes a new displacement field on the structure. This iterative procedure continues until the rms of nodal displacements falls below a prescribed tolerance.

Steps starting with the solution of wing structural displacement vector and ends with the solution of flow field over the deformed aerodynamic surface are named as one aeroelastic iteration hereafter. The flowchart of the iterative procedure is given in Figure 2.4.

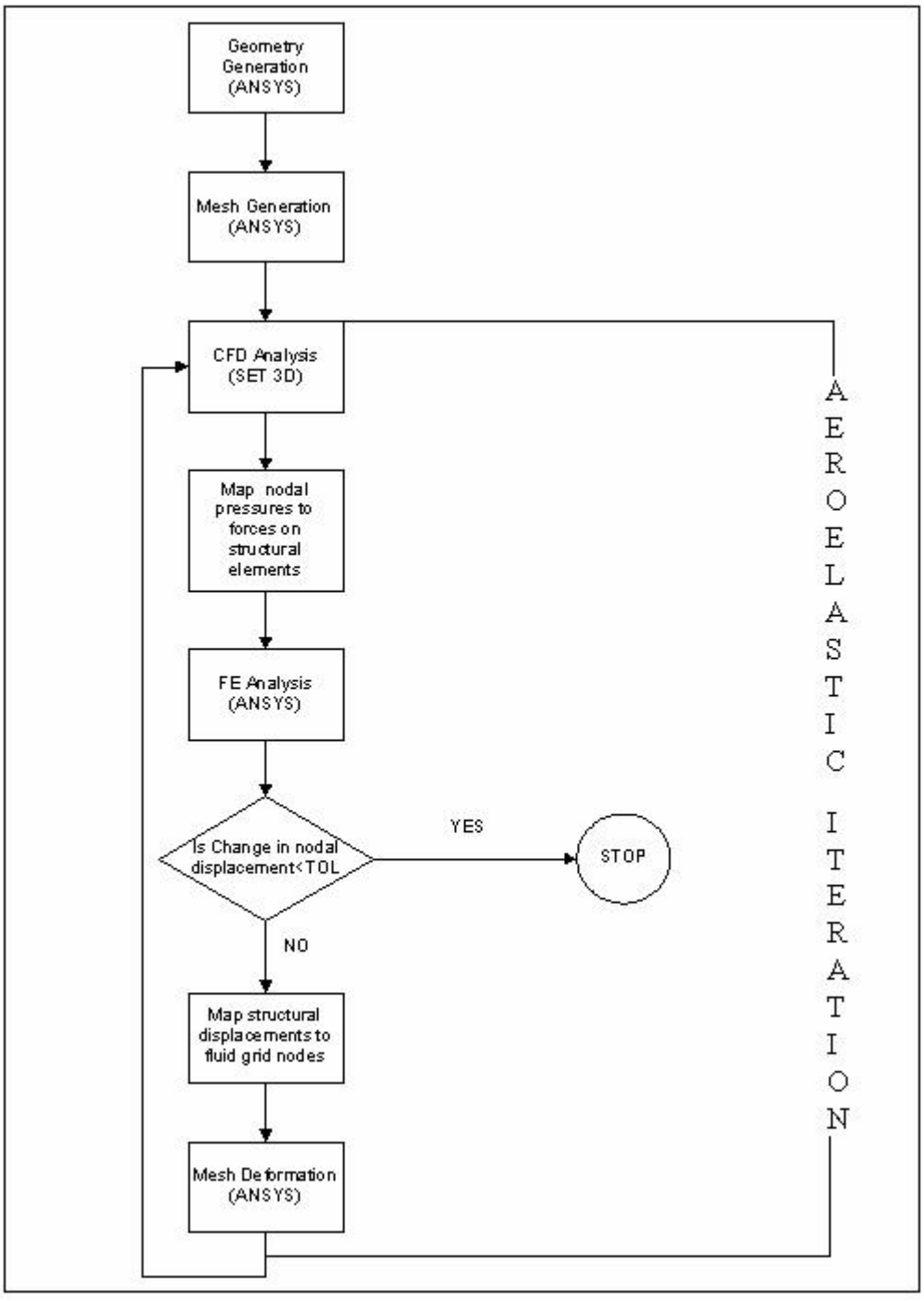

Figure 2.4 Flow Chart of the Computational Aeroelastic Procedure

2.4 COUPLED FIELD SOLUTION OF STATIC AEROELASTIC PROBLEM

In the present study a loosely coupled scheme is used for the iterative solution of the aeroelastic phenomena. In this solution scheme the fluid and structure solution vectors are found independently and coupling is accomplished by applying the relevant boundary conditions. Dynamic aeroelastic problems call for a coupling in both time and space, whereas for static aeroelastic problems, in which time does not appear as an independent variable, the coupling takes place in space only [32, 33, 34]. A schematic of the loosely coupled approach is shown in Figure 2.5.

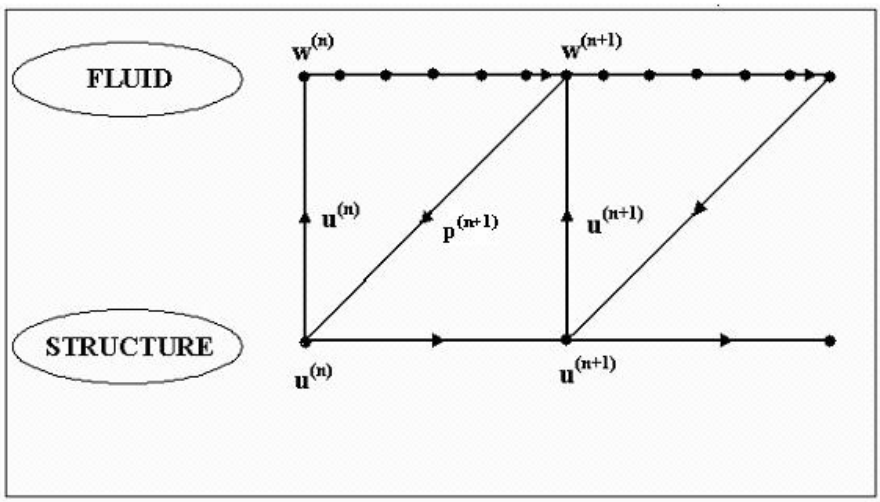

Figure 2.5 Loosely Coupled Approach [34]

2.5 FLOW SOLVER – SET3D

2.5.1 Governing Equations

SET3D (**S**AGE **E**uler **T**etrahedron **3**-**D**imensional) flow solver is used to compute flow fields over aircraft wings. SET3D solves the integral form of the Euler Equations on unstructured grids using a cell-centered finite volume formulation. Time dependent Euler Equations govern the motion of an inviscid fluid by satisfying the conservation of mass, momentum and energy equations. For a control volume V with a boundary S the equations can be written in a vector form as follows:

$$\frac{\partial}{\partial t}\int_V \mathbf{Q}\,dV + \int_S \mathbf{F}(\mathbf{Q}).\mathbf{n}\,dS = 0 \tag{2.15}$$

In this formulation **Q** is the solution vector defined by;

$$Q = \begin{Bmatrix} \rho \\ \rho u \\ \rho v \\ \rho w \\ \rho e_o \end{Bmatrix} \tag{2.16}$$

where

ρ	=	non-dimensional density
ρu	=	non-dimensional momentum in x-direction
ρv	=	non-dimensional momentum in y-direction
ρw	=	non-dimensional momentum in z-direction
ρe_0	=	non-dimensional energy

and the flux vector normal to the boundary surface is given by

$$\mathbf{F(Q).n} = \mathbf{(V.n)}\begin{Bmatrix} \rho \\ \rho u \\ \rho v \\ \rho w \\ e_o \end{Bmatrix} + p\begin{Bmatrix} 0 \\ n_x \\ n_y \\ n_z \\ 0 \end{Bmatrix} \tag{2.17}$$

Note that Euler Equations have 6 unknowns, ρ, u, v, w, e_o and p. With only Euler Equations in hand, the number of unknowns exceeds the number of equations. The additional equation comes form the state of a perfect gas which can be written as;

$$p = (\gamma - 1)\left[e_o - \rho \frac{(u^2 + v^2 + w^2)}{2} \right] \tag{2.18}$$

The Euler Equations are non-dimensionalized by Equation (2.19)

$$\begin{aligned} u &= \frac{\tilde{u}}{\tilde{a}_\infty} \qquad v = \frac{\tilde{v}}{\tilde{a}_\infty} \qquad w = \frac{\tilde{w}}{\tilde{a}_\infty} \qquad a = \frac{\tilde{a}}{\tilde{a}_\infty} \\ \rho &= \frac{\tilde{\rho}}{\tilde{\rho}_\infty} \qquad p = \frac{\tilde{p}}{\rho \tilde{a}_\infty^2} \qquad T = \frac{\tilde{T}}{\tilde{T}_\infty} \qquad e = \frac{\tilde{e}}{\tilde{a}_\infty^2} \end{aligned} \tag{2.19}$$

where overhead ~ represents a dimensional value and subscript ∞ represents a freestream value, a is the speed of sound and u, v and w are the velocity components in x, y, and z directions, respectively.

2.5.2 Numerical Method, Upwind Differencing and Time Integration

The physical domain is discretized using tetrahedral elements. The finite volume formulation is used for the numerical solution of the discretized governing equations; the integral conservation law is enforced for each of the small control volumes defined by the computational mesh.

A cell-centered scheme is used in which the governing equations are solved for each tetrahedron and solution variables are stored at the cell center. The fluxes are computed across the common faces. SET-3D utilizes the Roe's Flux Difference Splitting Scheme for flux evaluation, which computes an exact solution to an approximate Riemann problem. Both implicit and explicit time integration algorithms are available in the solver. Explicit scheme uses a third order accurate Runge-Kutta for numerical solution of ordinary differential equations. Since steady state solutions desired to be obtained at each aeroelastic iteration, the time accuracy does not affect our solutions except the convergence rate. In finite volume discretization, for a constant control volume, Eqn. (2.15) can be represented as

$$\Omega_i \frac{d}{dt}\bar{\mathbf{Q}}_\mathbf{i} + \sum_{j=1}^{Nfaces_i} \left[(\mathbf{F}.\mathbf{n}S)_j \right]_i = 0 \qquad i = 1, Ncells \tag{2.20}$$

where $\bar{\mathbf{Q}}_\mathbf{i}$ is the volume average of $\mathbf{Q}$ over cell i, Ω_i is the volume of cell i, and $\left[(\mathbf{F}.\mathbf{n}S)_j \right]_i$ is the average flux through face j of cell i, an outward flux being positive.

Since Eqn. (2.15) holds for any control volume, the flux balance in Eqn. (2.15) must be satisfied for all cells [35].

2.5.3 Geometry and Grid Generation

The computational grids are obtained using the geometry and grid generation tool of ANSYS. ANSYS has a moderate grid generation tool, computational grids prepared using ANSYS has been extensively used in SET3D analyses and good results were obtained [36].

Modeling of the computational domain starts with creation of the aerodynamic surface over which the flow is solved. Then the far field boundaries of the computational domain are defined and a volume is formed between these outer boundaries and the aerodynamic surface. This volume consists of areas, lines and keypoints.

Grid generation tool of ANSYS supports both structured and unstructured mesh generation. Free and mapped surface triangulation is possible as seen in Figure 2.6.

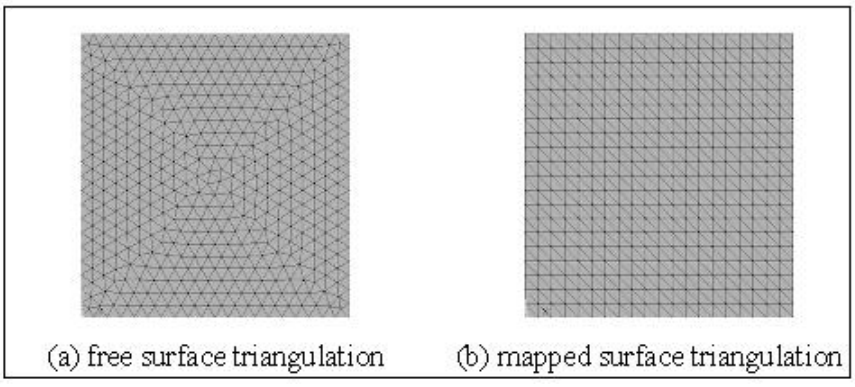

Figure 2.6 Mapped and Free Surface Triangulations.

ANSYS provides many tools to control grid density, both on a global and local level. Global element sizing allows user to specify a maximum element edge length or number of division per line for the entire model. In local level, different element sizes can be defined for keypoints, lines and areas. Number of divisions and a spacing ratio can be defined for lines, and an element size can be specified in the interior of an area.

The first step in a grid generation process is to create a surface grid using the automatic mesh generator by defining the global element sizes on areas and line divisions. Special attention is given to regions where high gradient flow parameters are expected, like leading edge and trailing edge of a wing.

After generating the surface grid a computational domain made up of tetrahedral elements are formed. ANSYS tetrahedral mesher is based on a Delaunay Technique [37]. The resulting grids are boundary conforming.

The generation of tetrahedral elements mostly depends on the surface triangulation, and the size of the computational domain. The quality of the volume grid also depends on the farfield boundary distance and the number of grid points on the boundary edges. The density of the volume mesh can be controlled by *Esize* option (defines the global element size) and the expansion of tetrahedral meshes can be controlled by the *Tetexpnd* (tetrahedral mesh expansion factor) option in ANSYS program.

In most cases the size of the elements on the aerodynamic surface is small compared to the computational domain size. Setting the global element size closer to the element size used in the surface triangulation, and setting the tetexpand option to small values, results in high-density meshes of gradually expanding nature.

But this approach leads to high-density grids, which requires high amount of memory and even saving the information is difficult. One remedy to this problem is to divide the solution domain into smaller volumes. The volume that contains the aerodynamic surfaces as a boundary can be meshed with a large number of elements. The density of the mesh is decreased gradually towards the outer boundaries. A computational domain that is divided into a number of small volumes and the corresponding grid is shown in Figure 2.7. ANSYS SOLID45 element is used for discretization of the solution domain.

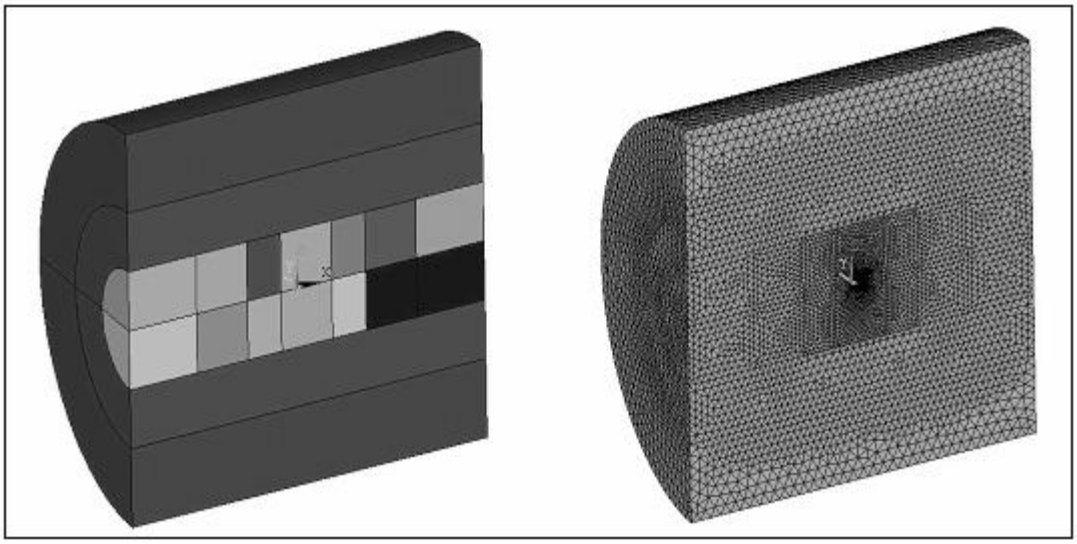

Figure 2.7 Solution Domain Divided into Smaller Volumes and Resulting Computational Domain.

After a computational domain is constructed, nodes associated with the farfield boundary, wall boundary and symmetry boundary are listed in three different text

files; namely, *nbound.lis*, nwall.lis and *nsymmetry.lis.* The grid point coordinates of all grid points are listed in *nall.lis* file and elements and the associated grid point are listed in the *elist.lis* file. A preprocessing program written in FORTRAN language reads the generated files and creates the *mesh.ansys* file, which contains the grid point coordinates, connectivity information and boundary conditions.

2.5.4 Implementation of Boundary Conditions

In SET3D, boundaries are represented by cell flags, IBC. These flags are given to the solver as an input via the *mesh.ansys* file as described in section 2.5.3. Flow conditions such as Mach number, angle of attack and yaw angle are given in the input file, set3d.in. The boundary condition flags used in the SET3D are as follows;

Far Field Boundary Condition; IBC=1

This flag represents the far field boundaries. Characteristic boundary conditions are applied to the far-field boundaries using the fixed and extrapolated Riemann invariants corresponding to the incoming and outgoing waves. The incoming Riemann invariant is determined from the freestream flow and the outgoing invariant is extrapolated from the interior domain

Wall Boundary Condition; IBC=-2

This flag represents the solid boundaries such as wing and fuselage surfaces. The flow tangency condition is imposed by setting the velocities on the boundary faces to their cell-centered values. The normal components to the boundary surface are then subtracted from these velocities. Density and pressure boundary conditions are set to their cell-center value.

Symmetry Boundary Condition; IBC=-4

This flag represents the solid boundaries such wind tunnel walls. The treatment of these boundaries is the same as that of wall boundaries.

2.6 STRUCTURE SOLVER-ANSYS

2.6.1 Governing Equations

Equations of elasticity governing the motion of a deformable body under the action of external forces can be written as follows;

$$\sigma_{ij,j} + B_i = \rho \frac{\partial^2 u_i}{\partial t^2}$$

$$\varepsilon_{ij} = \frac{1}{2}(u_{i,j} + u_{j,i}) \qquad (i = x, y, z) \qquad (2.21)$$

$$\sigma_{ij} = \delta_{ij}\lambda e + 2\mu \varepsilon_{ij}$$

where

σ_{ij}	=	Stress Tensor
ε_{ij}	=	Strain Tensor
B_i	=	Body Force per Unit Mass
u_i	=	Displacement
λ,μ	=	Lame's Constants

The first equation of (2.21) is the equation of motion for a dynamic problem. For static cases and by neglecting body forces the equation can be written as;

$$\sigma_{ij,\,j} = 0 \tag{2.22}$$

The second set of equations are referred to as the compatibility equations and the third one represents the constitutive relations.

Together with the boundary conditions in terms of forces and displacements, the problem is termed as the boundary value problem of elasticity. Closed form solutions are available for a limited number of problems, so numerical techniques are needed to solve this type of problems for complex geometries.

2.6.2 Finite Element Method and ANSYS Finite Element Solver

The finite element method is a numerical procedure for analyzing structures and continua. Usually the problem is too complicated to be solved satisfactorily by classical analytical methods. The finite element procedure produces many simultaneous algebraic equations, which are generated and solved on a digital computer [38].

The system of linear equations generated by the finite element procedure can be written as

$$[K]\{u\} = \{F\} \tag{2.23}$$

ANSYS finite element software is used to solve the displacements associated with the aerodynamic loading calculated by the flow solver.

The finite element modeling process is not explained here in detail since it is standard for any finite element program. In short the finite element modeling in ANSYS starts with defining element types, element real constants, material properties and the model geometry. The geometry is then divided into finite

elements. Wing box structures are modeled with shell and beam elements. Then appropriate loading and boundary conditions are applied to the model. This first step is referred to as the preprocessing stage.

The next step is the solution stage. In this stage analysis type is defined using the *ANTYPE* command. The equation solver is selected which solves the system of simultaneous linear equations given in Equation (2.23) generated by the finite element procedure. The equations are solved either by using direct elimination or iterative methods. The last step is the post processing stage where the resulting displacements, stresses and strains are processed.

The computational aeroelastic procedure needs multiple calls to ANSYS program, which necessitates ANSYS program to be run in Batch mode. In Batch mode a text file, which includes the necessary commands, is submitted to the ANSYS program. Program reads the commands, solves the problem and writes desired solution parameters to text files.

2.6.3 ANSYS Finite Elements Used in Structural Analysis

SOLID187 Element

SOLID187 element is a higher order 3-D, 10-node element, which has a quadratic displacement behavior and is well suited to modeling irregular meshes. The element has ten nodes with three translation degree of freedom in the nodal x, y, and z directions. The geometry and node locations for this element are shown in Figure 2.8.

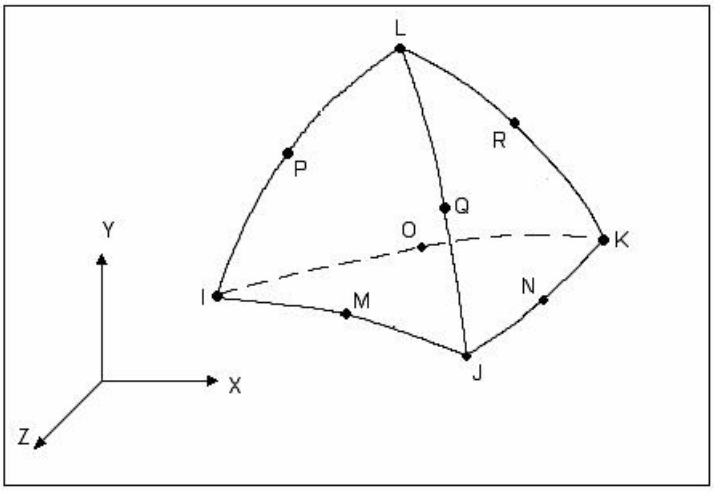

Figure 2.8 ANSYS SOLID187 Element [37]

SHELL63 Element

SHELL63 element has both bending and membrane capabilities. Both in-plane and normal loads are permitted. The element has six degrees of freedom at each node; translations in the nodal x, y, and z directions and rotations about the nodal x, y, and z-axes. Membrane stiffness or the bending stiffness can be neglected depending on the application. The geometry, node locations, and the coordinate system for this element are shown in Figure 2.9. The element is defined by four nodes, four thicknesses and material properties.

The thickness of the element is defined by a real constant set. If the element has a constant thickness, then defining the thickness at only one node is adequate. Pressures may be input as surface loads on each element face. The element has a triangular option as shown in Figure 2.9.

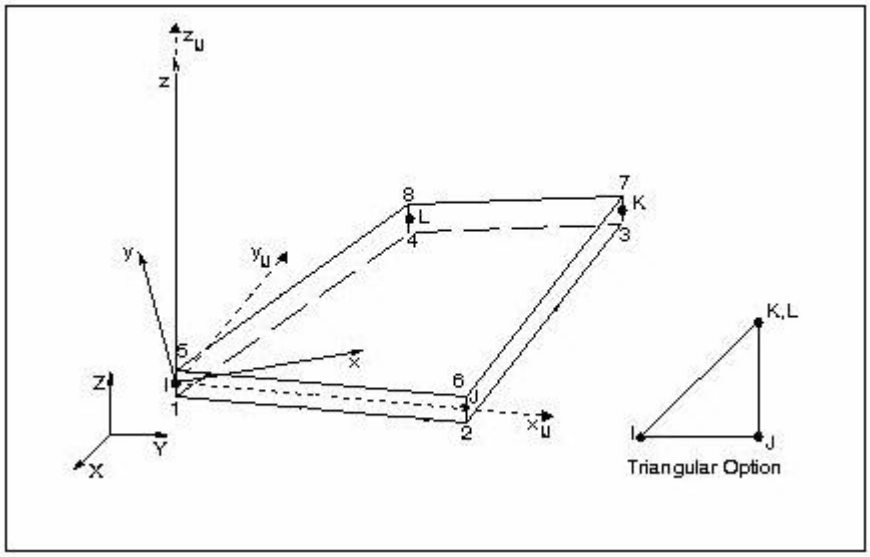

Figure 2.9 ANSYS SHELL63 Element [37]

BEAM4 Element

BEAM4 is a uniaxial element with tension, compression, torsion, and bending capabilities. The element has six degrees of freedom at each node; translations in the nodal x, y, and z directions and rotations about the nodal x, y, and z axes.

The geometry, node locations, and coordinate systems for this element are shown in Figure 2.10. The element is defined by two or three nodes, the cross-sectional area, two area moments of inertia (IZZ and IYY), two thicknesses (TKY and TKZ), an angle of orientation (θ) about the element x-axis, the torsional moment of inertia (IXX), and the material properties. If IXX is not specified or is equal to 0.0, it is assumed equal to the polar moment of inertia (IYY+IZZ). IXX should be positive and is usually less than the polar moment of inertia. The element torsional stiffness decreases with decreasing values of IXX.

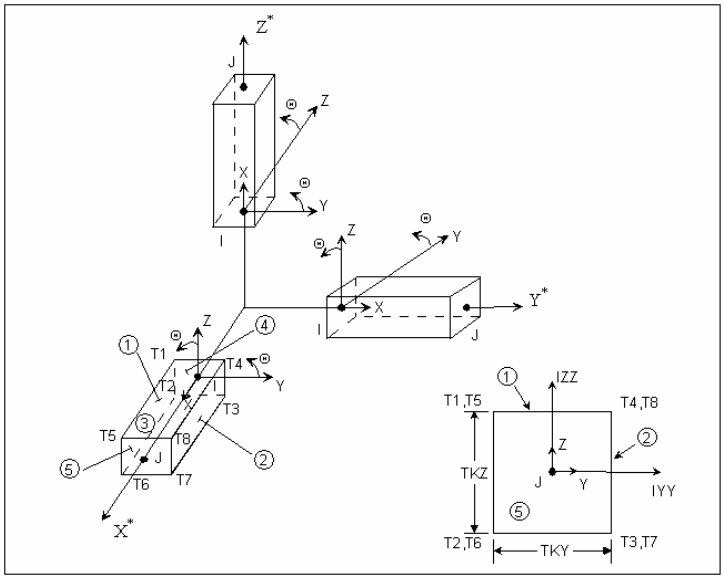

Figure 2.10 ANSYS BEAM4 Element [37]

Pressures may be input as surface loads on the element faces as shown by the circled numbers on Figure 2.10. Positive normal pressures act into the element.

2.7 CFD GRID DEFORMATION METHOD

The numerical solution of flow problems with moving boundaries calls for an algorithm to deform the computational domain grid so as to conform to the deforming structure on the fluid-structure interface.

The widely used approach is to view the fluid grid as a continuous or discrete pseudo-structural system. The behavior of such a mechanical system is governed by the semi-discrete equations of the dynamic equilibrium given by Equation (2.24).

$$[M]\ddot{\mathbf{q}}+[D]\dot{\mathbf{q}}+[K]\mathbf{q}=0 \qquad (2.24)$$

where a dot overhead designates a time derivative, M, D and K are the system of fictitious mass, damping and stiffness matrices and q is the displacement vector [17].

The grid points attached to the moving boundary Γ_m stay attached to these boundaries at some relative locations, and therefore the equation of dynamic equilibrium is driven by the displacement type boundary condition

$$\mathbf{q} = \mathbf{q_m} \quad \text{on} \quad \Gamma_m \tag{2.25}$$

where q_m is the displacement vector of the moving boundary. The positions of the internal grid points are then obtained from the time integration of Equation (2.24) using the boundary condition Equation (2.25).

Most of the work on moving grids used the quasi-static version of Equation (2.24) which can be written as

$$[K]\mathbf{q} = 0 \qquad \text{and} \qquad \mathbf{q} = \mathbf{q_m} \tag{2.26}$$

Following the work of Batina [39] most of the approaches have used the linear spring analogy method to create the left hand side of Equation. (2.26). In this analogy CFD computational grid is treated as a system of interconnected springs. Each edge of triangle in 2-D or tetrahedron in 3-D is considered as a lineal spring as shown in Figure 2.11.

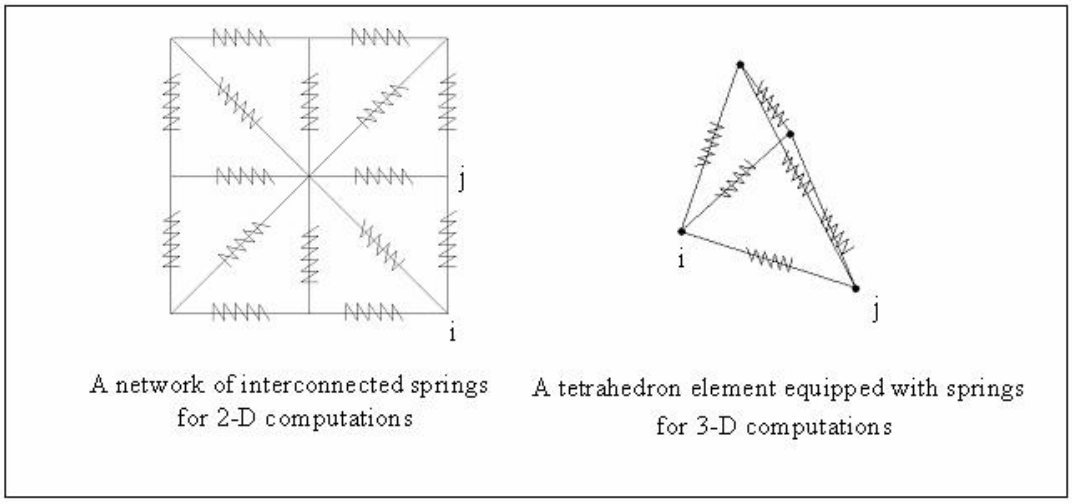

Figure 2.11 Spring Analogy Method for CFD Grid Deformation

For a given edge i-j the spring stiffness is taken as inversely proportional to the length of the edge as defined in Equation (2.27).

$$k_{spring} = \frac{1}{\sqrt{(x_j - x_i)^2 + (y_j - y_i)^2 + (z_j - z_i)^2}} \tag{2.27}$$

Grid points on the outer boundary are held fixed and new locations for the grid points are solved by imposing the body motion.

The method of spring analogy fails in situations where large amplitude grid motion occurs. This is mainly due to the stiffness definition. Stiffness definition given in Equation (2.27) does not take into account the formation of zero area/volume and bad aspect ratio elements. One remedy to this problem is proposed by Farhat and co-authors [17, 18]. They proposed to attach to each vertex i and for each triangle

T_{ijk} connected to i, a torsional spring as shown in Figure 2.12, whose stiffness is given by Equation (2.28)

$$C_i = \frac{1}{1+\cos\theta_i} \times \frac{1}{1-\cos\theta_i} = \frac{1}{\sin^2\theta_i} \tag{2.28}$$

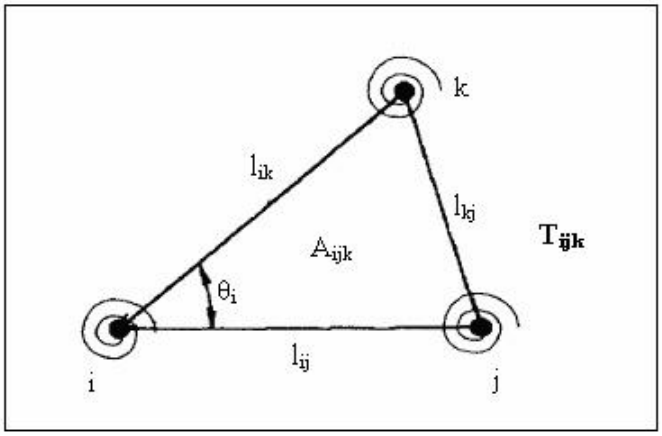

Figure 2.12 Torsional Spring Analogy Method for CFD Grid Deformation

When $\theta_i \rightarrow 0$ or $\theta_i \rightarrow \pi$ the stiffness of the torsional spring goes to infinity and as a result the torsional spring attached to vertex i prevent this vertex from crossing any edge that faces it and any triangle from attaining a zero or negative area.

The torsional spring constant can be written in terms of area of the triangle (A_{ijk}) and edge lengths l_{ik} and l_{ij} as follows:

$$\sin\theta_i = \frac{2A_{ijk}}{l_{ij}\, l_{ik}}$$

$$C_i = \frac{l_{ij}^2 l_{ik}^2}{4A_{ijk}^2} \tag{2.29}$$

For three dimensional applications, the use of torsional spring analogy is not as easy as in two dimensional applications, since collapse mechanisms for 3-D elements is more complex than the two dimensional triangle [18].

2.7.1 A Finite Element Based Method for Grid Deformation

Since the flow solver SET3D does not have a moving mesh algorithm, a mesh deformation procedure is developed as a part of this work. The procedure views the whole CFD computational domain as an isotropic elastic medium and uses the tetrahedral elements generated for finite volume discretization as finite elements. The outer boundaries are held fixed and the structural displacements of deforming aerodynamic surface are given as displacement type boundary condition, the resulting equations are then solved using the ANSYS finite element program.

ANSYS SOLID45 elements have been used for the discretization of CFD solution domain. The geometry node locations and the coordinate systems for this element are shown in Figure 2.13.

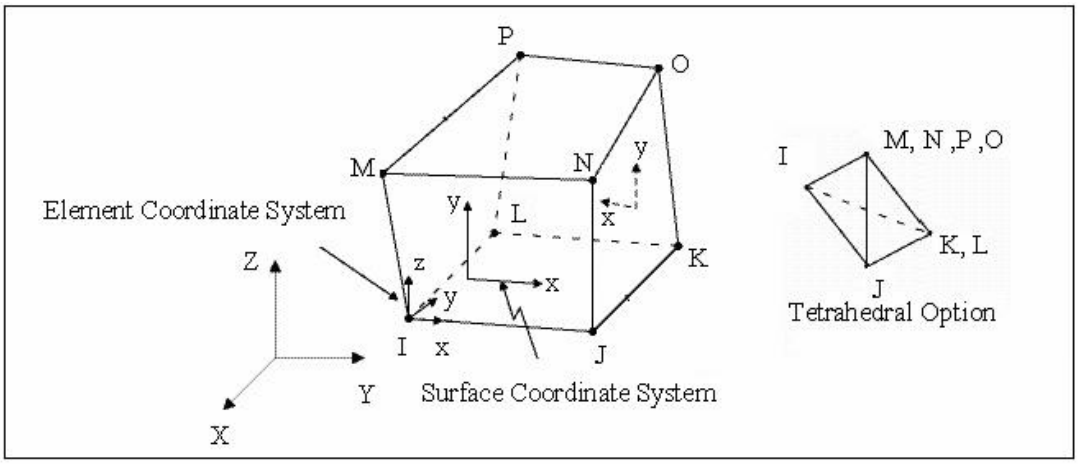

Figure 2.13 ANSYS SOLID45 Element [37]

For hexahedral option the element is defined by eight nodes and the material properties. Tetrahedral option is also available and shown in Figure 2.13. CFD computational domain is formed by using tetrahedral option and mesh deformation calculations is also performed on this option of the element. Element has three translational degree of freedom at each node, u_x, u_y and u_z.

Appropriate material properties have to be defined in order to deform CFD domain. Preliminary studies have been performed to find a way to define fictitious material properties for the solution domain so that under the action of applied boundary conditions a new computational domain with valid elements can be obtained. Preliminary studies were performed on a 2-D computational domain which had been formed in order to solve flow over a NACA-0012 airfoil. The geometry of the solution domain and the resulting computational domain are given in Figures 2.14-2.15, respectively.

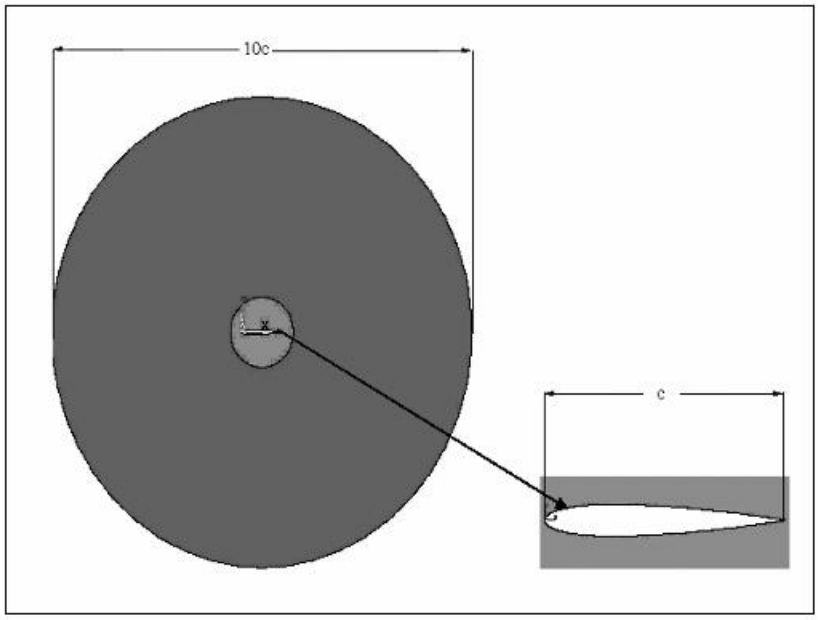

Figure 2.14 Geometry of the Solution Domain for NACA0012 Airfoil

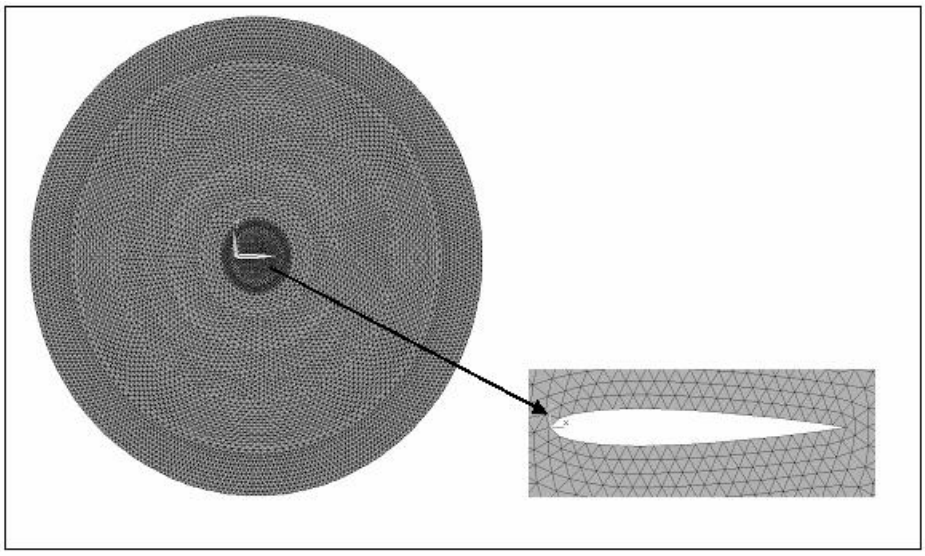

Figure 2.15 Computational Grid for NACA0012 Airfoil (18314 elements, 9332 nodes)

The solution domain was divided into two areas and material properties were defined so that the inner area (area with blue color in Fig.2.14) has a large value of modulus of elasticity and the outer area (area with magenta color in Fig 2.14) has a small value. By this way it was expected that elements near the moving boundary will deform a little so that the grid quality in this region does not change more, while the elements away form the moving boundary will deform more as compared to elements in the inner area.

Nodes at outer boundaries are held fixed and a displacement type boundary condition is imposed at the nodes of the deforming boundary so that the airfoil rotates 30 degrees about half chord.

Undeformed and deformed states of the computational domain are given in Figure 2.16. An examination of undeformed and deformed states of the computational domain at leading edge is given in Figure 2.17 and 2.18, respectively. Figure 2.18 reveals that the elements near the airfoil geometry deform more than expected. Element number 1383 loses its shape completely; a node of the element crosses the edge facing it. This collapse mechanism, which is explained before for Spring Analogy Method, shows itself here with the above-mentioned material properties assigned to the areas. An examination of undeformed and deformed states of computational domain at trailing edge is given in Figure 2.19 and 2.20, respectively. A comparison of two states shows that elements near trailing edge distorted when compared to their initial shapes.

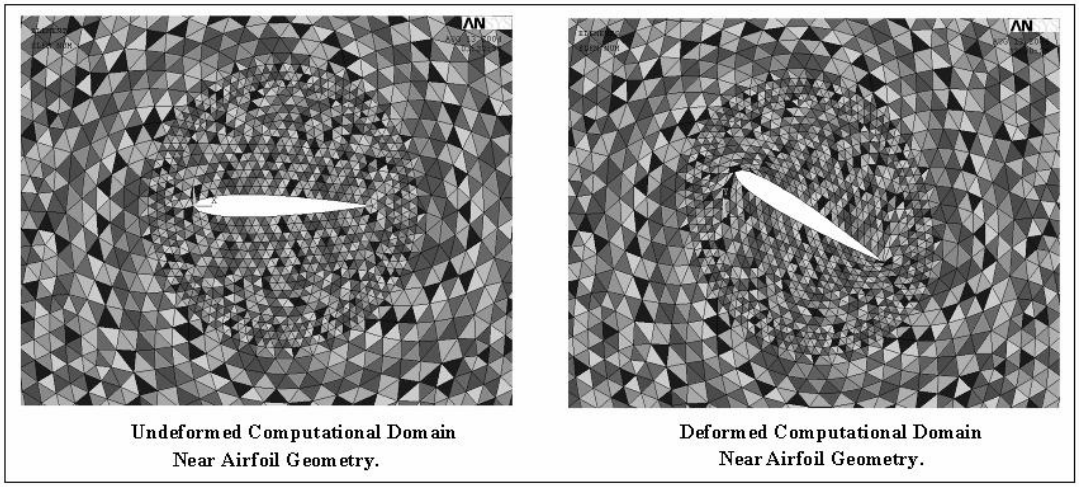

Figure 2.16 Deformed and Undeformed Computational Domains near Airfoil Geometry

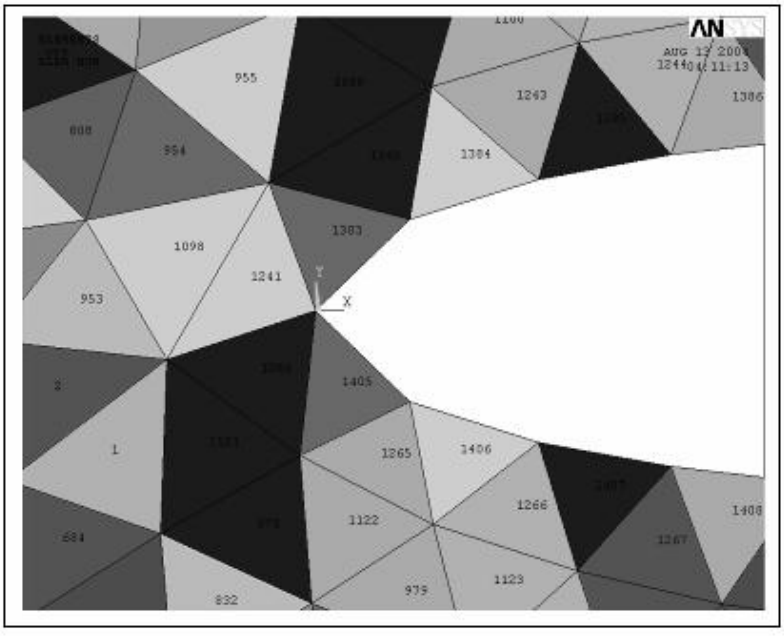

Figure 2.17 Undeformed Computational Domain (A Close Look at Leading Edge)

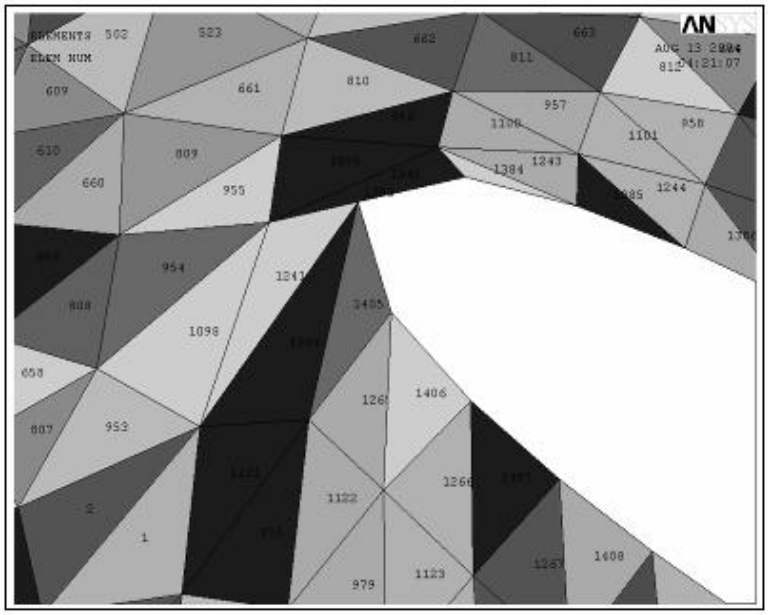

Figure 2.18 Deformed Computational Domain (A Close Look at Leading Edge)

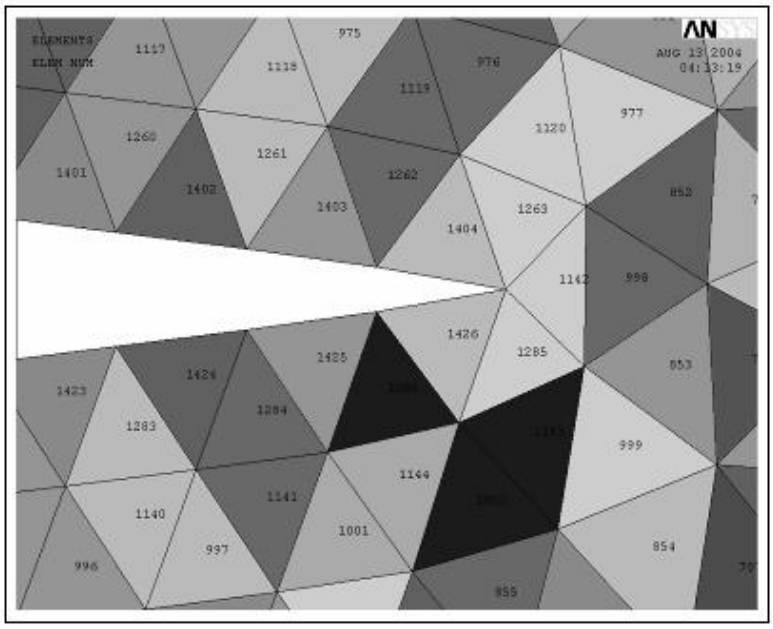

Figure 2.19 Undeformed Computational Domain (A Close Look at Trailing Edge)

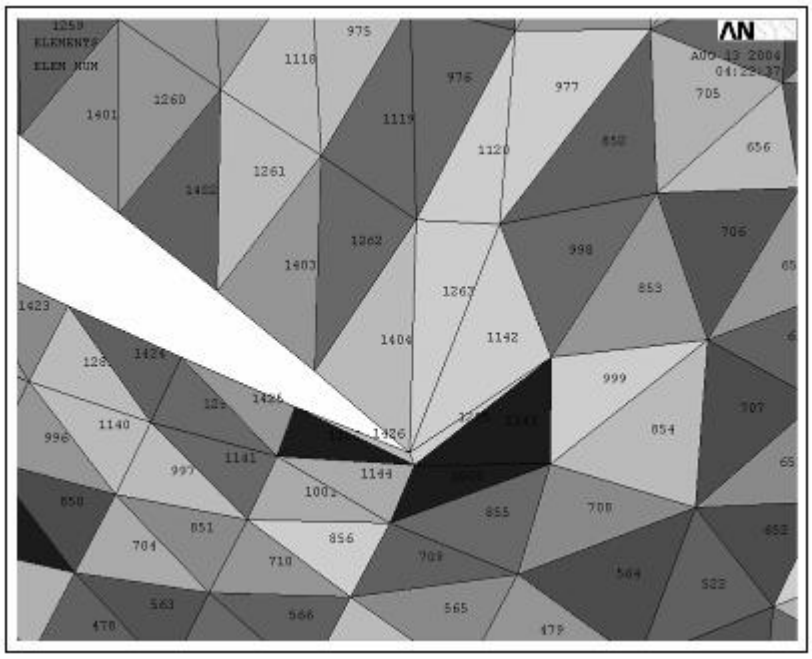

Figure 2.20 Deformed Computational Domain (A Close Look at Leading Edge)

A remedy to the above mentioned problem is to define the material property of each element according to its size. In this approach elasticity modulus of each element is defined as inversely proportional to the area of the element as given in Equation (2.30).

$$E_i = \frac{C}{A_i^n} \qquad i = 1, \text{numel} \tag{2.30}$$

where E_i is elasticity modulus of element i, A_i is the area of element i, C and n are two constants and numel stands for number of elements.

Since the CFD domain is modeled as an isotropic medium, shear modulus of each element is directly related to elasticity modulus as given in Eqn. (2.31)

$$G_i = \frac{E_i}{2(1+\upsilon)} \qquad i = 1, numel \tag{2.31}$$

where G_i is the shear modulus of element i and υ is the Poisson's Ratio which is taken as 0.3 for all elements.

A small ANSYS Parametric Design Language (APDL) program is written, which finds the area of each element in the computational domain and assigns material properties to each element using Equation (2.30). APDL program that assigns material properties is given in Appendix A. For a constant value of $C=5x10^5$ analysis are performed for n=1 to n=6. It is seen that the change in the shape of elements near the airfoil geometry decreases as n increases. But increasing n=6 leads to distorted elements far from the moving boundary. The comparison of deformed computational domain shapes are given in Figure 2.21 for n=2 and n=6 cases.

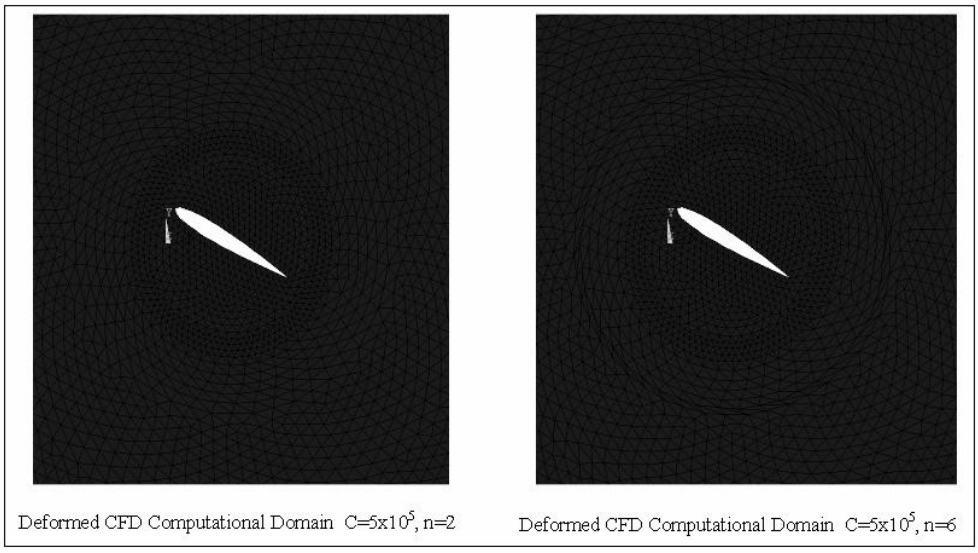

Figure 2.21 Deformed Computational Domains with n=2 and n=6

Details of the solution domain at leading and trailing edges for n=2 case is given in Figures 2.22-2.23.

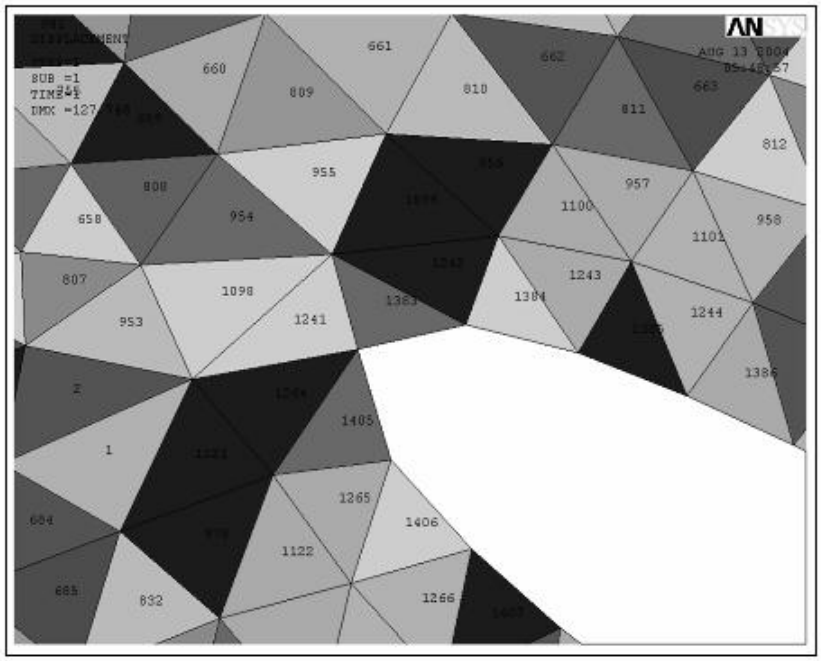

Figure 2.22 Deformed Computational Domain Leading Edge n=2

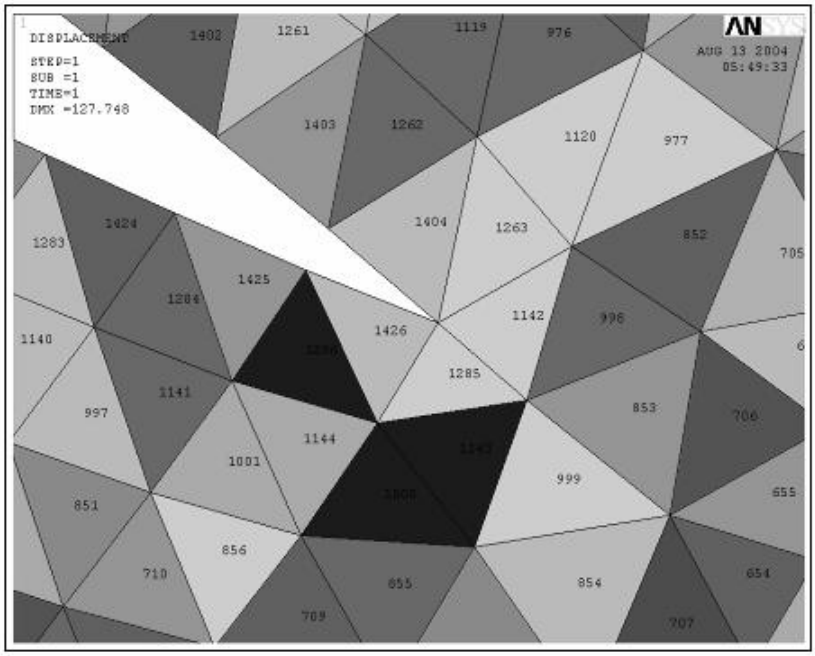

Figure 2.23 Deformed Computational Domain Trailing Edge n=2

Adopting the above finite element based strategy of mesh deformation to 3-D cases is straightforward. In 3-D cases the volume of an element is used in calculating element material properties. The modified version of Eqn (2.30) for 3-D cases is given in Eqn (2.32)

$$E_i = \frac{C}{V_i^n} \qquad i = 1, \text{numel} \tag{2.32}$$

where V_i is the volume of 3-D element i.

2.8 LOAD AND MOTION TRANSFER METHODS

In most of the work in computational aeroelasticity literature the fluid and structure meshes are incompatible along the fluid-structure interface as shown in Fig. 2.24

[19, 40, and 41]. This leads to the need of efficient algorithms to transfer pressures at the fluid grid points to structural grid points as nodal forces, and displacements at structure grid points to fluid grid points. [40, 42]

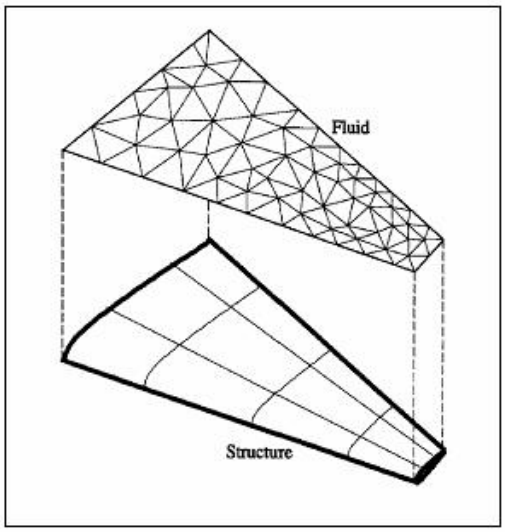

Figure 2.24 Fluid and Structure Meshes with Non-Matching Interfaces [40]

In the present work the computational domain of the fluid and the structure problems have matching discrete interfaces. The nodes at the surface of structural finite element model also belong to the elements of finite volume discretization. Actually a triangular element of finite element discretization is a face of a tetrahedron element of finite volume discretization. Fluid and structure meshes with matching interfaces are shown in Fig. 2.25.

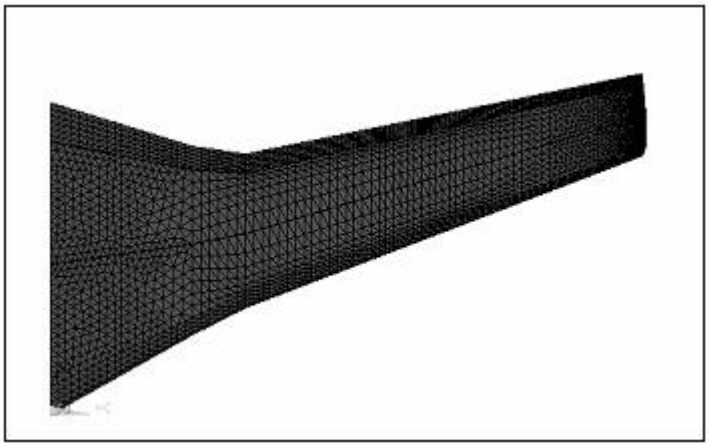

Figure 2.25 Fluid and Structure Meshes with Matching Interfaces

Nodes of structural elements and tetrahedron elements at fluid/structure interface show one-to-one correspondence even in node numbering; that is, node number i with coordinates x, y and z is the same for both structural and fluid domains at the interface.

2.8.1 Motion Transfer Method

The structural displacements, which are obtained from structural analysis, are easily transferred to CFD computational domain since the nodes show one-to-one correspondence. After the structural model is solved using ANSYS Finite Element Solver, the displacements in x, y and z directions are written to a text file called *nwalldisp*. *nwalldisp* file is opened by ANSYS program at the beginning of mesh deformation calculations and stored as an array within the program. Structural displacements at each node of the structural model are applied directly to the CFD grid and new grid point coordinates are found by using the method explained in Section 2.7.1. The flow over the deformed shape is solved using flow conditions of previous iteration.

2.8.2 Load Transfer Method

Non-dimensional pressure values obtained from the CFD solver are dimensionalized and applied directly to the structural nodes (once again all fluid nodes on the fluid/structure boundary are the same as structural nodes). Non-dimensional pressure values on fluid nodes are written to *pressure.dat* file by the flow solver SET3D. This file is opened by ANSYS program at the beginning of the structural calculations and pressure values are stored in an array, non-dimensional values are turned into dimensional ones within ANSYS and stored as an array called P, and then they are applied to the structural nodes.

ANSYS SFFUN and SF Commands

Once the dimensional pressure values are stored as an array within the ANSYS program, one can use the SFFUN command to define loading over the aerodynamic surface. The location of the value in the array implies the node number, that is, the first element of array P is the pressure value at node number 1.

For a triangular element with three nodes SFFUN command together with SF command fits a surface load function depending on the pressure value at each node. The resulting force can be found by multiplying the average pressure value with the area of the element.

A basic representation of this loading is shown in Figure 2.26 for only one triangular element with nodes 1, 2 and 3 which have pressure values of 10, 20 and 30, respectively.

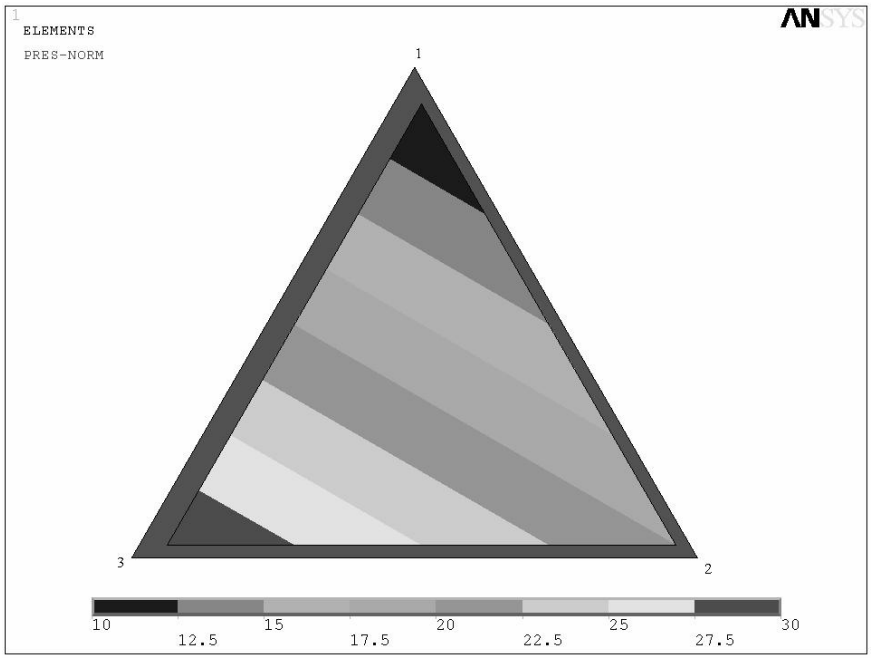

Figure 2.26 Pressure Distribution over a Triangular Element

2.9 COUPLING ENVIRONMENT, ANSYS INPUT FILES, AND PERL SCRIPTING LANGUAGE

Flow solver SET3D works in a parallel computing environment under Linux operating system. ANSYS finite element program works under both Linux and Windows operating systems. In the present work a Linux version of ANSYS program was used for structural and mesh deformation calculations. A PERL script is written that calls the structure solver (ANSYS), mesh deformation solver (ANSYS) and flow solver (SET-3D) repeatedly until the difference between root mean square of displacements of structural nodes between two aeroelastic iterations falls below a specified tolerance. The PERL script used in calculations is given in Appendix B.

The PERL script calls two ANSYS input files written in APDL. The first one is an input file called set3d_ansys_str.txt, which includes all necessary commands to perform a linear static finite element analysis of the structure. The second input file is called; ansys_str_set3d.txt, which includes all necessary commands to perform mesh deformation analysis. The two input files are given in Appendix C and D.

CHAPTER 3

TEST CASE I – AGARD WING 445.6

3.1 INTRODUCTION

In this chapter the present method is applied to solve static aeroelastic characteristics of AGARD Wing 445.6, which was previously tested for its flutter characteristics in the Langley TDT [21]. The wing has a panel aspect ratio of 1.65, a taper ratio of 0.66 and a quarter-chord sweep angle of 45^{o} and NACA 65A004 airfoil sections in the streamwise direction. The wing planform is shown in Figure 3.1.

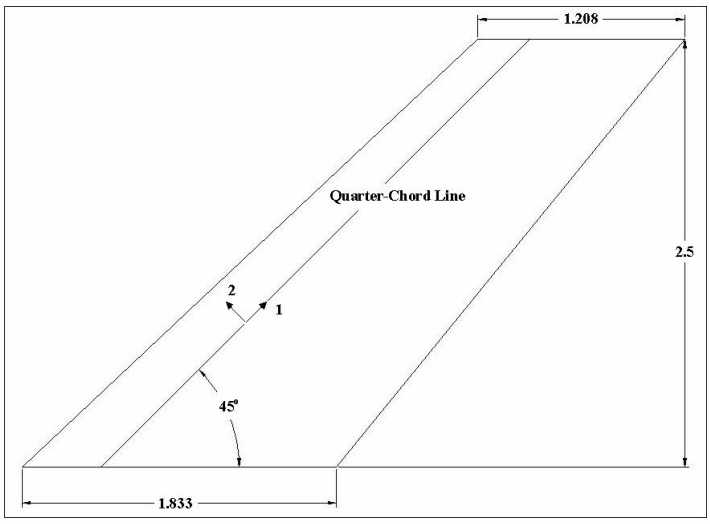

Figure 3.1 AGARD Wing 445.6 Planform (All linear dimensions are in foot)

AGARD Wing 445.6 which was used in an experimental study [21] was constructed by laminated mahogany, which can be assumed as an orthotropic material. The solid wing model is shown in Figure 3.2.

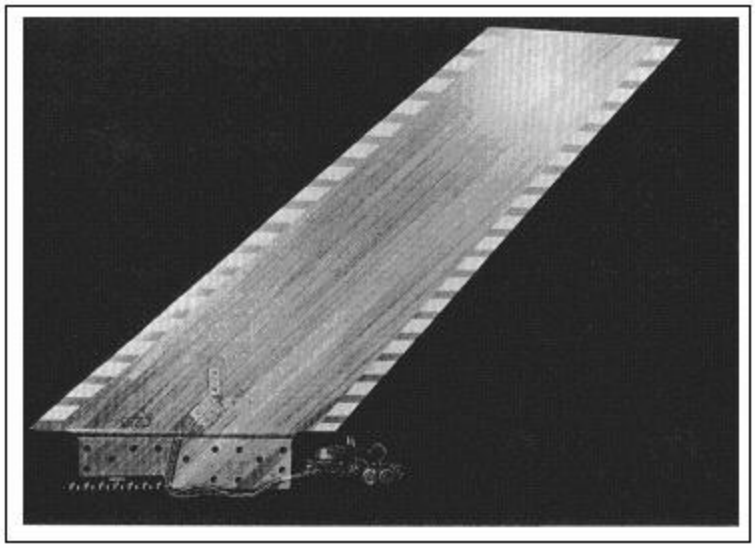

Figure 3.2 Solid AGARD Wing 445.6 [21]

In order to obtain flutter at the desired Mach number and density the stiffness of the solid model was reduced by drilling holes through the wing. Rigid foam plastic was used as a filler to maintain aerodynamic continuity [21]. This reduced stiffness model was named as weakened model and is shown in Figure 3.3. This model will be used in validation studies

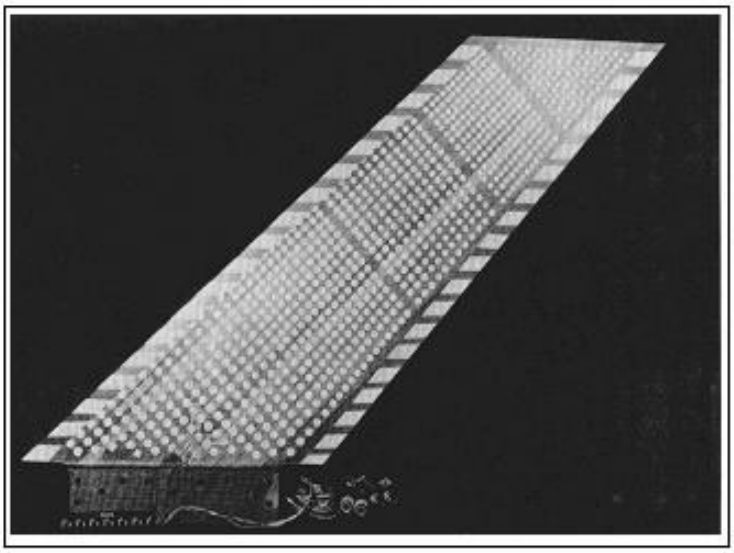

Figure 3.3 Weakened AGARD Wing 445.6 [21]

For an orthotropic material, material properties are unique and independent in three mutually perpendicular directions. For AGARD Wing 445.6, these directions are shown in Figure 3.1. The fiber orientation of the wood is taken along the wingspan and is denoted as 1. Material properties for laminated mahogany was obtained from [43] and given in Table 3.1.

Table 3.1 Mechanical Properties of Laminated Mahogany.

Material Property	Value (lbf/ft^2)
E_{11}	192.96×10^6
E_{22}	12.63×10^6
E_{33}	21.11×10^6
G_{12}	13.02×10^6
G_{13}	16.59×10^6
G_{23}	5.53×10^6
Material Property	Value
ν_{12}	0.034
ν_{13}	0.033
ν_{23}	0.326

E_{11}, E_{22}, and E_{33} are the modulus of elasticity, G_{12}, G_{13} and G_{23} are the shear modulus and ν_{12}, ν_{13}, and ν_{23} are the Poisson's ratios.

The stiffness properties of the weakened wing can be approximated by multiplying the material properties given in Table 3.1 with appropriate stiffness reduction factors as suggested by Yates [21]. These reduction factors, which are deduced from [21], are 0.397 for elasticity modulus values and 0.515 for shear modulus values. The weakened model material properties are then found by multiplying the values given in Table 3.1 with mentioned reduction factors, and are given in Table 3.2

Table 3.2 Mechanical Properties for the Weakened AGARD Wing 445.6

Material Property	Value (lbf/ft^2)
E_{11}	76.675 x10^6
E_{22}	5.019x10^6
E_{33}	8.388 x10^6
G_{12}	6.711x10^6
G_{13}	8.551x10^6
G_{23}	2.850x10^6
Material Property	Value
ν_{12}	0.034
ν_{13}	0.033
ν_{23}	0.326

3.2 AGARD WING 445.6 CFD ANALYSIS

3.2.1 Grid Sensitivity Study

For CFD grid sensitivity four unstructured grids with varying surface and volume resolutions are studied. CFD analyses are performed for M=0.85 $\alpha=5^o$, M=096 $\alpha=0^o$, and M=1.141 $\alpha=0^o$ flow conditions. In this part the details of computational grids and the results of the rigid wing analyses are given.

The dimensions of half cylinder shape solution domain are given in Figure 3.4, and an isometric view of the computational domain is given in Figure 3.5.

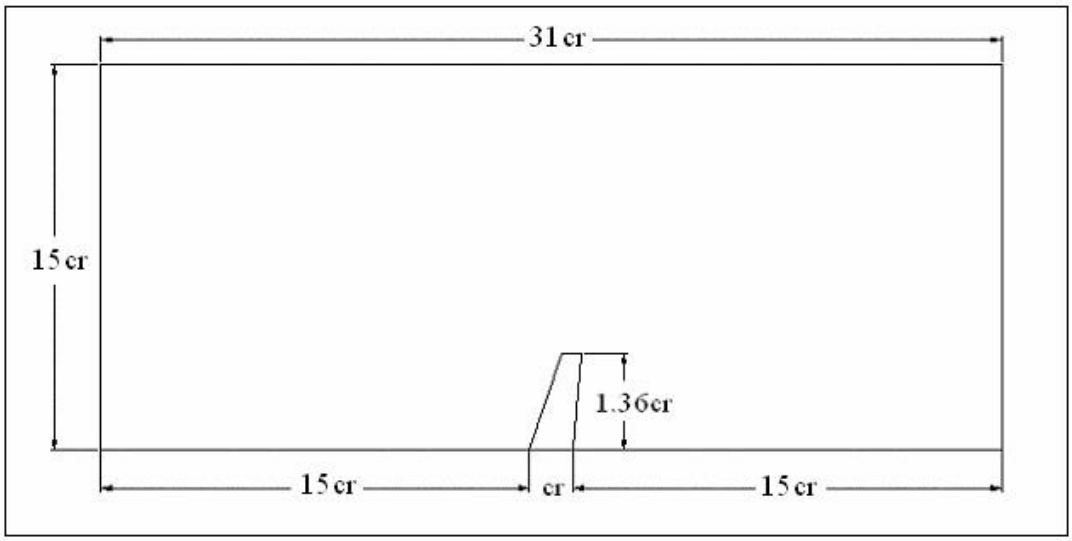

Figure 3.4 Dimensions of the Computational Domain.

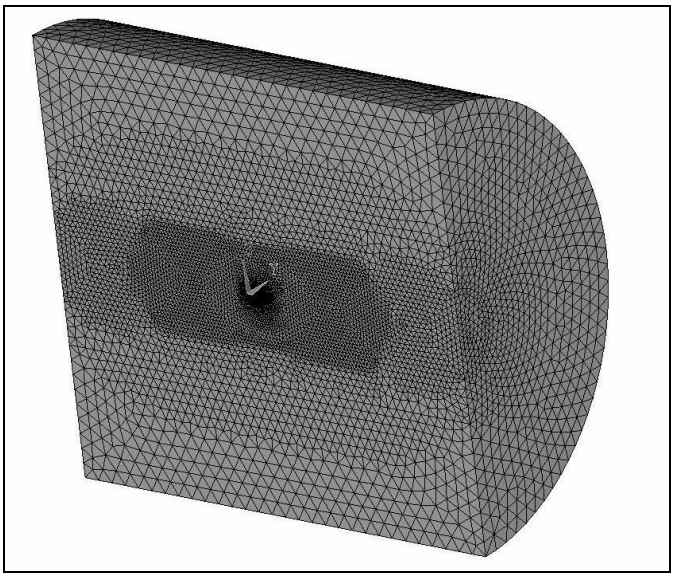

Figure 3.5 Half Cylinder Computational Domain.

The surface triangulations for four different CFD computational grids are given in Figure 3.6, and the number of boundary faces and boundary nodes for each grid is given in Table 3.3. Unstructured volume grids are shown in Figure 3.7 and the number of field elements and field nodes are given in Table 3.4.

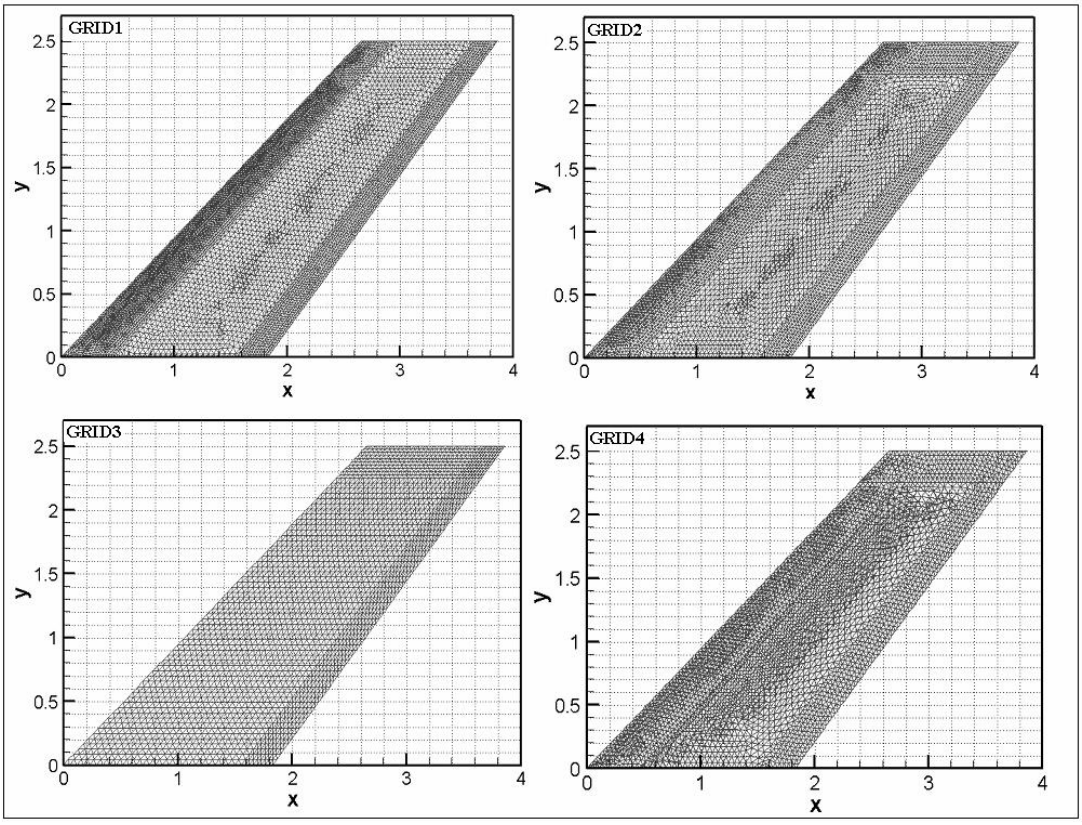

Figure 3.6 Wing Surface Triangulations

Table 3.3 Numbers of Surface Triangles and Nodes for Different CFD Grids

Mesh	Number of Surface Triangles	Number of Nodes
GRID1	19450	9805
GRID2	14706	7408
GRID3	9596	4834
GRID4	8746	4416

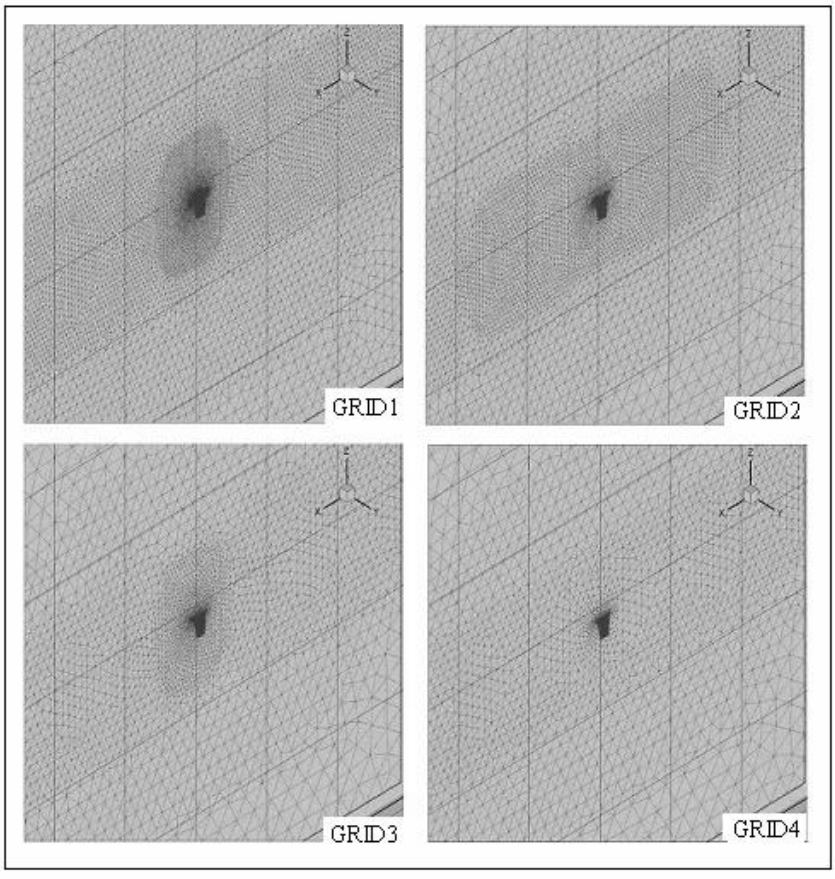

Figure 3.7 Unstructured Volume Grids.

Table 3.4 Numbers of Field Elements and Nodes for Different CFD Grids

Mesh	Number of Field Elements	Number of Boundary Nodes
GRID1	645784	119066
GRID2	615628	109693
GRID3	340532	61276
GRID4	189728	35657

These four different grids are tested in different flow conditions in order obtain minimum grid size which captures the physics of the flow. GRID4 has the minimum number of cells; it has nearly the same number of surface triangles as that of GRID3 but has approximately half number of tetrahedral elements. GRID1 and GRID2 have nearly same number of tetrahedral elements but GRID1 has finer surface resolution. In the following sections the results of the rigid wing CFD analysis made with these four different grids are given.

Flow Condition 1: M=0.85 $\alpha=5^o$

For M= 0.85 and $\alpha=5^o$, flow over the AGARD Wing 445.6 is solved using the grids described above. The pressure distributions obtained are shown in Figures 3.8-3.9 at two different spanwise locations.

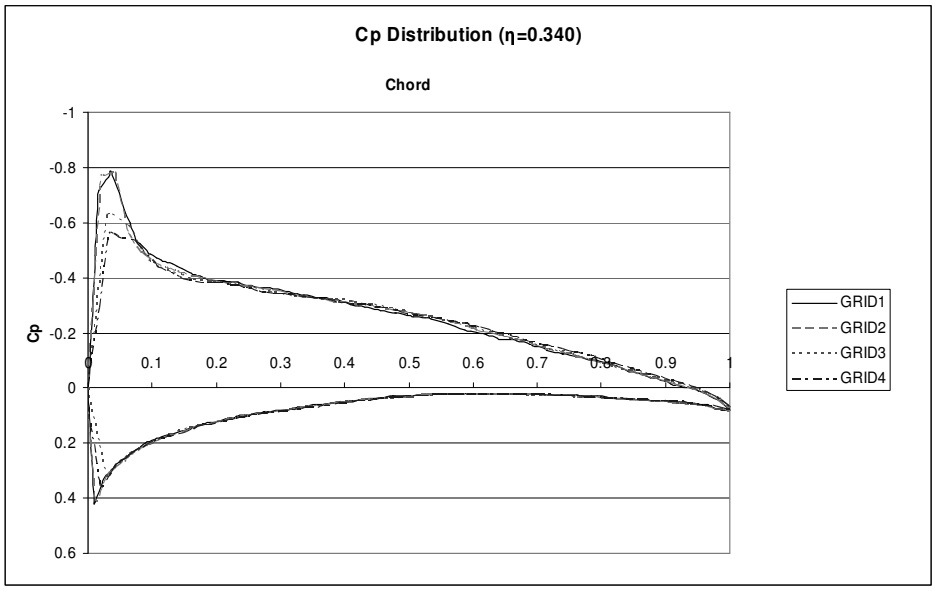

Figure 3.8 Wing Cp Distribution at 34 % Semispan (M=0.85 $\alpha=5^{o}$)

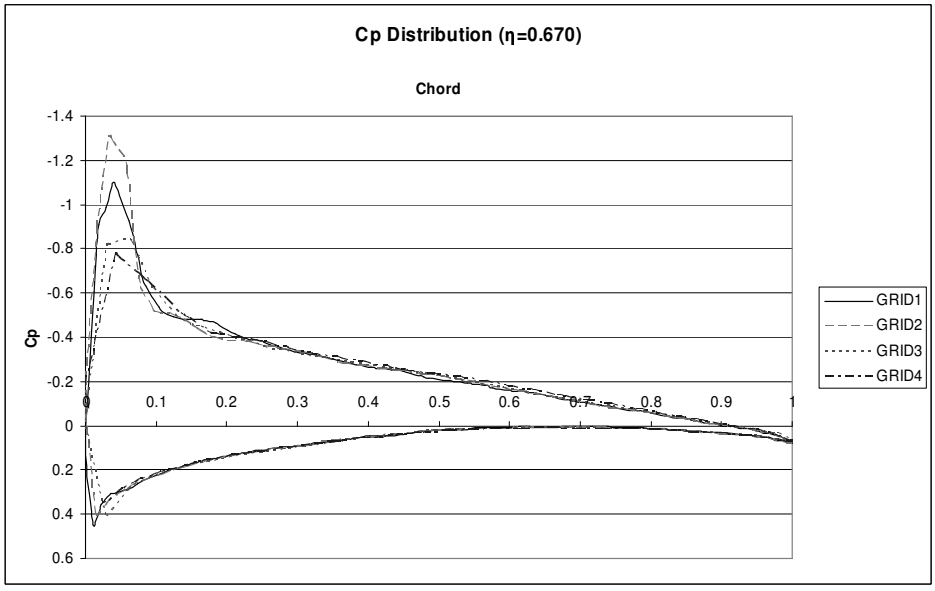

Figure 3.9 Wing Cp Distribution at 67 % Semispan (M=0.85 $\alpha=5^{o}$)

As shown in Figure 3.8 and 3.9, pressure distributions differ at the leading edge for coarse and fine grids.

At the inboard section (η=0.34) GRID4 predicts 30 % lower suction peak value as compared to GRID2, suction peaks are located at 3.46%-4.10% chord location, respectively.

At the outboard section (η=0.67), suction peaks predicted by GRID1 and GRID2 differ about 8 %, on the other hand coarse meshes predict approximately 60 % lower suction peak values. Suction peaks occur at %3.6-3.8 percent chord location for fine grids whereas for GRID3 and GRID4 it occurs at 6.2 %and 4.3 % chord locations, respectively.

Pressure coefficient contours over the wing upper and lower surfaces are shown in Figure 3.10.

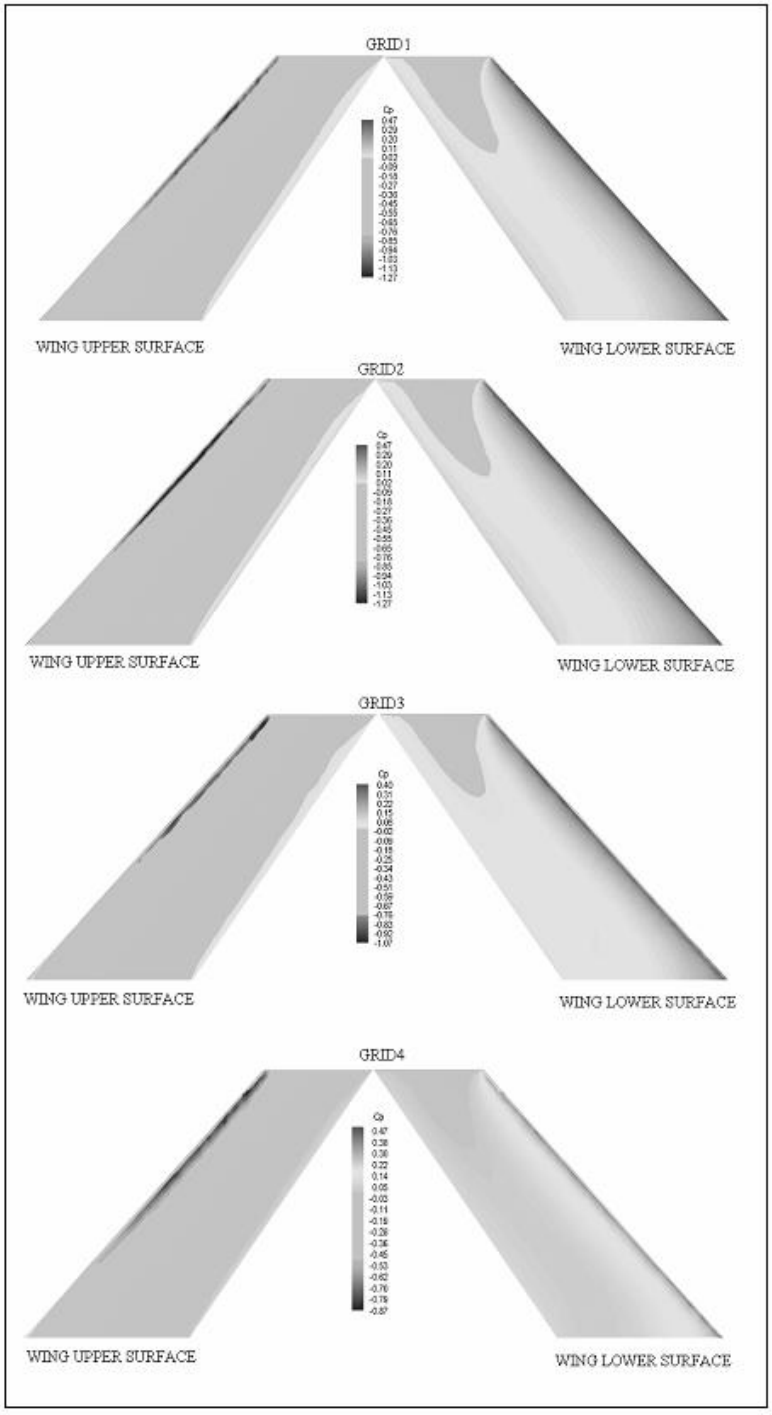

Figure 3.10 Pressure Coefficient Contours over AGARD Wing 445.6 (M=0.85 $\alpha=5^{o}$)

Flow Condition 2: M=0.96 α=0°

The pressure distributions on the upper surface of the wing for three different spanwise locations are similarly shown in Figure 3.11-3.13.

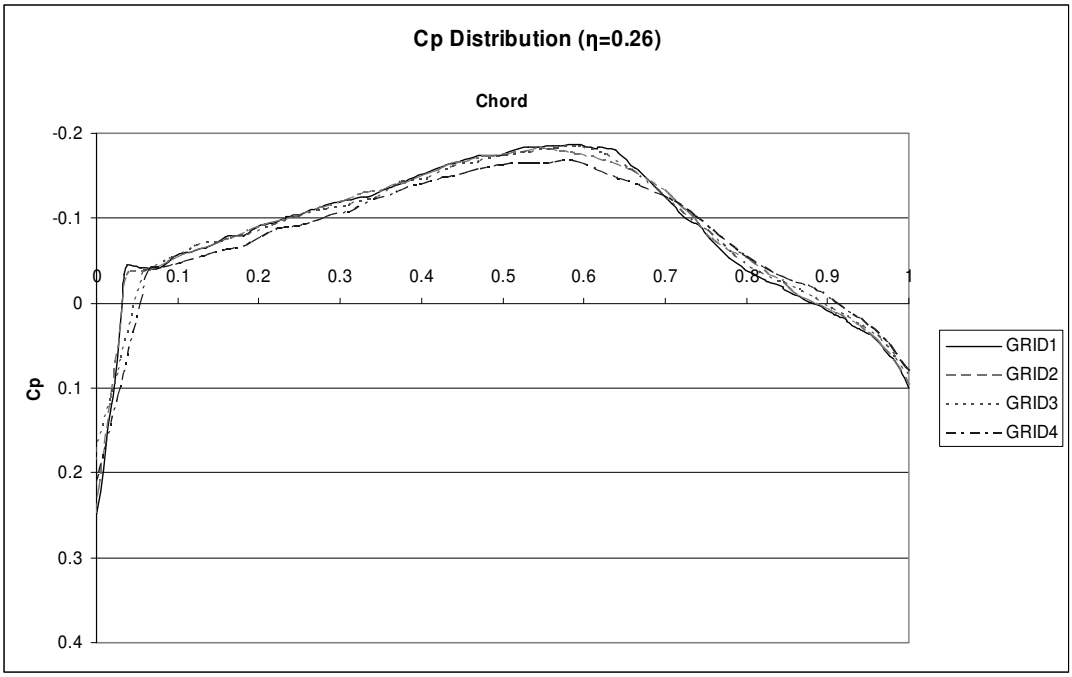

Figure 3.11 Wing Cp Distribution at 26 % Semispan (M=0.96 α=0°)

At η=0.26 location the flow solver predicts the maximum Cp value (Cp_{max}) of 0.249 for GRID1, 0.247 for GRID2, 0.184 for GRID3 and 0.214 for GRID4 at the leading edge. Flow solution with fine grids predicts nearly same Cp_{max}, whereas the flow solution with GRID3 and GRID4 predicts 25 % and 14 % lower Cp_{max} values, respectively.

Flow solver predicts suction peak of -0.183 at 59.2 % chord for GRID1 and a suction peak of -0.182 at 54.5 % chord for GRID2. Suction peak of -0.184 occurs at 59.4 % chord for GRID3 and suction peak of -0.168 occurs at 58.1 % chord for GRID4. Flow solution with GRID4 predicts 7.7 % lower suction peak value when compared to flow solution with GRID2.

Pressure coefficient is zero at 3.1 % and 88.3 % chord for GRID1, at 3.4 % and 88.2 % chord for GRID2, at 4.8 % and 89.3 % for GRID3 and 5.5% and at 90.8 % for GRID4. Pressure coefficient becomes zero at higher percent chord values for GRID4.

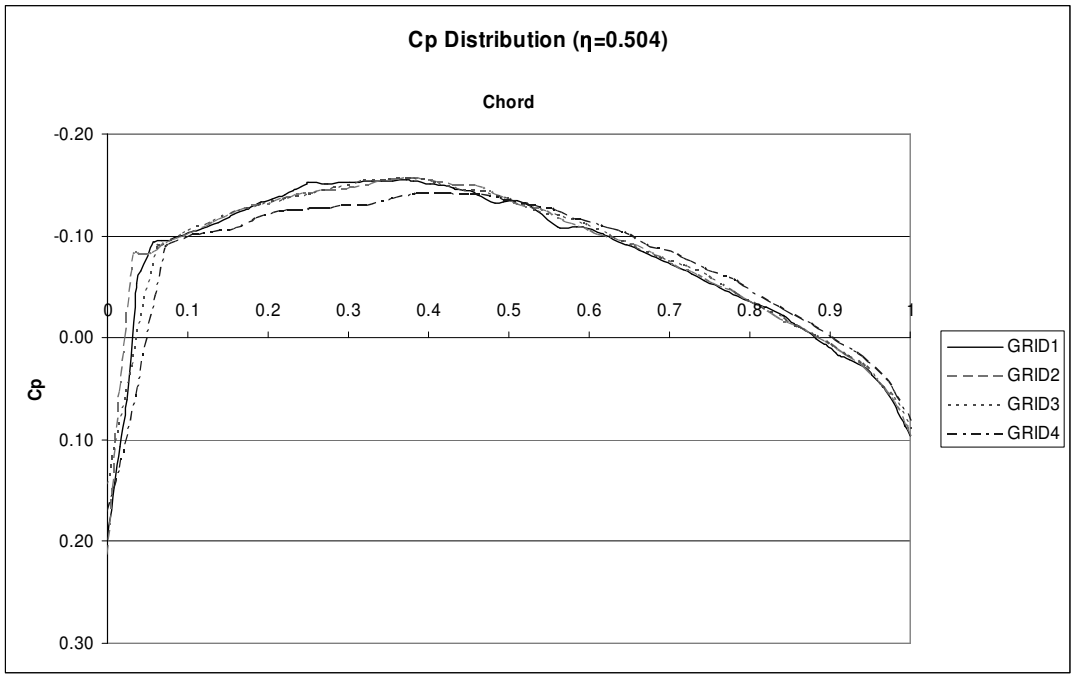

Figure 3.12 Wing Cp Distribution at 50.4 % Semispan (M=0.96 $\alpha=0^{o}$)

At η=0.504 location the flow solver predicts Cp_{max} of 0.198 for GRID1, 0.213 for GRID2, 0.144 for GRID3 and 0.171 for GRID4 at the leading edge. Flow solution with fine grids predicts nearly same Cp_{max}, whereas flow solution with GRID3 and GRID4 predicts 32 % and 20 % lower Cp_{max} values, respectively, when compared to GRID2.

Flow solver predicts suction peak of -0.155 at 37.2 % chord for GRID1 and a suction peak of -0.157 at 37.9 % chord for GRID2. Suction peak of -0.157 occurs at 38.1 % chord for GRID3 and suction peak of -0.142 occurs at 41 % chord for GRID4. Flow solution with GRID4 predicts 10 % lower suction peak value when compared to flow solution with GRID2.

Pressure coefficient is zero at 3.1 % and 88.3 % chord for GRID1, at 3.4 % and 88.2 % chord for GRID2, at 4.8 % and 89.3 % for GRID3 and 5.5% and at 90.8 % for GRID4.

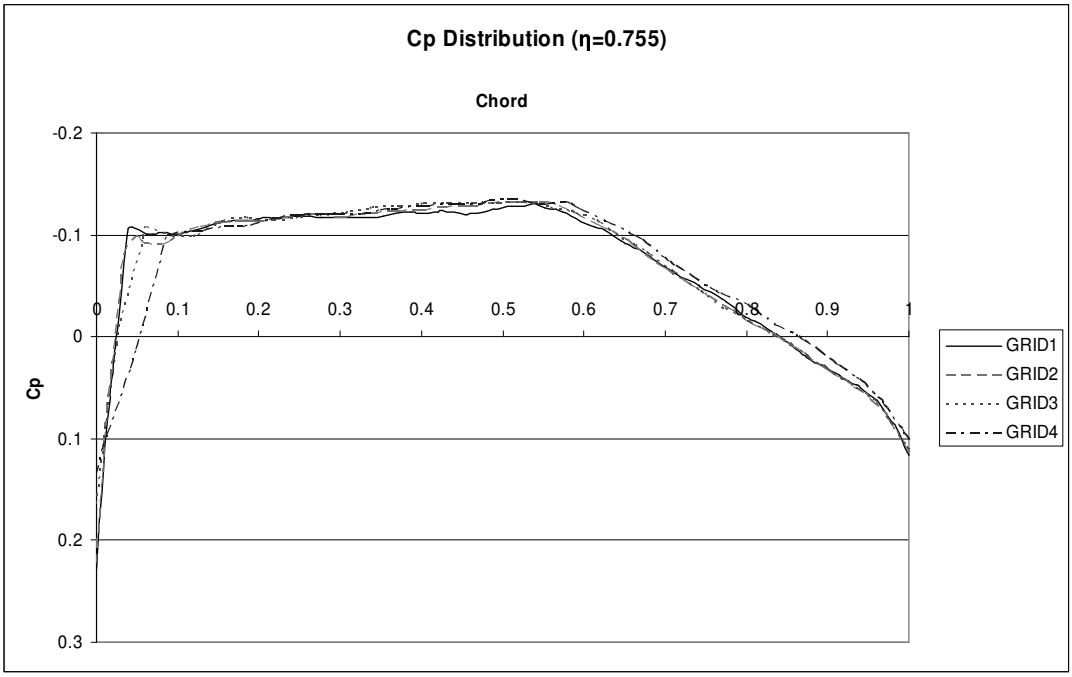

Figure 3.13 Wing Cp Distribution at 75.5 % Semispan (M=0.96 $\alpha=0^{o}$)

At η=0.755 location, the flow solver predicts Cp_{max} of 0.228 for GRID1, 0.222 for GRID2, 0.164 for GRID3 and 0.135 for GRID4 at the leading edge. Flow solution with fine grids predicts nearly same Cp_{max}, whereas flow solution with Grid 3 and Grid 4 predicts 26 % and 40 % lower Cp_{max} values, respectively, when compared to GRID2.

The solution predicts a suction peak of -0.132 at 53.7 % chord for GRID1 and a suction peak of -0.132 at 53.1 % chord for GRID2. A suction peak of -0.132 occurs at 52.7 % chord for GRID3 and a suction peak of -0.132 occurs at 57.1 % chord for GRID4. Flow solver predicts same suction peak values for each of the grids, but the suction peak occurs at a higher percent chord location for GRID4.

Pressure coefficient is zero at 2.5 % and 84 % chord for GRID1 and GRID2, at 2.9 % and 83.5 % for GRID3 and at 5.4% and 86 % for GRID4.

Pressure coefficient and Mach contours over AGARD Wing 445.6 are given in Figure 3.14 and 3.15, respectively.

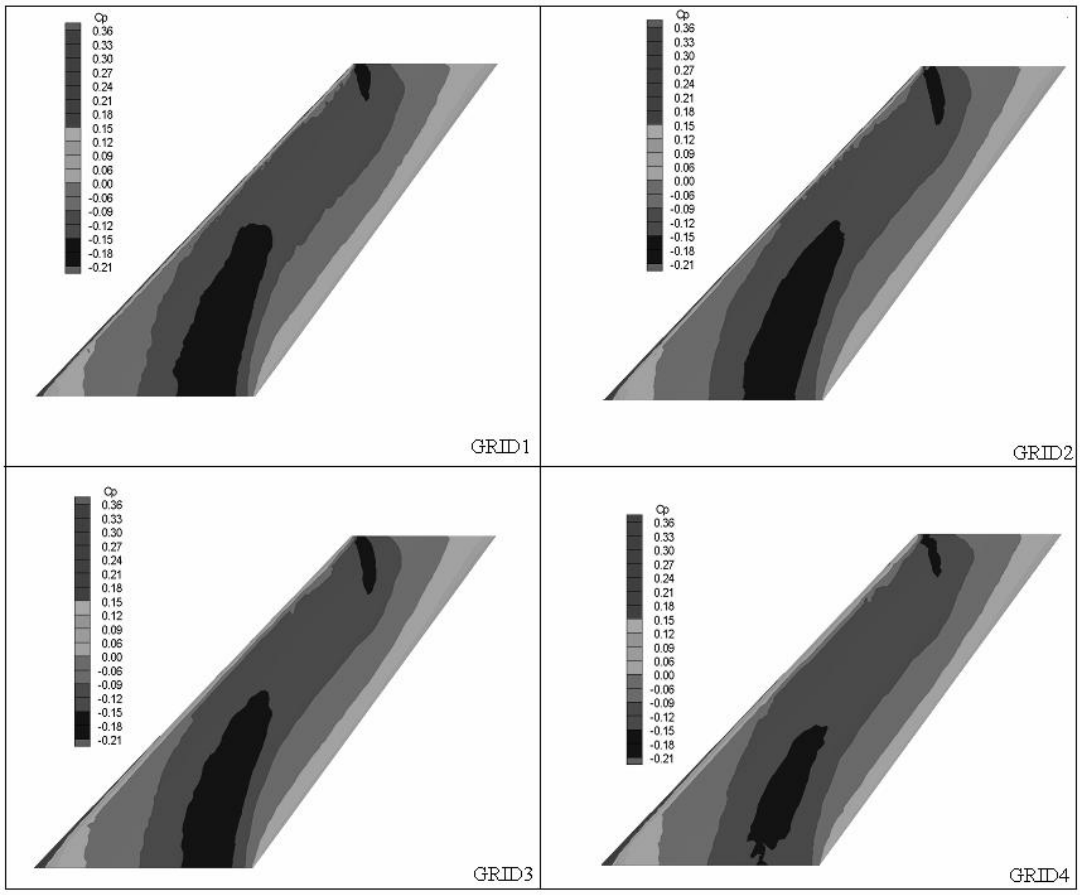

Figure 3.14 Pressure Coefficient Contours over AGARD Wing 445.6 (M=0.96 $\alpha=0^{o}$)

Figure 3.14 gives entire Cp distribution for four different grids. A large region of negative Cp occurs over the wing for each of the grids. Cp values of greater than 0.15 occurs at the entire leading edge for GRID1 and GRID2 but Cp values less than 0.15 present for GRID3 and GRID4 towards the tip of the wing.

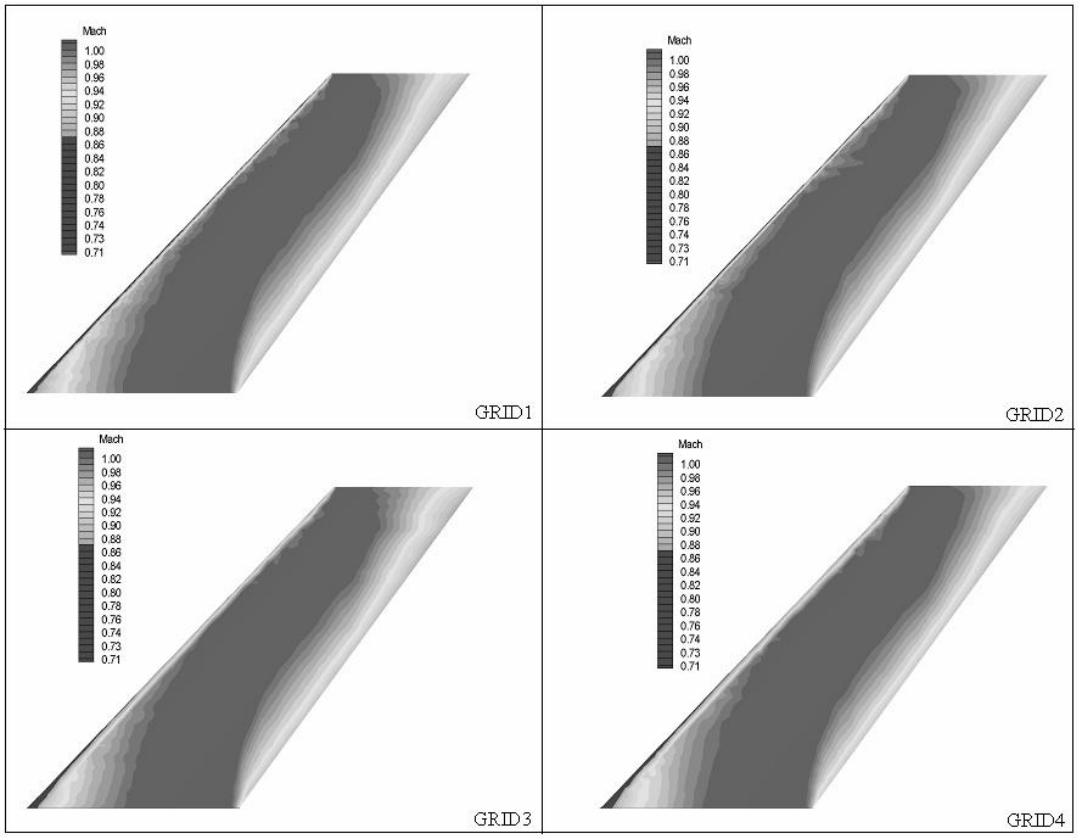

Figure 3.15 Mach Contours over AGARD WING 445.6 (M=0.96 $\alpha=0^{o}$)

A large region of M=1 flow is formed over the wing surface for each of the grids, but this high region of supersonic flow does not terminate with a shock.

Flow Condition 3: M=1.114 α=0°

The pressure distributions on the upper surface of the wing for three different spanwise locations are similarly shown in Figures 3.16-3.18.

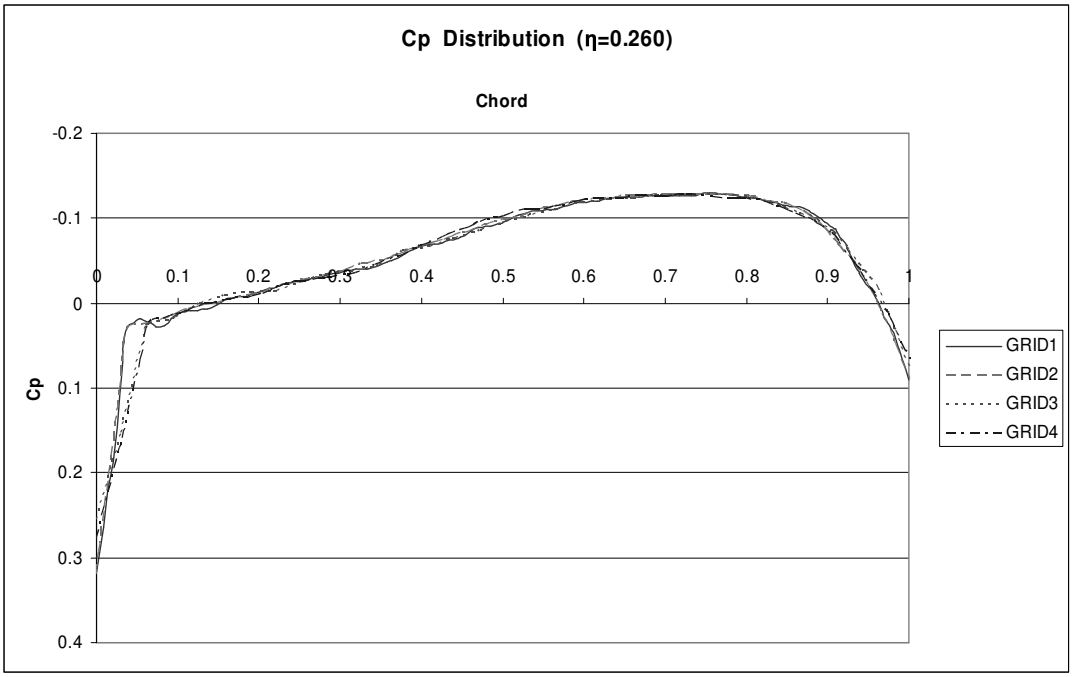

Figure 3.16 Wing Cp Distribution at 26 % Semispan (M=1.141 α=0°)

At η=0.26 location, the flow solver predicts Cp_{max} of 0.317 for GRID1, 0.318 for GRID2, 0.255 for GRID3 and 0.278 for GRID4 at the leading edge. Flow solution

with fine grids predicts nearly same Cp_{max}, whereas flow solution with Grid 3 and Grid 4 predicts 20 % and 12.5 % lower Cp_{max} values, respectively, when compared to GRID2.

Flow solver predicts a suction peak of -0.129 at 76.9 % chord for GRID1 and a suction peak of -0.129 at 73.6 % chord for GRID2. Suction peak of -0.127 occurs at 72.4 % chord for GRID3 and a suction peak of -0.128 occurs at 72.6 % chord for GRID4. Flow solver predicts same suction peak values for the fine grids and slightly lower values for coarse grids.

Pressure coefficient is zero at 15 % and 96 % chord for GRID1 and GRID2, at 12.8 % and 97 % for GRID3 and at 13.7% and 96.6 % for GRID4.

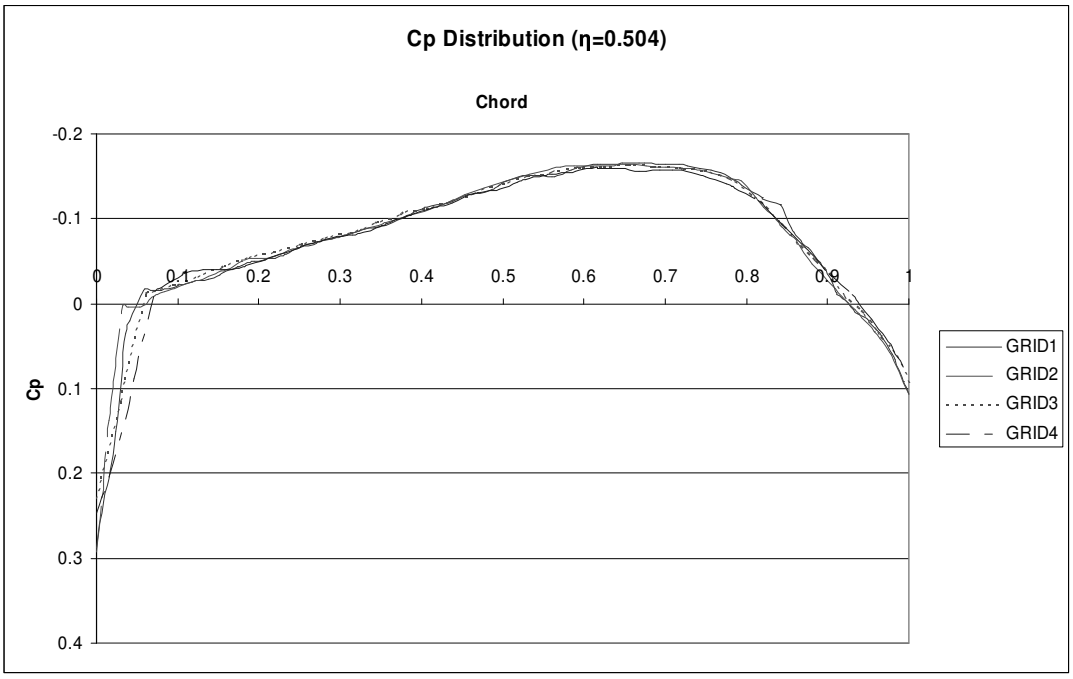

Figure 3.17 Wing Cp Distribution at 50.4 % Semispan (M=1.141 $\alpha=0^o$)

At η=0.504 location, the flow solver predicts Cp_{max} of 0.287 for GRID1, 0.293 for GRID2, 0.230 for GRID3 and 0.247 for GRID4 at the leading edge. Flow solution with fine grids predicts nearly same Cp_{max}, whereas flow solution with Grid 3 and Grid 4 predicts 21.5 % and 16 % lower Cp_{max} values, respectively, when compared to GRID2.

Flow solver predicts a suction peak of -0.166 at 67.4 % chord for GRID1 and a suction peak of -0.164 at 67.7 % chord for GRID2. Suction peak of -0.162 occurs at 66.1 % chord for GRID3 and suction peak of -0.160 occurs at 62.9 % chord for GRID4. Flow solver predicts nearly same suction peak values for the fine grids and slightly lower values for coarse grids.

Pressure coefficient is zero at 5 % and 92.4 % chord for GRID1, at 5.8 % and 92.7 % chord for GRID2, at 5.9% and 93 % for GRID3 and at 6.8% and 94 % for GRID4.

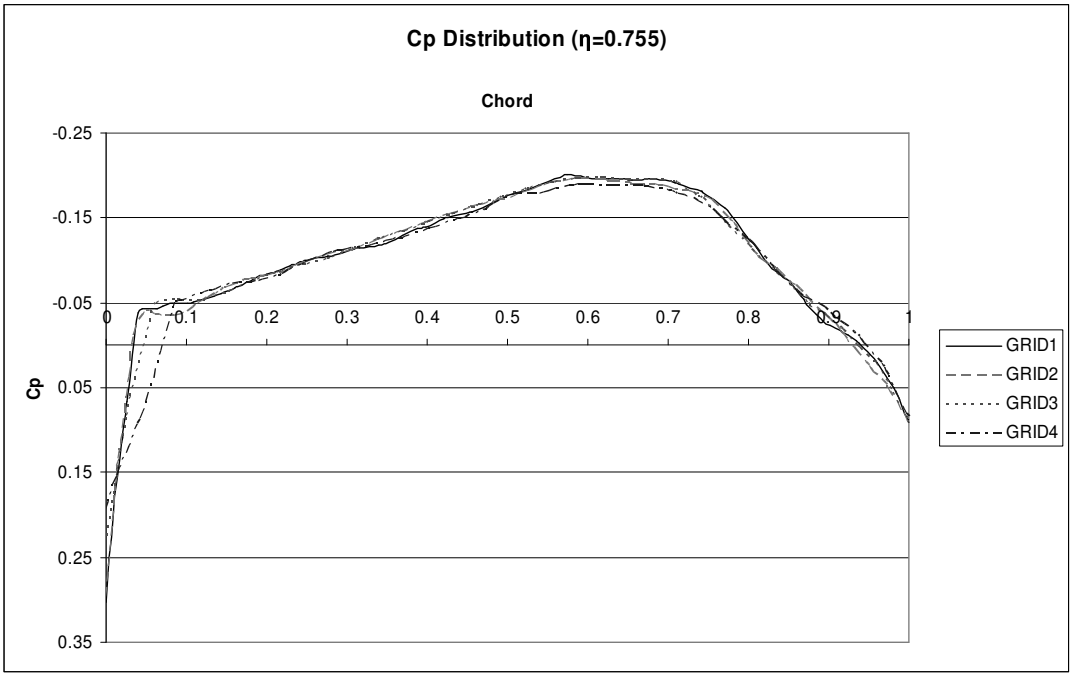

Figure 3.18 Wing Cp Distribution at %75.5 Semispan (M=1.141 $\alpha=0^o$)

At η=0.755 location, the flow solver predicts Cp_{max} of 0.303 for GRID1, 0.296 for GRID2, 0.234 for GRID3 and 0.194 for GRID4 at the leading edge. Flow solution with fine grids predicts nearly same Cp_{max}, whereas flow solution with Grid 3 and Grid 4 predicts 23 % and 36 % lower Cp_{max} values, respectively, when compared to GRID2.

Flow solver predicts suction peak of -0.201 at 57.5 % chord for GRID1 and a suction peak of -0.196 at 58 % chord for GRID2. Suction peak of -0.196 occurs at 58 % chord for GRID3 and suction peak of -0.189 occurs at 59.5 % chord for GRID4. Pressure coefficient is zero at 3.5 % and 94.1 % chord for GRID1, at 3.3 % and 93 % chord for GRID2, at 4.7% and 93 % for GRID3 and at 7 % and 95 % for GRID4.

Pressure coefficient and Mach contours over AGARD Wing 445.6 are given in Figures 3.19 and 3.20, respectively.

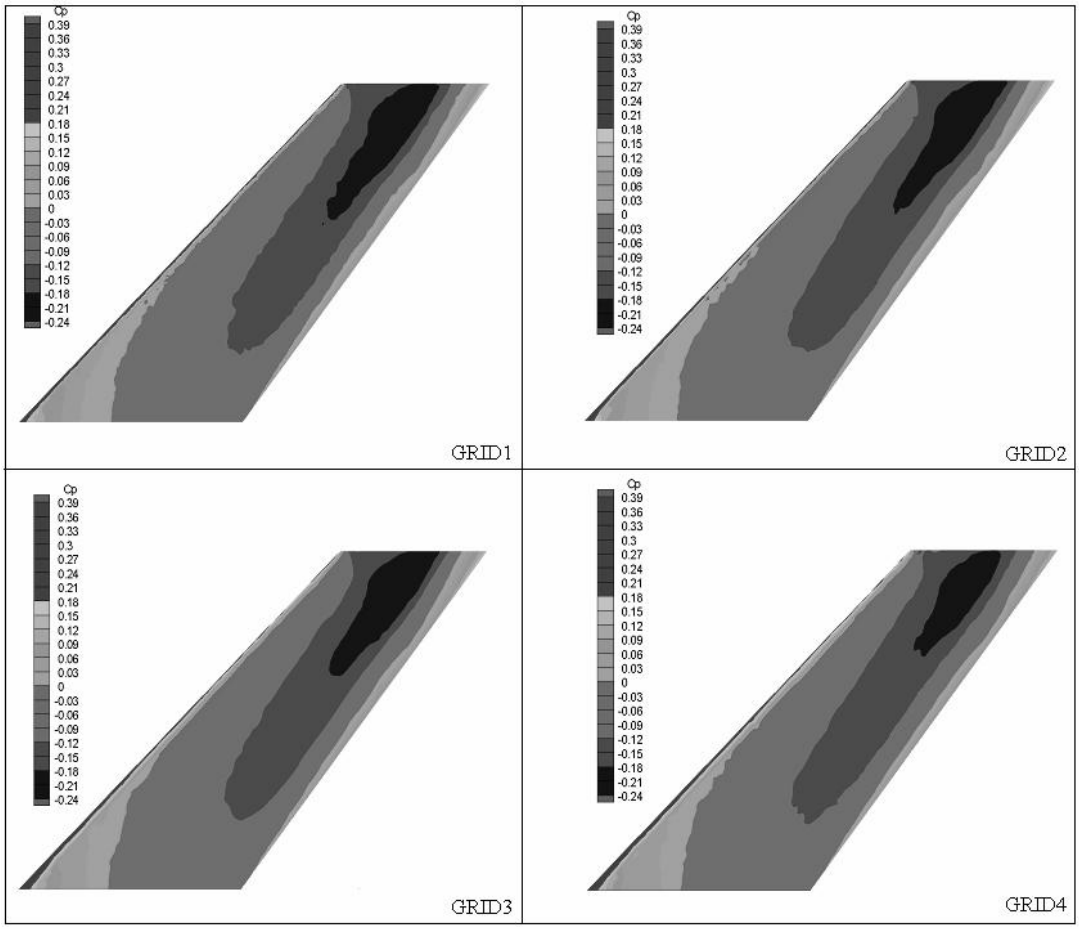

Figure 3.19 Pressure Coefficient Contours over AGARD Wing 445.6 (M=1.141 $\alpha=0^{o}$)

Figure 3.19 gives entire Cp distribution for four different grids. A large region of negative Cp occurs over the wing for each of the grids.

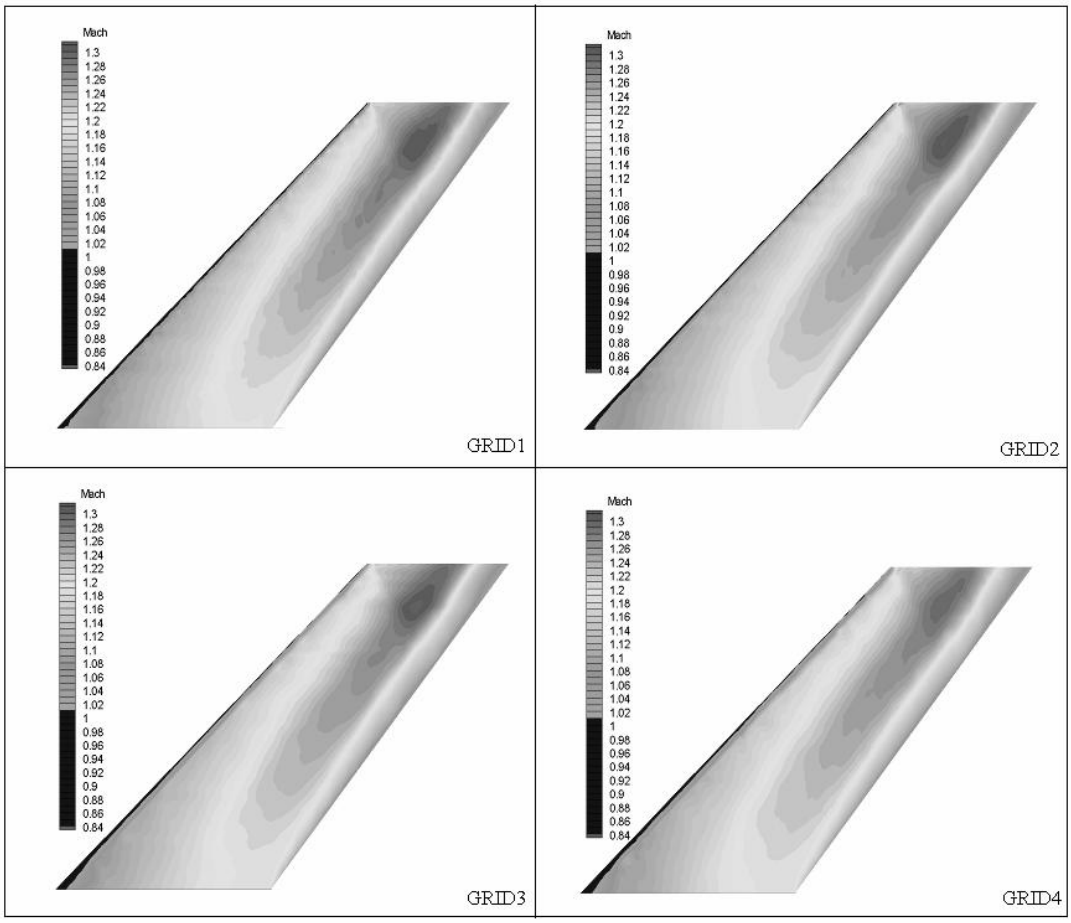

Figure 3.20 Mach Contours over AGARD Wing 445.6 (M=1.141 $\alpha=0^{o}$)

A large region of M>1 flow is formed over the wing surface for each of the grids.

Grid sensitivity analysis reveals that the flow solution with GRID4, which is the coarsest grid, appears to be a grid dependent solution for three flow conditions. Flow solution with GRID3 gives similar results with those of GRID1 and GRID2 in some cases, but for M=0.85 $\alpha=5^o$ flow condition it behaves like flow solution with GRID4. Among GRID1 and GRID2, GRID2 is selected for further studies, since it contains fewer elements when compared to GRID1. In the next section the computed flow fields obtained with GRID2 is compared against numerical work by Lee-Rausch [22] and Cai [25]

3.2.2 CFD Analysis – Comparison of Results

Flow Condition 1: M=0.85 $\alpha=5^o$

In these section pressure distributions over the wing is compared with that of Cai [25] at two different spanwise locations. This flow condition is taken for comparison, since Cai [25] solved static aeroelastic characteristics of AGARD Wing 445.6 at this flow condition. Pressure distributions are given in Figure 3.21-3.22.

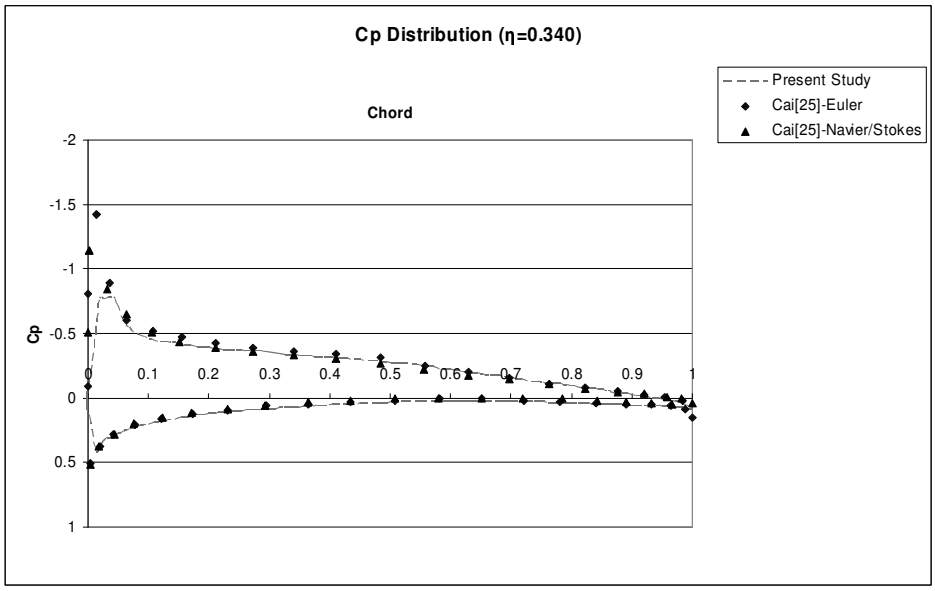

Figure 3.21 Comparison of Cp Distribution at 34 % Semispan (M=0.85,α=5^{o})

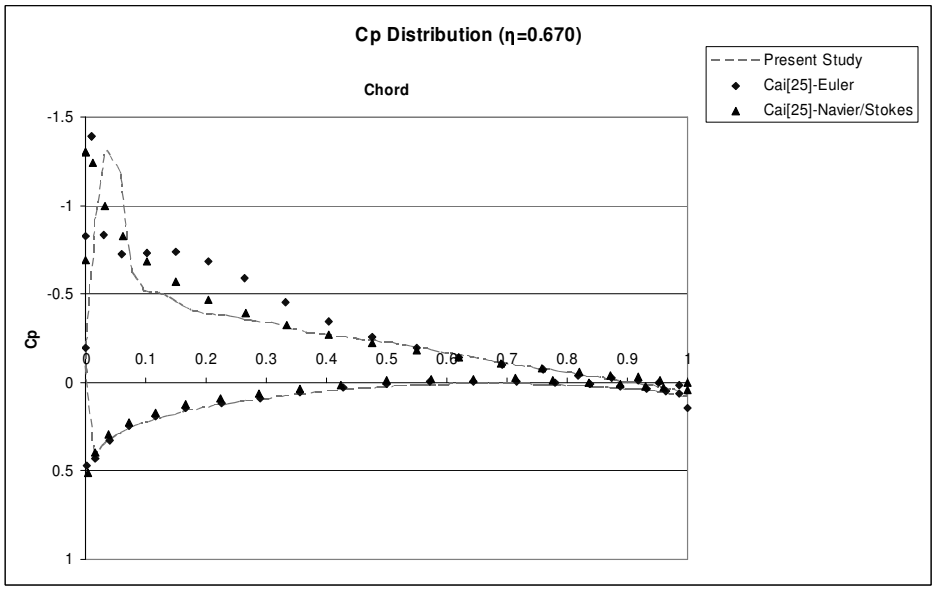

Figure 3.22 Comparison of Cp Distribution at 67 % Semispan (M=0.85, α=5^{o})

Results agree well to those of Cai [25] at the inboard section (η=0.34) except for suction peak at leading edge on the upper surface of wing. Cai [25] predicts a suction peak of –1.42 at 1.3% local chord; however the present study gives a suction peak –0.789 at 4 % local chord.

At the outboard section (η=0.67), Cai [25] predicts higher Cp values starting from 10 % local chord up to 40 % local chord. This behavior is attributed to an inviscid separation bubble near the tip of the wing, which is predicted by the Euler code [25]. However, this behavior was not observed in the Navier-Stokes solution of Cai [25] and is in more agreement with the present results at the outboard section as seen in Figure 3.22. In addition Cai [25] predicts a suction peak of –1.38 at 1 % local chord, which is slightly different from present study prediction which shows a suction peak of –1.30 at 3.6 % local chord.

The difference in the flow solution at leading edge may be attributed to the low resolution of the leading edge radius in the present study. The leading edge radius of AGARD Wing 445.6 is modeled but cannot be meshed, since the leading edge radius is very small compared to other dimensions of the wing. It should be noted that Cai [25] uses an O-Type structured grid which provides much better resolution at the leading edge Another contribute to the discrepancy may also the difference between the flow solvers.

Flow Condition 2: M=1.114 $\alpha=0^o$

In this section pressure distributions over upper surface of the wing for is compared with that of Lee-Rausch [22] at three different spanwise locations. Pressure distributions are given in Figures 3.23-3.25.

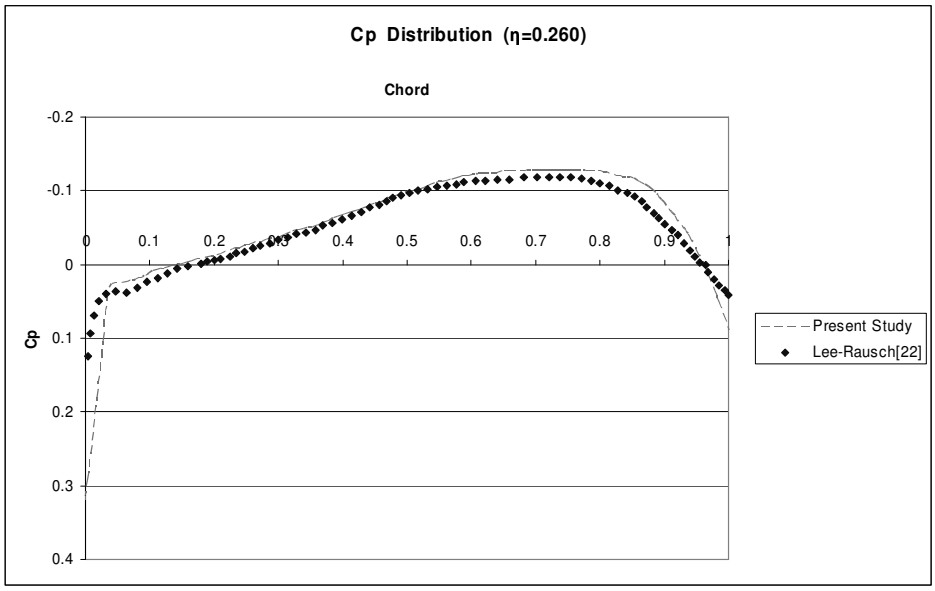

Figure 3.23 Comparison of Cp Distribution at 26 % Semispan (M=1.141, $\alpha=0^{o}$)

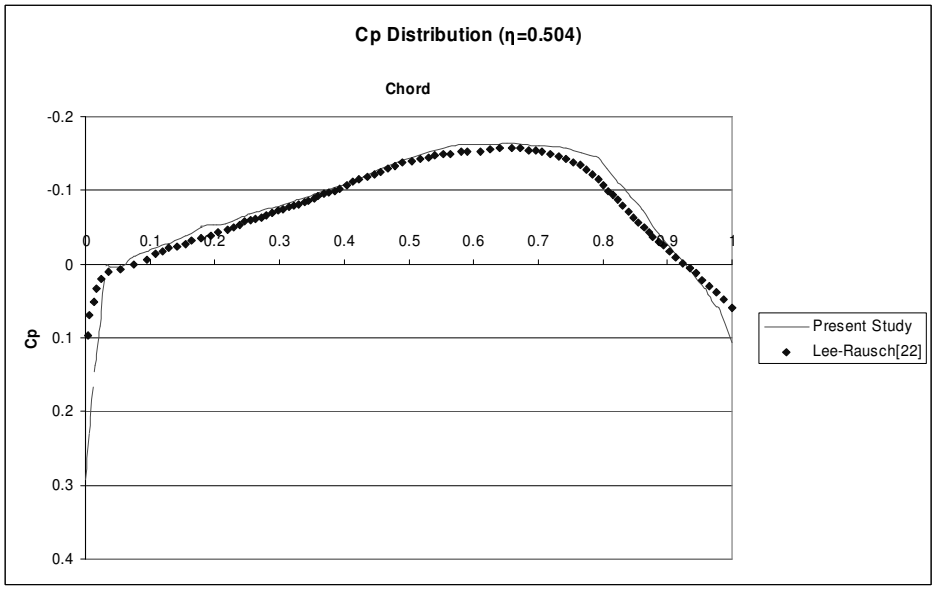

Figure 3.24 Comparison of Cp Distribution at 50.4 % Semispan (M=1.141, $\alpha=0^{o}$)

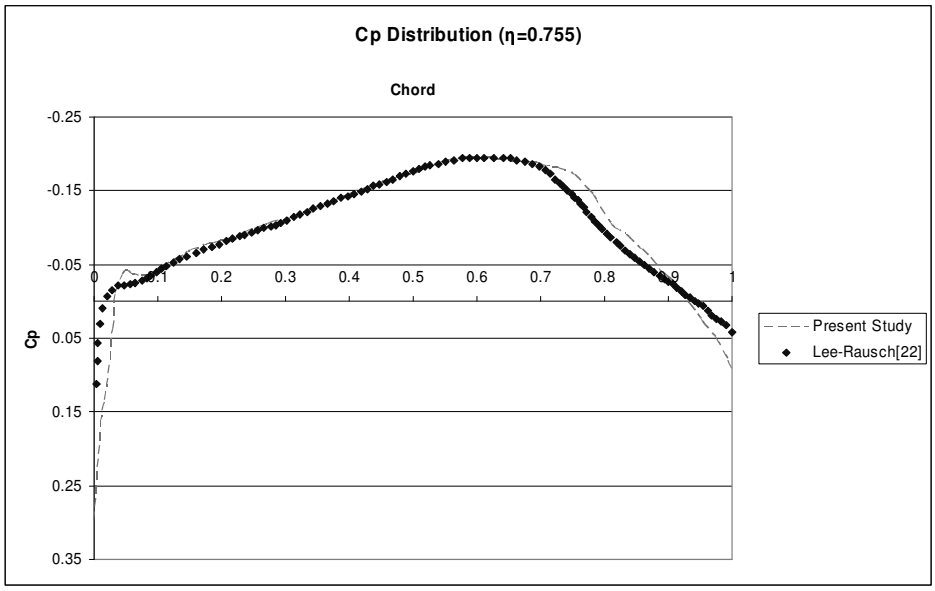

Figure 3.25 Comparison of Cp Distribution at 75.5 % Semispan (M=1.141, $\alpha=0^{o}$)

At this flow condition, the solution differs only in leading and trailing edge of the wing. Cp distributions follow the same path between 10% and 70% chord locations. Zero pressure coefficient locations differ slightly. Lee-Rausch [22] used a structured C-H type of grid which provides much better resolution at the leading and trailing edge when compared to the present study.

3.3 AGARD WING 445.6 MODAL ANALYSIS

In this section modal analysis of the AGARD Wing 445.6 is carried out in order to validate the present study finite element model of the wing which will be used in static calculations in the following sections.

Structural finite element models of the weakened wing are prepared for the solution of the static aeroelastic problem. ANSYS SOLID187 element, which has been

discussed in the previous chapter, is used for the finite element discretization. Finite element model is partially fixed at the root section. A grid sensitivity analysis for the flow solutions has already been performed in section 3.2. Since a matching discrete interface is employed at the fluid/structure interface grid sensitivity analysis is now performed for the structural grids. In the grids for structural analysis the wing surface grid distributions are the same with the flow field grid. Finite element models of the wing for each CFD grid is given in Figure 3.26

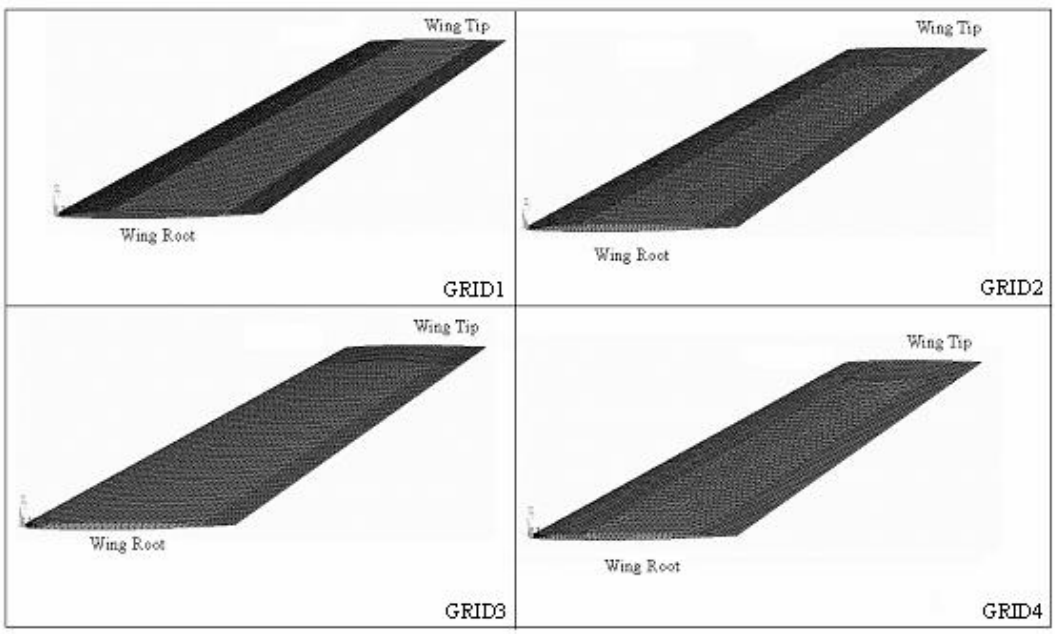

Figure 3.26 Finite Element Models of AGARD Wing 445.6

The number of SOLID187 elements used in each finite element model is given in Table 3.5.

Table 3.5 Number of SOLID187 Elements Used in Finite Element Models

FEM Model	Number of SOLID187 Elements
GRID1	29821
GRID2	22870
GRID3	14650
GRID4	13007

All of the finite element models have a volume of 0.159 ft^3, the mass of the weakened wing is obtained from Yates [21] as 0.12764 slugs, and density of mahogany is calculated as 0.799 $slug/ft^3$.

By using material properties given in Table 3.2 and calculated density value, modal analysis of 3-D weakened wing is performed using ANSYS. The first four frequencies are given in Table 3.6 for the four different finite element models along with those computed by Yates [21]. Percent error values of natural frequencies for each finite element model is given in Table 3.7

Table 3.6 Calculated Natural Frequencies for Weakened AGARD Wing 445.6

Natural Frequency (Hz)					
Mode Number	GRID1	GRID2	GRID3	GRID4	Yates [23]
1	9.891	9.963	10.032	10.116	9.60
2	37.64	37.70	38.79	39.17	38.10
3	49.86	50.29	51.04	51.72	50.70
4	92.9	93.15	94.82	97.26	98.50

Table 3.7 Percent Error Values for Finite Element Models

Natural Frequency (Hz)				
Mode Number	GRID1 % Error	GRID2 % Error	GRID3 % Error	GRID4 % Error
1	3.03	3.78	4.50	5.37
2	1.22	1.05	2.86	3.85
3	1.68	0.81	1.48	2.82
4	5.60	5.43	3.73	1.26

Percent errors in natural frequencies increase with decreasing element number for the first 3 modes, but a decrease in percent error value for the 4^{th} mode shape is observed with decreasing element number.

Considering the percent error values given in Table 3.7 and the grid sensitivity study given earlier in Section 3.2 for flow solutions, now GRID2 model is selected for use in the following aeroelastic validation studies.

In addition to the calculated modal frequencies, mode shapes of the structure are also calculated. The mode shapes, which are mainly based on wing out-of-plane deflection values, are compared to those of Kolonay [44]. Results obtained from 3D finite element analysis of the wing are scaled up so that the maximum deflection values are same that of Kolonay [44], then minimum deflection values are compared in Table 3.8.

Table 3.8 Comparison of Minimum Deflection Values

Mode	Present Study Min	Kolonay[44] Min
1	-0.00354	-0.08551
2	-26.099	-25.09
3	-28.502	-27.17
4	-24.352	-22.62

The wing mode shapes calculated in the present study are compared with those of Kolonay in Figures 3.27-3.30. Out of plane deflection values of the present study model is scaled up so that maximum deflection values are same with that of Kolonay [44]. There is an 180^{o} shift in the second mode shape, which is due to the difference of solvers. The results of the modal analysis are in admissible levels and the present study finite element model can be used in the further static finite element analysis.

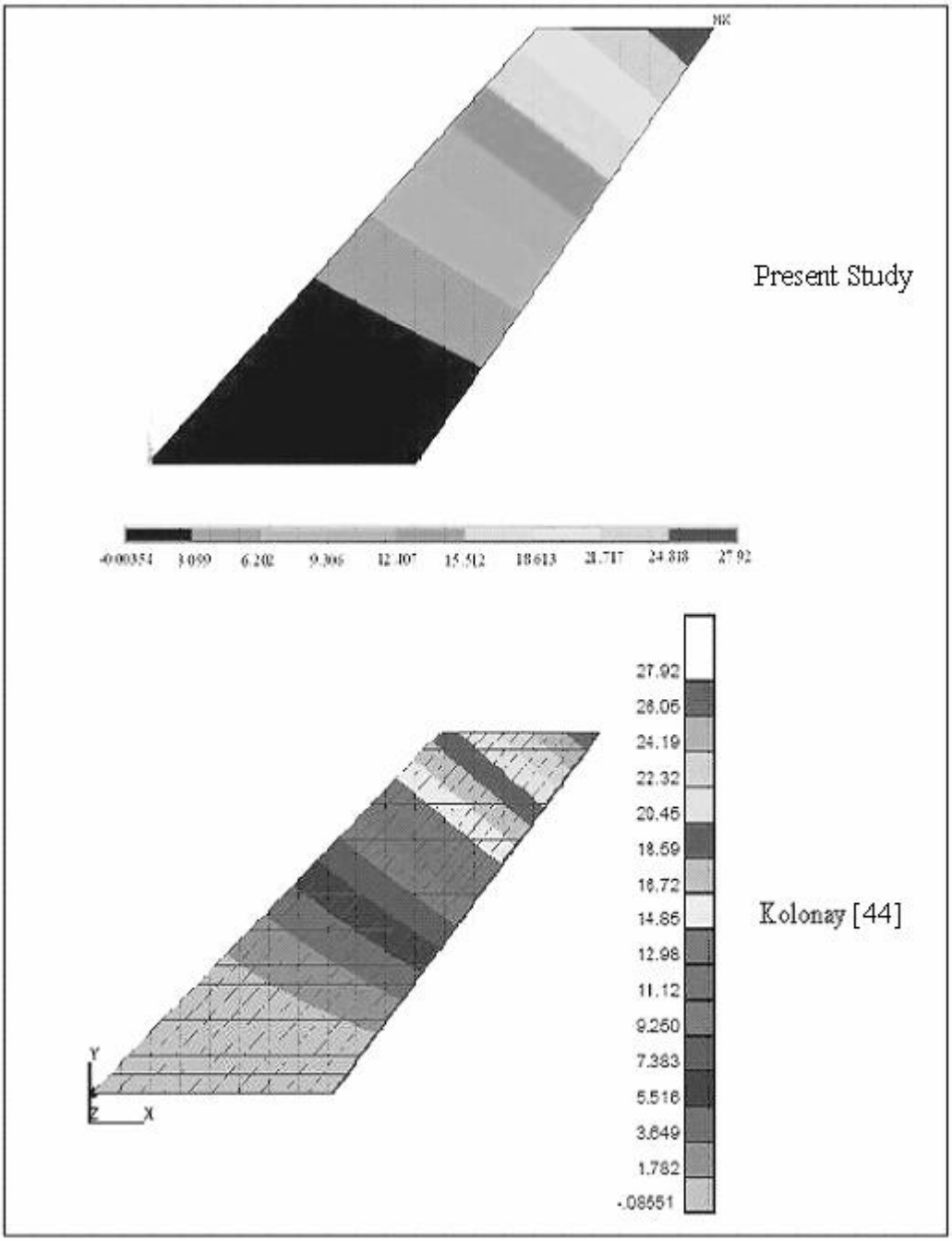

Figure 3.27 Mode Shape 1

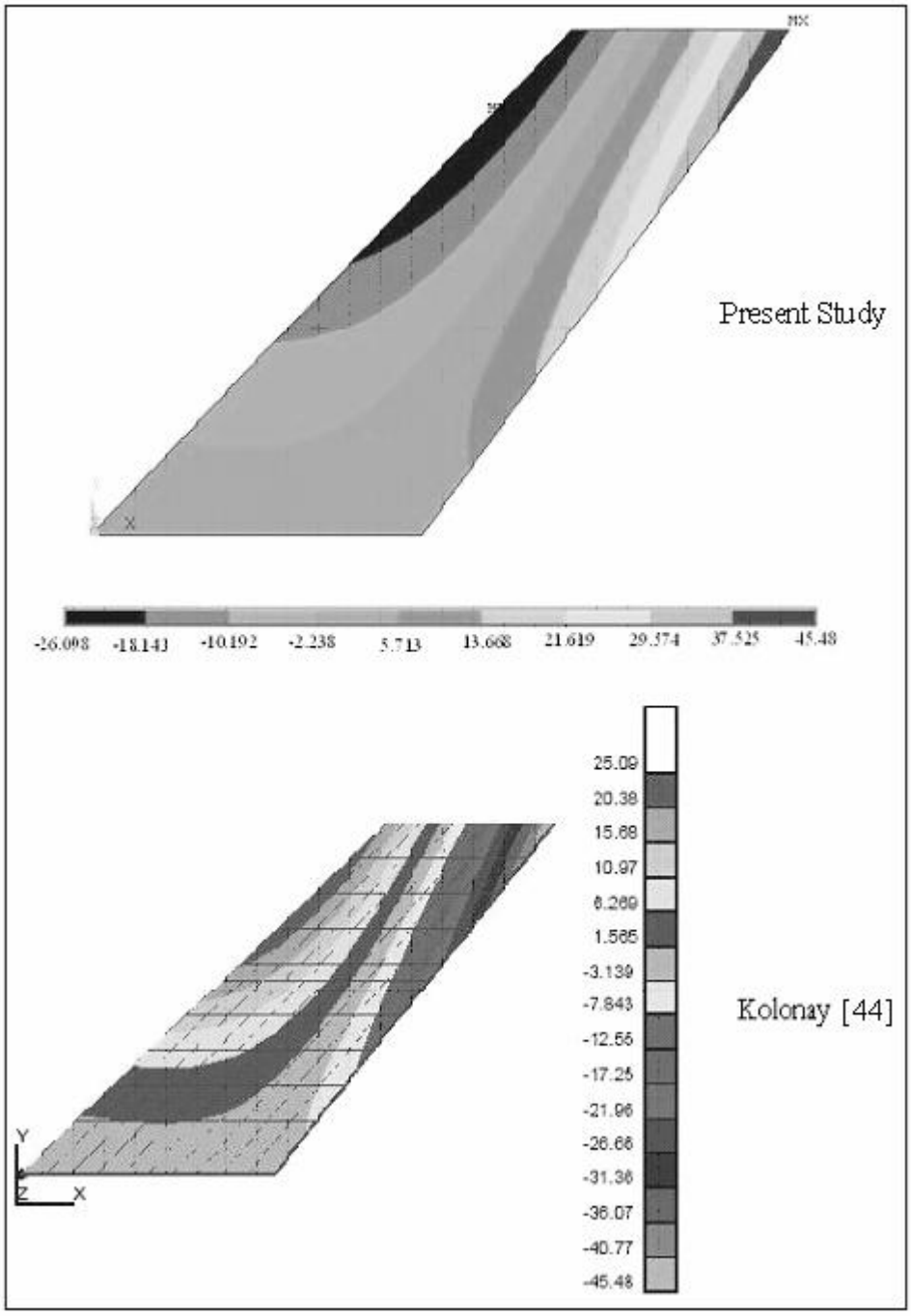

Figure 3.28 Mode Shape 2

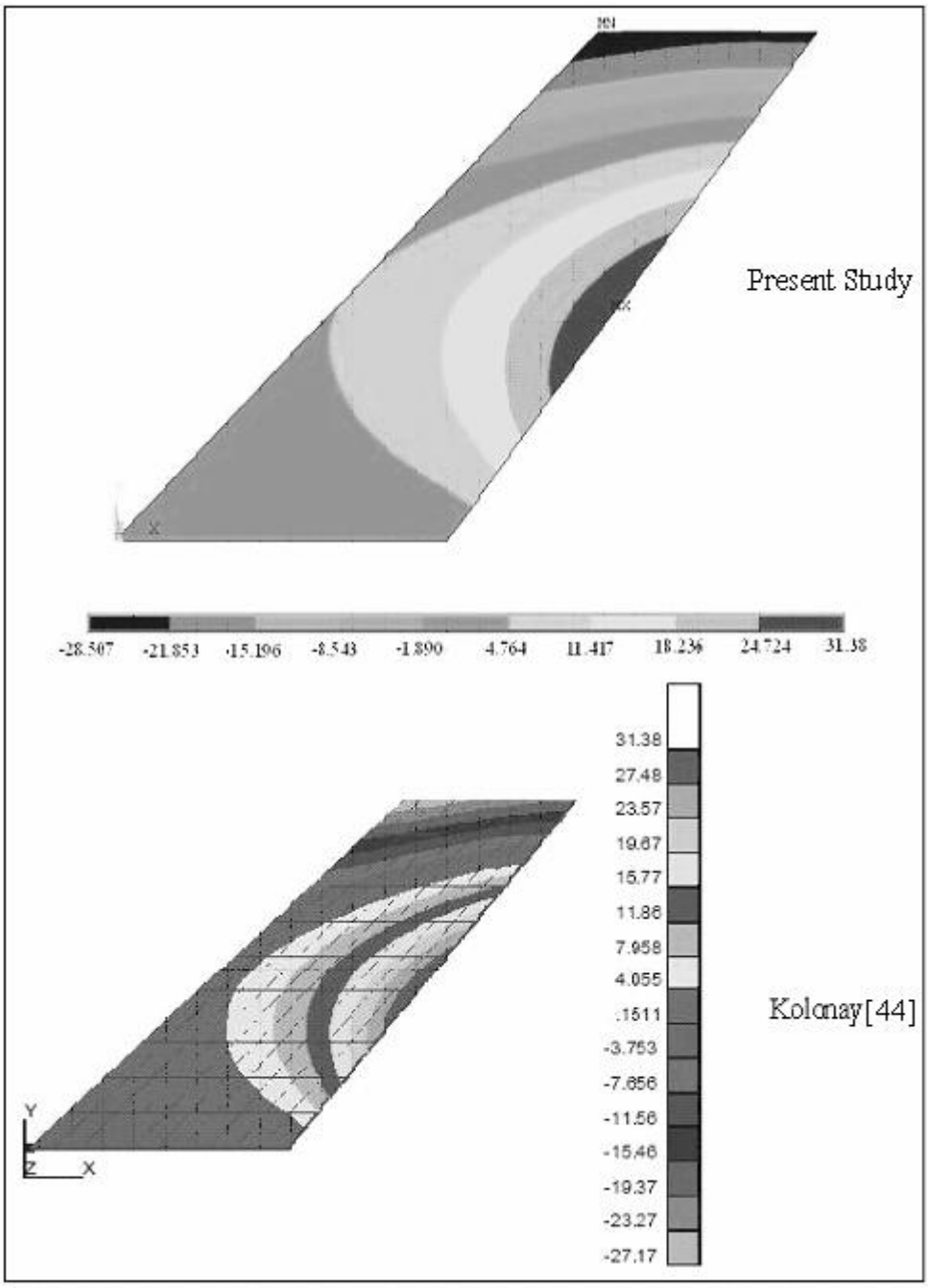

Figure 3.29 Mode Shape 3

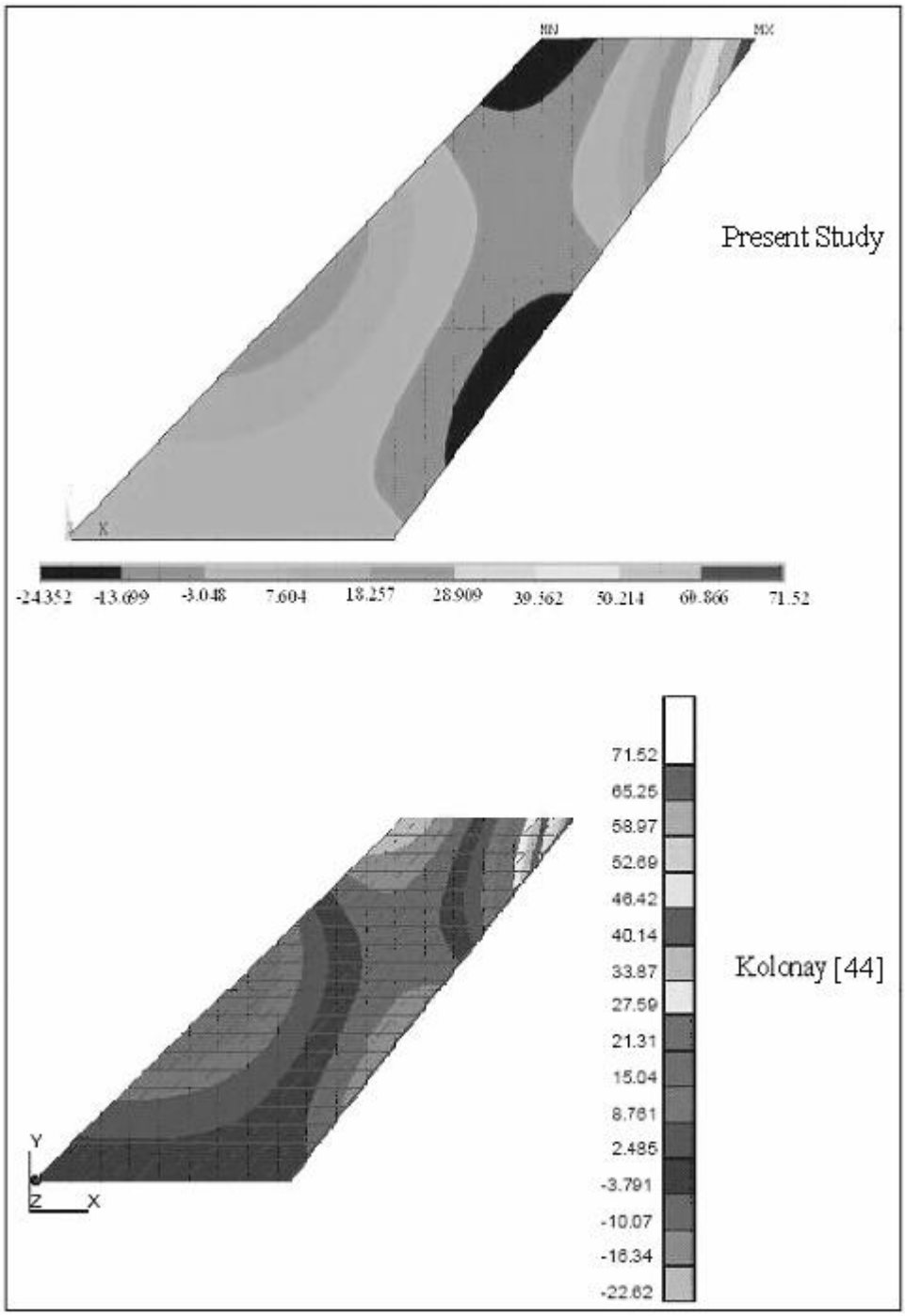

Figure 3.30 Mode Shape 4

3.4 AGARD WING 445.6 STATIC AEROELASTIC ANALYSIS

In this section static aeroelastic analysis of AGARD Wing 445.6 is performed using the developed computational aeroelastic procedure. A converged flow solution is obtained at the beginning of the static aeroelastic iterations and this flow solution over the rigid wing is used as an initial condition to the aeroelastic iterations. Nodal displacement values at the wing structural grid points are calculated upon application of aerodynamic loads via the finite element analysis of the wing. Displacements over the wing surface are reflected on the flow domain and aerodynamic loads on the deformed wing are again calculated using the flow solver. This iterative process continues until RMS values of nodal displacements between two consecutive aeroelastic iterations falls below a prescribed tolerance. A tolerance value of 10^{-7} ft is used in the analyses of AGARD Wing 445.6.

The convergence history for rigid and elastic wings is shown in Figure 3.31. Flow over the rigid wing is computed until CFD residuals reduce below two order of magnitudes, which takes about 3000 time steps with CFL=3. Once the converged solution is obtained, computational aeroelastic analysis of the wing is turned on and the aeroelastic iterations start. The location of the flow domain nodal grid points is updated at every 100 CFD time steps based on the results of FE analysis. In Figure 3.31, the spike at time step=3000 is due to the start of aeroelastic iterations. Rms of nodal displacements falls below the tolerance value after 32 aeroelastic iterations, which corresponds to 3200 CFD time steps.Lift coefficient of rigid and elastic wings are given in Figure 3.32.

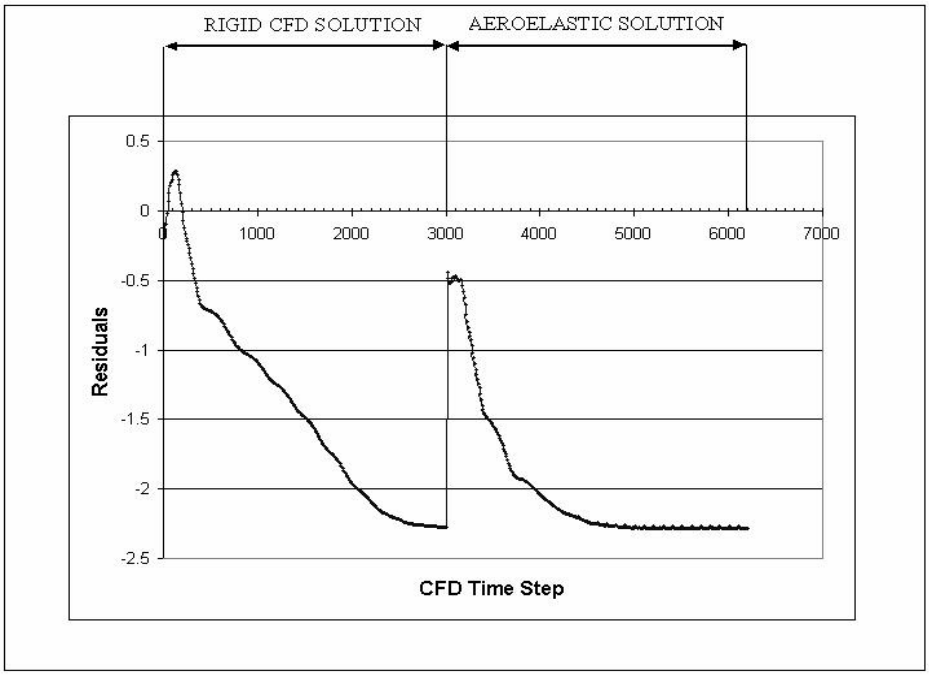

Figure 3.31 Convergence History for Rigid and Elastic Wings.

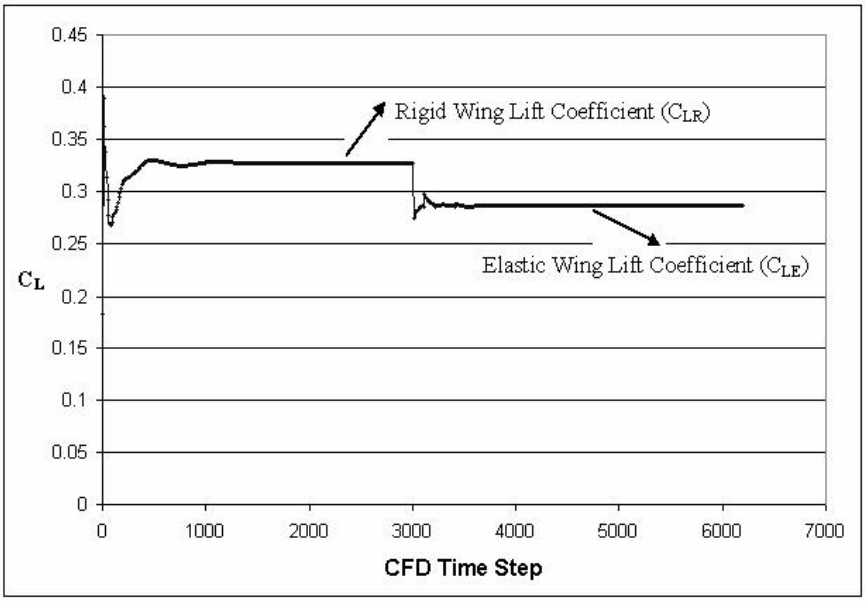

Figure 3.32 Lift Coefficients for Rigid and Elastic Wings.

Rigid wing lift coefficient, elastic wing lift coefficient and percent reduction in lift coefficient due to the wing elasticity predicted in the present study are given together with those were predicted by Cai [25] in Table 3.9

Table 3.9 Comparison of Rigid Wing and Elastic Wing Lift Coefficients

	Rigid Wing Lift Cefficient C_{LR}	Elastic Wing Lift Cefficient C_{LE}	% Reduction
Present Study	0.328	0.287	12.5
Cai [26]Euler	0.370	0.288	22.1
Cai [26] N/S	0.339	0.288	15.0

Euler solution of Cai [25] predicts a higher value of rigid wing lift coefficient. However, Navier/Stokes solution of Cai [25] predicts a rigid wing lift coefficient of 0.339, which is 3.2 % higher than rigid wing lift coefficient predicted by the present study. Whereas elastic wing lift coefficient of Cai [25] are the same for both Euler and Navier/Stokes solutions. Elastic wing coefficient predicted by the present study is about 0.3 % smaller than the one predicted by Cai [25].

Rigid and elastic wing Cp distributions calculated in the present study are given in Figures 3.33-3.34 for two different spanwise locations.

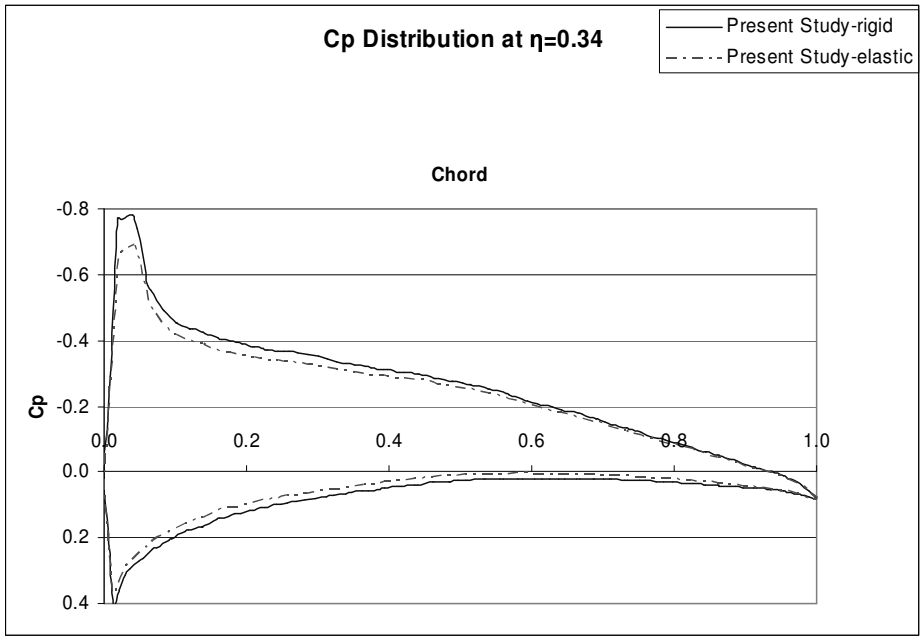

Figure 3.33 Elastic and Rigid Wing Cp Distributions at 34 % Semispan

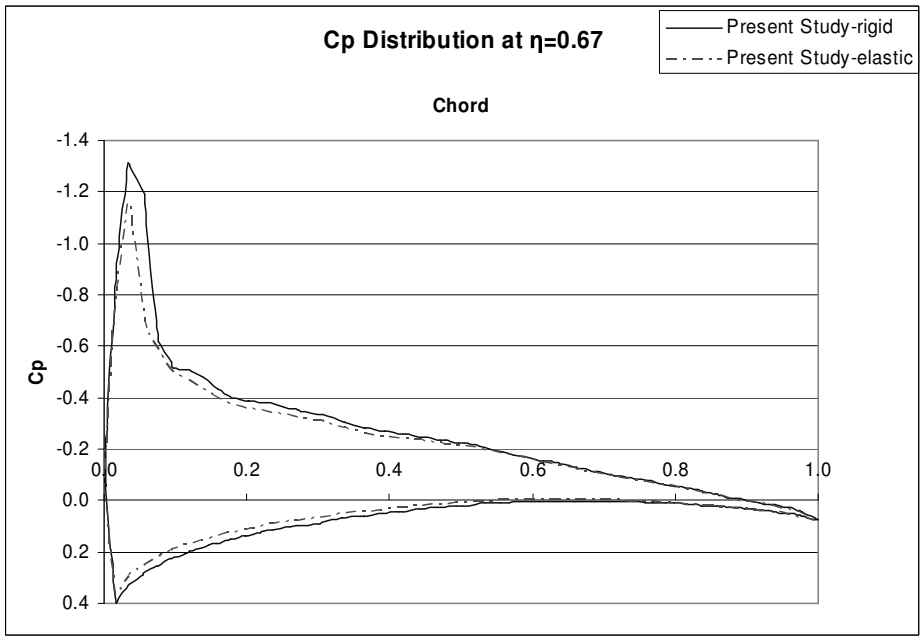

Figure 3.34 Elastic and Rigid Wing Cp Distributions at 67 % Semispan

The suction pressures on the upper wing surface are reduced in elastic wing case as seen in Figures 3.33-3.34. The lift is similarly reduced by about 12.5% when compared to rigid wing case.

Non-dimensional pressure contours over elastic and rigid wings are given in Figure 3.35.

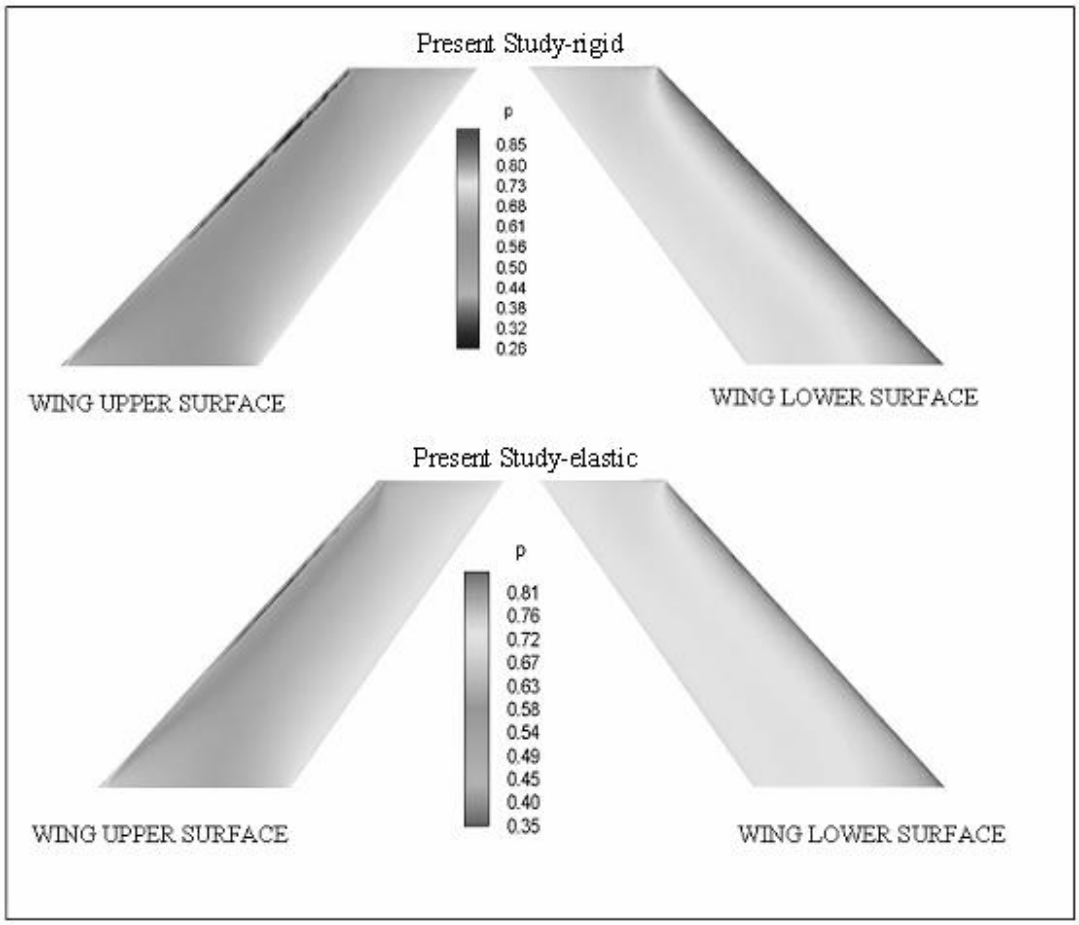

Figure 3.35 Elastic and Rigid Wing Non-dimensional Pressure Contours

Elastic wing pressure distributions at two different spanwise locations are compared with the results of Cai [25] in Figures 3.36-3.37.

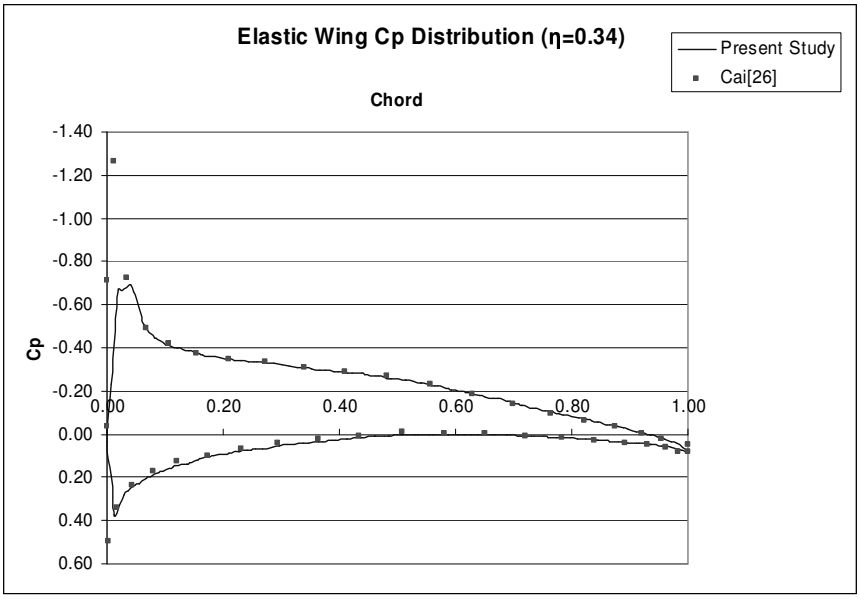

Figure 3.36 Comparison of Elastic Wing Cp Distribution at 34 % Semispan

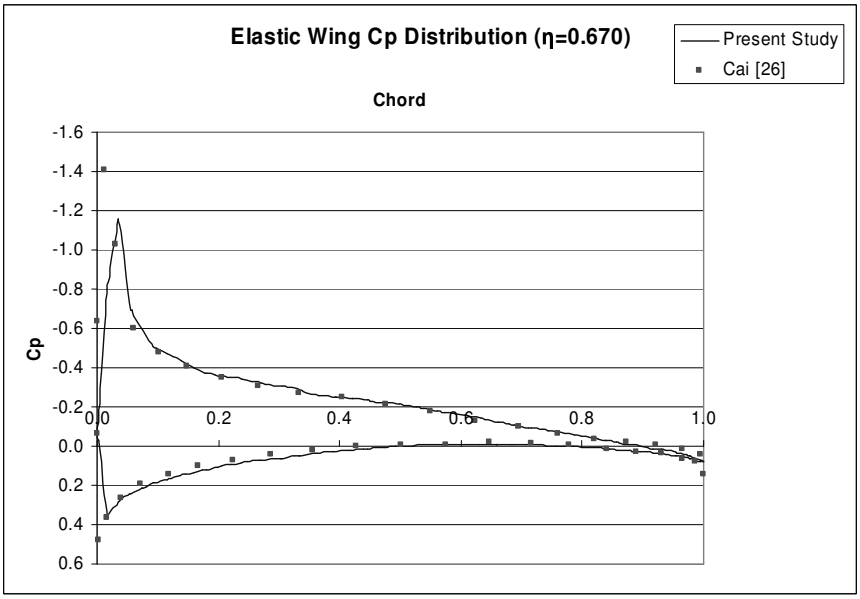

Figure 3.37 Comparison of Elastic Wing Cp Distribution at 67 % Semispan

At the inboard section of the wing (η=0.34) Cai [25] predicts a suction peak of –1.26 at 1 % chord location at the upper surface of wing. At this section the present study results show a suction peak of –0.7 at 4 % chord location. At the outboard section (η=0.67) Cai [25] predicts a suction peak of –1.41 at 1 % local chord at the upper surface wing; on the other hand, the present study results predict a suction peak of –1.13 at 3.6 % chord. As shown in Figures 3.36-3.37, present study pressure predictions for elastic wing are well suited to results of Cai [25] except for the leading edge section.

The comparison of equilibrium positions for rigid and elastic wings is given in Figure 3.38

Figure 3.38 Initial and Equilibrium Positions of AGARD Wing 445.6

Deformation of AGARD Wing 445.6 at the leading and trailing edges at M=0.85, $\alpha=5^{o}$ and $q_{\infty}=64.2$ lbf/ft^2 is given in Figures 3.39 and 3.40 along with the results of Cai [25].

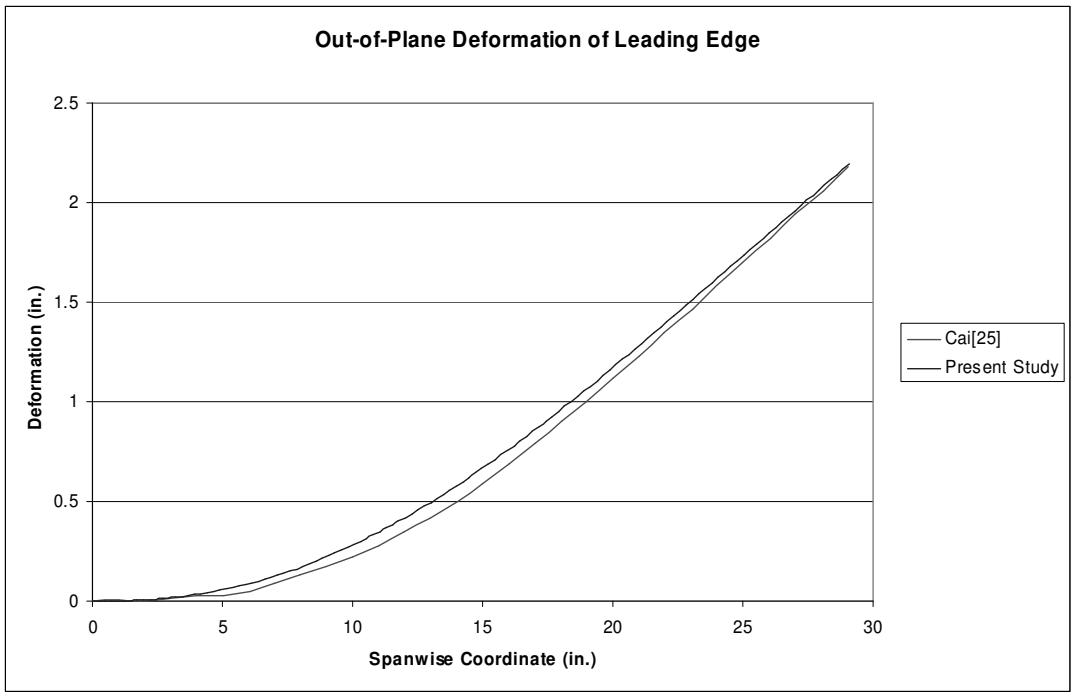

Figure 3.39 Leading Edge Out-of-Plane Deformation of AGARD Wing 445.6

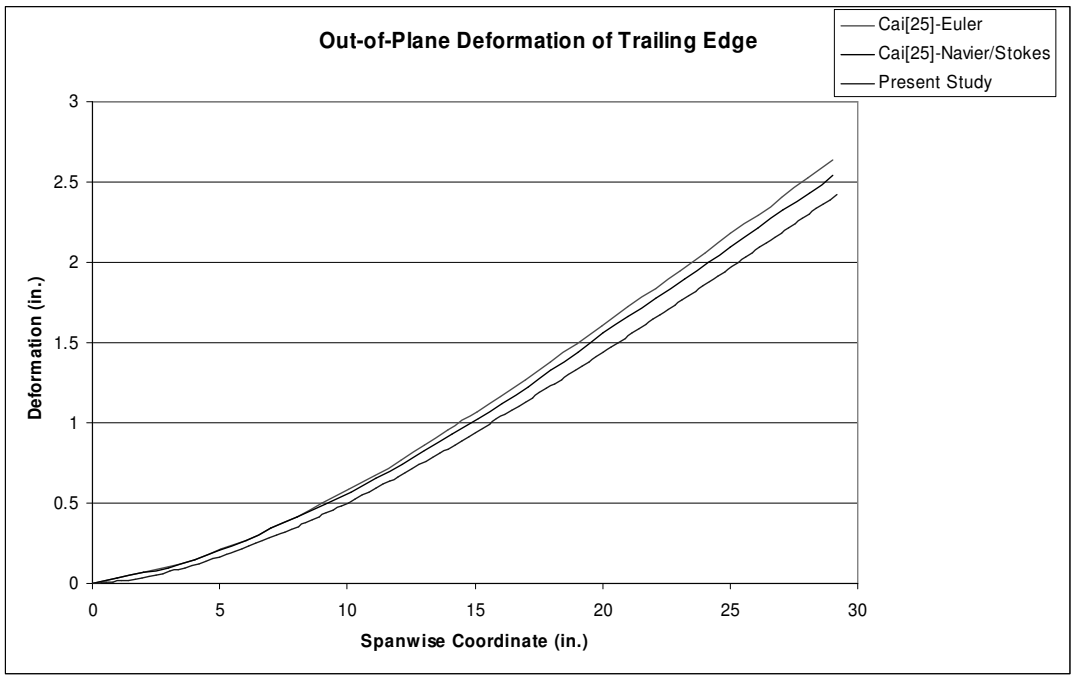

Figure 3.40 Trailing Edge Out-of-Plane Deformation of AGARD Wing 445.6

Out-of-plane deformations at the leading edge of the wing shows agreement with the results of Cai [25] with a maximum percent error of 18 % at 43.3 % percent span as shown in Figure 3.39. However, this error is misleading because the absolute values are small in magnitude. At this location present study predicts a displacement of 0.496 in., and Cai [26] predicts a displacement of magnitude 0.419 in., which only differ by 0.077 in. in magnitude. This error decreases and eventually diminishes toward root and tip of the wing. It should be noted that Cai [25] uses modal structural equations rather than a 3D finite elements in order to compute deformation of the wing. In addition Cai [25] regarded the fluid and structure equations as one single system of time dependent equations in time and solved them by time marching methods until a steady state is reached which makes the solution method fully coupled.

Out-of-plane deformations at the trailing edge of the wing show good agreement with the results of Cai [25] as shown in Figure 3.40. The maximum error occurs in the wing tip, and is 4.7 % for Cai [25] Navier-Stokes solution and 8.3 % for Cai [25] Euler solution.

As well as aerodynamic parameters and structural deformations, stress information is also available from the finite element model of the wing. This stress information would be valuable in stress analysis of a wing under the action of aerodynamic loads at a prescribed flow condition where design may be of interest. Equivalent Von-Misses stress distribution of AGARD Wing 445.6 is given in Figure 3.41

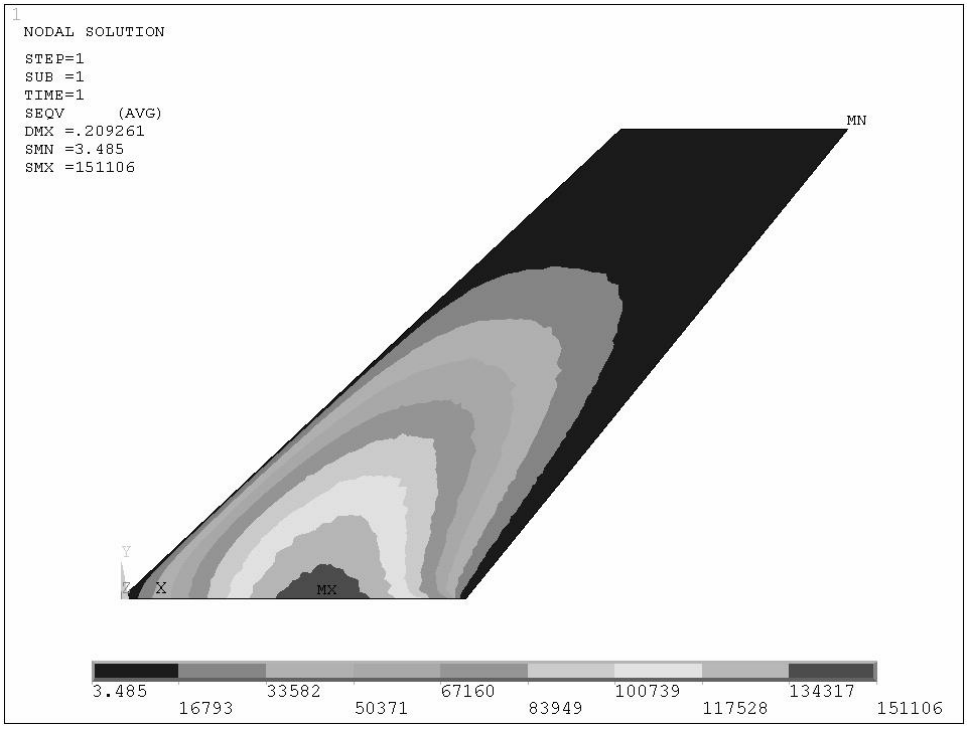

Figure 3.41 Equivalent Von-Misses Stress Distribution on AGARD Wing 445.6 (Stress values are in lbf/ft^2)

The structural and grid deformation calculations are done on a single processor with Intel Xeon 3.0 processor and the CFD calculations are done in a parallel computing environment with 16 nodes. Each of the nodes has an Intel Pentium 2.4 processor. One aeroelastic iteration for the case of AGARD Wing 445.6 takes about 20 minutes and 80% of this time is spent for grid deformation calculations.

CHAPTER 4

TEST CASE I – AGARD WING 445.6

4.1 INTRODUCTION

In this chapter the present method is applied to solve static aeroelastic characteristics of ARW-2. The ARW-2 is a large elastic wing which has an aspect ratio of 10.3 with a leading-edge sweep angle of 28.8^{o} and a supercritical airfoil. The planform geometry of the wing is given in Figure 4.1. Steady pressure measurements were conducted on an elastic semispan wing model at Langley TDT [27, 28, 29, 30, and 31].

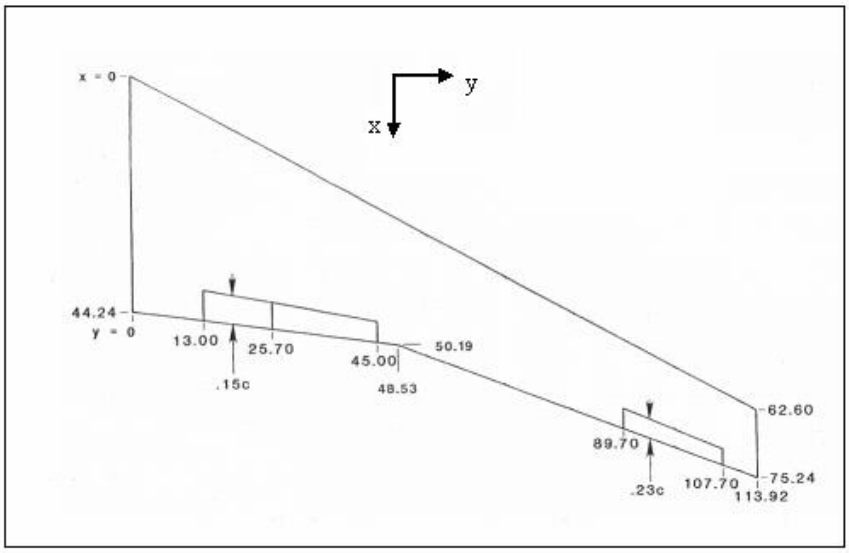

Figure 4.1 ARW-2 Wing Planform (All dimensions are in inches)

4.2 ARW-2 WIND TUNNEL MODEL DEFINITION AND STRUCTURAL PROPERTIES

4.2.1 Wind Tunnel Model

The elastic semispan wind tunnel model consisted of right wing panel from the DAST ARW-2 drone flight vehicle and a rigid half body fuselage. Both the fuselage and the wing were mounted on a remotely controlled turntable mechanism. The half body fuselage was used primarily to place the wing outside the wind tunnel wall boundary layer.

Originally the wing contour was formed from three supercritical airfoil shapes with different thickness-to-chord ratios. Straight-line interpolations along constant percent chords are used to define the area between the three airfoil shapes. This wing contour was the desired shape for a loaded wing associated with level flight with a cruise Mach number of 0.8 at an altitude of 46800 ft. However, an elastic wing deforms to a different shape, known as the jig shape, if all aerodynamic loads and vehicle loads are removed Sanford [45]. In the present study the jig shape airfoil coordinates for ten different span locations given in Sanford [45] is used to model wing geometry.

The semispan wing consisted of a carry-through section, which attached to the sidewall turntable and a wing panel, which attached to the carry-through section near the edge of the fuselage shell. The carry-through section was machined from a 4-inch-thick block of aluminum

4.2.2 Wing Structural Properties

The wing primary structure consisted of a front spar at 25 % of local chord and a rear spar at % 62 local chord. Ribs were placed perpendicular to rear spar every 13.2 in The spars and ribs were machined from 7075-T73 aluminum alloy. The

wing skin was made of fiberglass material with honeycomb panels sandwiched between the middle two layers. The number of layers of fiberglass used to make the skin varied from 36 at the inboard end to 27 at the outboard end [28, 45]. Measured bending and torsion stiffness distributions of the wing are given in Fig 4.2 together with calculated stiffness values using the finite element model given in Sanford [45].

The stiffness data were calculated from angular deflections of loaded wing. The deflections were measured with a laser light source and set of mirrors mounted on the wing along the centerline of wing box beam (43.5 % chord). These deflection measurements also demonstrated that the 43.5 % chord line was the actual elastic axis of the wing [45].

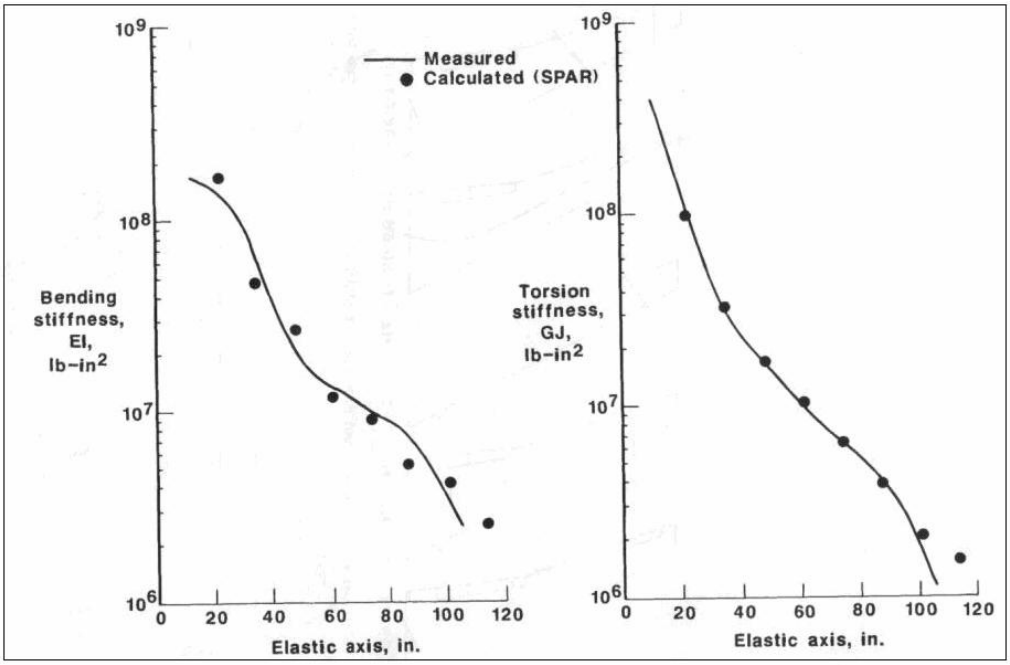

Figure 4.2 Calculated and Measured Torsion and Bending Stiffness Data [45]

4.3 ARW-2 FINITE ELEMENT MODEL

The structural properties of ARW-2 which are available in the literature are not adequate to model the wing structure. The spar web, cap thicknesses and the skin thicknesses are not provided. Moreover, details of the composite material used for the wing skin are not given. But the wing topology and the distributions of bending and torsional stiffness along the elastic axis are given. Under these limitations a 1-D and a 3-D wing model were generated using ANSYS program. Skin, spar web, spar cap and rib thicknesses in 3-D model are all defined parametrically using APDL. Modeling is based mainly on the given torsional and bending stiffness distribution of the wing and the location of the elastic axis.

4.3.1 1-D Finite Element Model of the Wing

A 1-D finite element model of the wing was created based on the stiffness data given in Figure 4.2. Wing torsional and bending stiffness values at 8 different span locations on the elastic axis are extracted from Figure 4.2. The stiffness values are given in Table 4.1.

Table 4.1 Bending and Torsional Stiffness Values for 1-D Finite Element Model

Distance along elastic axis measured from wing root (dea) [in]	1-D Finite Element Model; Element Number	Bending Stiffness (EI) [lb.in]	Torsional Stiffness (GJ) [lb.in]
27.62	1	1.06E+08	6.33E+07
40.84	2	3.59E+07	2.34E+07
54.13	3	1.57E+07	1.35E+07
59.77	4	1.34E+07	1.07E+07
73.87	5	9.72E+06	6.53E+06
87.24	6	6.97E+06	4.22E+06
100.51	7	3.30E+06	1.90E+06
113.76	8	2.52E+06	1.54E+06

At the wing tip, torsional and bending stiffness values are taken the same as the stiffness values at dea=113.76 in, where dea is the distance measured along the elastic axis.

The 1-D model consists of nine BEAM4 elements. The bending and torsion stiffness of each element is given in Table 4.1. The first column in Table 4.1 shows the right end of each element. One-dimensional model is shown in Fig. 4.3.

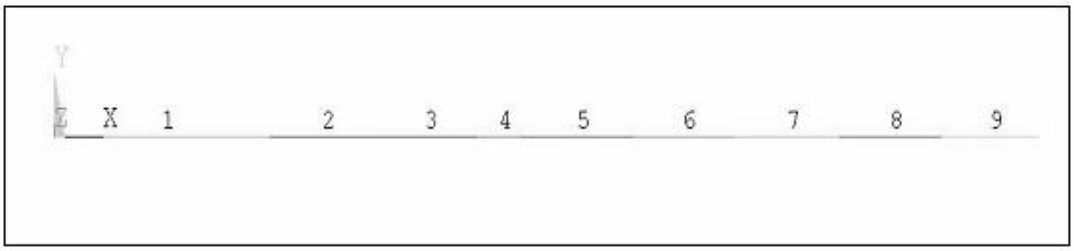

Figure 4.3 1-D Wing Finite Element Model

Finite element model is clamped at the root section (x=0). A tip load of 100 lb in y direction and a tip torque of 100 lb.in about the x-axis are applied (Fig 4.4 and Fig 4.5) and corresponding translations in y direction and rotations about the x-axis are obtained. The calculated displacement values are given in Table 4.2.

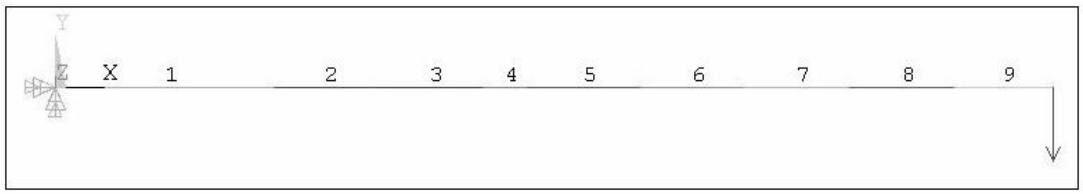

Figure 4.4 1-D Finite Element Model under 100 lb Tip Load

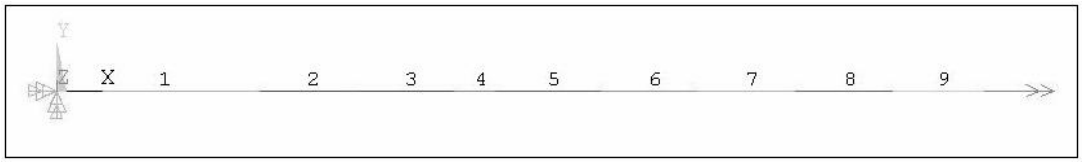

Figure 4.5 1-D Finite Element Model under 100 lb.in Tip Torque

It is assumed that the 1-D model of the wing with the above mentioned stiffness properties represent the 3-D wind tunnel model of ARW-2. The whole purpose of generating a 1-D model is to compute displacements and angles of twist result from the stiffness distributions given in Figure 4.2. The 3-D model described in the next section is calibrated using these displacements and angles of twist because a direct calibration of a stiffened box beam is difficult using the given stiffness distributions.

Table 4.2 Deflection and Angle of Twist Values for 1-D Finite Element Model

x [in]	Deflection (u_y) [in]	Angle of Twist (rot_x) [rad]
27.62	0.0419	0.000043
40.84	0.103	0.0001
54.13	0.232	0.000198
59.77	0.314	0.000251
73.87	0.605	0.000468
87.24	0.991	0.000782
100.51	1.523	0.00147
113.76	2.210	0.00233
126.22	2.939	0.00314

4.3.2 3-D Finite Element Model of ARW-2

The geometry of the ARW-2 is modeled using ANSYS, and the 3-D finite element model of the wing is created using APDL. The geometry of the ARW-2 is given in Fig. 4.6.

The wing has a front spar at 25 % local chord and a rear spar at 62 % local chord for outboard spanwise sections. There are three auxiliary spars in the inboard section which are not extended to the tip. The wing has 19 ribs including the one at the wing tip and 16 of them are perpendicular to the rear spar. The line between front spar and rear spar represents the elastic axis of the wing.

The finite element model of the wing, which is given in Figure 4.7, consists of 12595 SHELL63 elements and 516 BEAM4 elements.

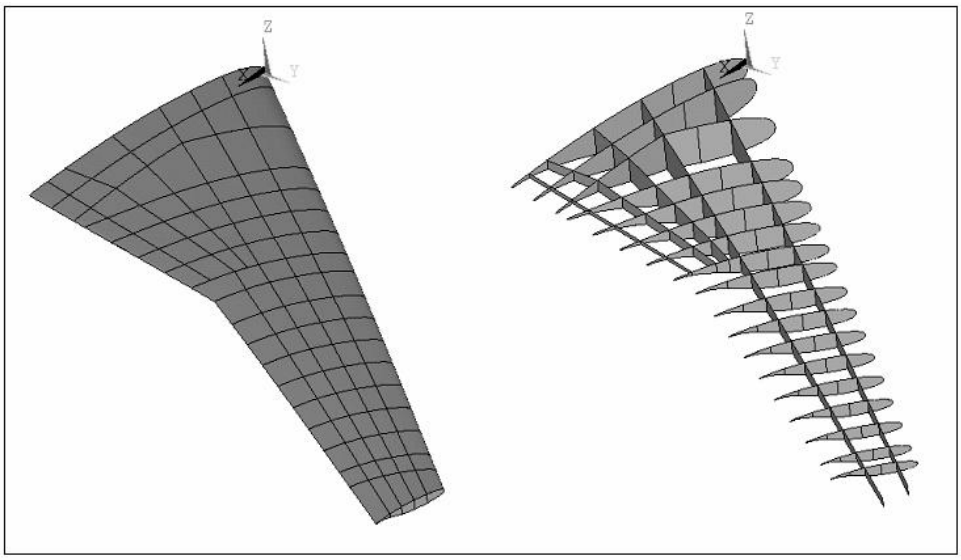

Figure 4.6 3-D Wing Geometry

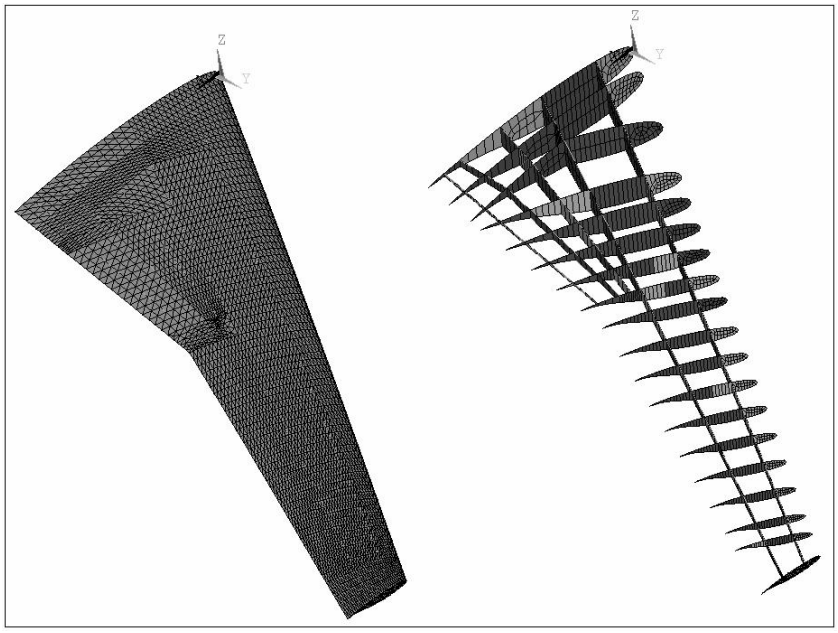

Figure 4.7 3-D Wing Finite Element Model

In order to have similar deformation characteristics with the actual ARW-2 wing, the finite element model has to satisfy the following criteria:

- Elastic axis has to be located at % 43.5 local chord

- At least the displacement and rotation values at the given locations in Table 4.2 has to be obtained upon the application of a tip load at and torque about the elastic axis respectively.

Check for Location of the Elastic Axis

The method for checking the location of the elastic axis comes from the definition:

EACheck 1: If the point of application of a force is on the elastic axis of a slender swept beam then this load does not produce any torsional twist.

In order to perform this check a tip load in z-direction is applied to the 3-D finite element model of the wing on the expected elastic axis. Nodal displacement values in z direction at the leading and trailing edge of eight different sections and the error defined by Eqn (4.1) are obtained from the finite element analysis.

$$checkb_i = \frac{\left|uzft_{te}\right|_i - \left|uzft_{le}\right|_i}{\left|uz_{ea}\right|} x100 \qquad i = 1..8 \tag{4.1}$$

where

$|uzft_{te}|_i$ = Absolute value of the displacement in z direction at the trailing edge of section i upon the application of a tip load of 100 lb on the assumed elastic axis of 3-D Wing model

$|uzft_{le}|_i$ = Absolute value of the displacement in z direction at the leading edge of section i upon the application of a tip load of 100 on at the assumed elastic axis of 3-D Wing model

$|uz_{ea}|$ = Absolute value of the displacement at the assumed elastic axis.

$Checkb_i$ = Relative angle of twist error in bending

EACheck 2: If a torque is applied about the elastic axis then this torque does not produce any translation on the elastic axis.

In order to perform this check a tip torque is applied about the expected elastic axis of 3-D wing model. Nodal displacement values in z direction at the leading and trailing edge of eight span locations and the error, which is defined by Eqn. (4.2), are obtained from the finite element analysis.

$$checkt_i = \frac{\left|uz_{ea}\right|}{\left|uztt_{te}\right|_i + \left|uztt_{le}\right|_i} x100 \qquad i = 1..8 \tag{4.2}$$

$|uztt_{te}|_i$ = Absolute value of the displacement in z direction at the trailing edge of section i upon the application of a tip torque of 100 lb.in about the assumed elastic axis of 3-D Wing model

$|uztt_{le}|_i$ = Absolute value of the displacement in z direction at the leading edge of section i upon the application of a tip torque of 100 lb.in about the assumed elastic axis of 3-D Wing model

$|uz_{ea}|$ = Absolute value of the displacement at the assumed elastic axis.

$Checkt_i$ = Relative bending deflection error in torsional loading

Check for Wing Model Torsion and Bending Characteristics

In order to match the stiffness properties of the finite element model with the wind tunnel model, a tip load of 100 lb is applied to the 3-D finite element model (Fig 4.8). The resulting displacements at eight different spanwise locations are compared with the results obtained from the 1-D finite element model. Similarly 100 lb.in tip torque is applied along the elastic axis and resulting rotations are compared with those of 1-D model. In both loading conditions, the nodes at root section between front spar and rear spar are clamped.

By changing the skin thickness, spar web and spar cap thickness values, the translation and rotation values given in Table 4.2 are approached.

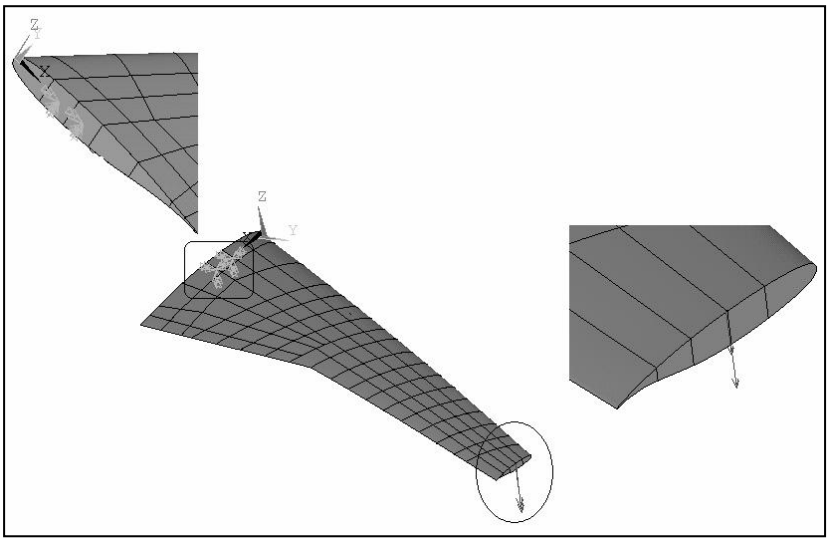

Figure 4.8 3-D Wing Model with 100 lb Load at the Tip.

A trial and error approach is implemented in order to match characteristics of our model with that of the wind tunnel model. Results are given in Tables 4.3-4.6.

Table 4.3 Comparison of Bending Deflections of 1-D Model and 3-D Model.

Spanwise section	1-D model displacements [in]	3-D model elastic axis displacements [in]	Percent error [%]
1	0.0419	0.0413	1.432
2	0.103	0.1029	0.097
3	0.232	0.2335	0.647
4	0.314	0.3196	1.783
5	0.605	0.6065	0.248
6	0.991	1.0136	2.281
7	1.523	1.5472	1.589
8	2.210	2.1988	0.507

Table 4.4 Comparison of Angle of Twist of 1-D Model and 3-D Model

Spanwise section	1-D model twist[rad]	3-D model twist [rad]	Percent error [%]
1	0.000043	0.000025	41.86
2	0.0001	0.000065	35.00
3	0.000198	0.000159	19.96
4	0.000251	0.000194	22.70
5	0.000468	0.000347	25.85
6	0.000782	0.000580	25.83
7	0.00147	0.000874	40.54
8	0.00233	0.00132	43.34

Table 4.5 Relative Angle of Twist Error in Bending

Spanwise section	Checkb [%]
1	27.7
2	13.7
3	8.5
4	5.9
5	3.0
6	1.4
7	0.5
8	0.03

Table 4.6 Relative Bending Deflection Error in Torsion

Spanwise section	Checkt [%]
1	26.3
2	10.8
3	10.1
4	9.5
5	8.4
6	7.8
7	6.8
8	5.9

The bending deflections of 3-D wing model are close to deflections of 1-D model. The maximum discrepancy between two models occurs at the 6^{th} spanwise section and the corresponding percent error is 2.28 as seen in Table 4.3. On the other hand the torsional deformations of 3-D wing model are small when compared to 1-D model and a maximum percent error of 43.83 occurs at the 8^{th} spanwise section as

seen in Table 4.4. Torsional rigidity of the 3-D model is higher than the actual wing. It can be reduced by decreasing the thickness of the skin panels, but skin panels then deform too much under the action of the distributed pressure force over the surface of the wing.

The two checks for the location of the elastic axis reveal that the elastic axis of the present study model is not at the desired location for the sections that are close to the wing root. This error in the location of the elastic axis is expected since the actual boundary conditions at the wing root was not given in the literature, so it cannot be reflected to the wing model of the present study.

4.4 ARW-2 COMPUTATIONAL FLUID DYNAMICS MODEL

For the solution of the flow over ARW-2 model an unstructured volume grid is formed. The dimensions of solution domain are given in Figure 4.9.

The surface mesh is formed by using the mapped surface triangulation option of ANSYS program except for four areas near the wing break section. The computational mesh has 11248 boundary faces and 5661 boundary nodes. Wing surface triangulation is shown in Figure 4.10.

The volume grid, which is shown in Figure 4.11, contains 59307 field nodes and 330941 field elements.

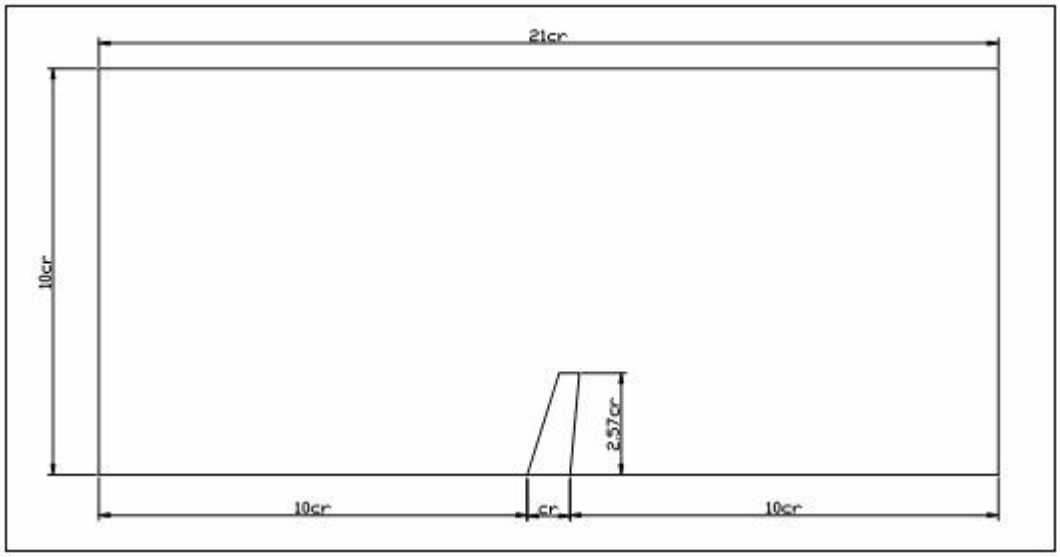

Figure 4.9 Dimensions of the Computational Domain.

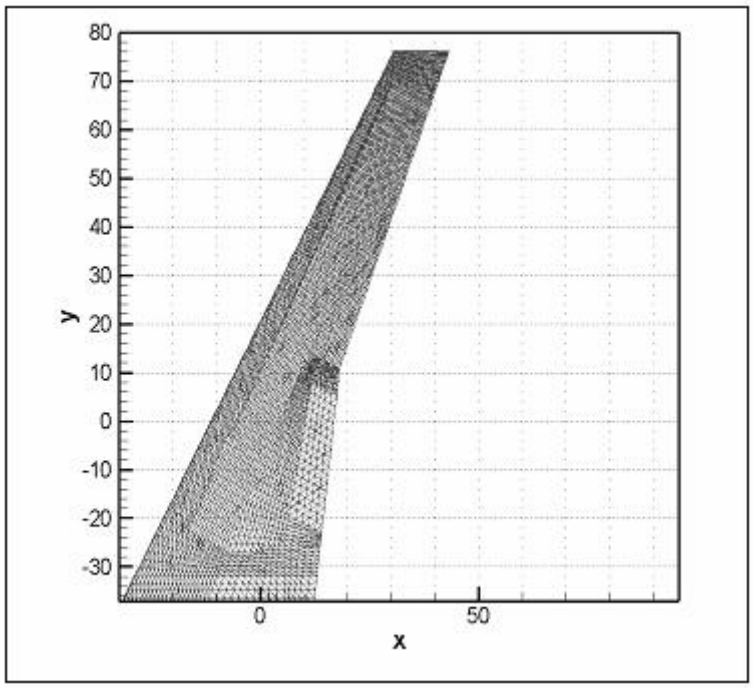

Figure 4.10 Wing Surface Triangulation

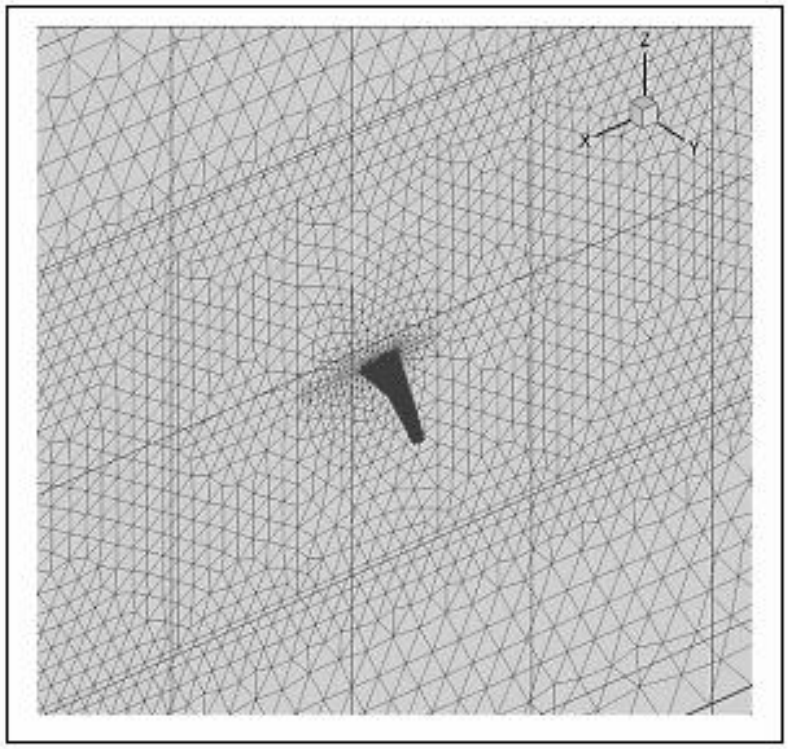

Figure 4.11 Unstructured Volume Grid.

4.5 ARW-2 STATIC AEROELASTIC ANALYSIS

The aeroelastic solution is obtained similarly to that of AGARD Wing 445.6.The rms of wing displacements in z direction falls below 0.00001 after 12 aeroelastic iterations, which corresponds to 1200 CFD time step. Computations are done at M_∞=0.8, q_∞=100 psf and $\alpha=0^o$ flow condition. Lift coefficient for rigid and elastic wings is plotted against CFD time step in Figure 4.12, and convergence history for rigid and elastic wings is given in Figure 4.13; the spike at 3000 iterations is due to the start of aeroelastic iterations.

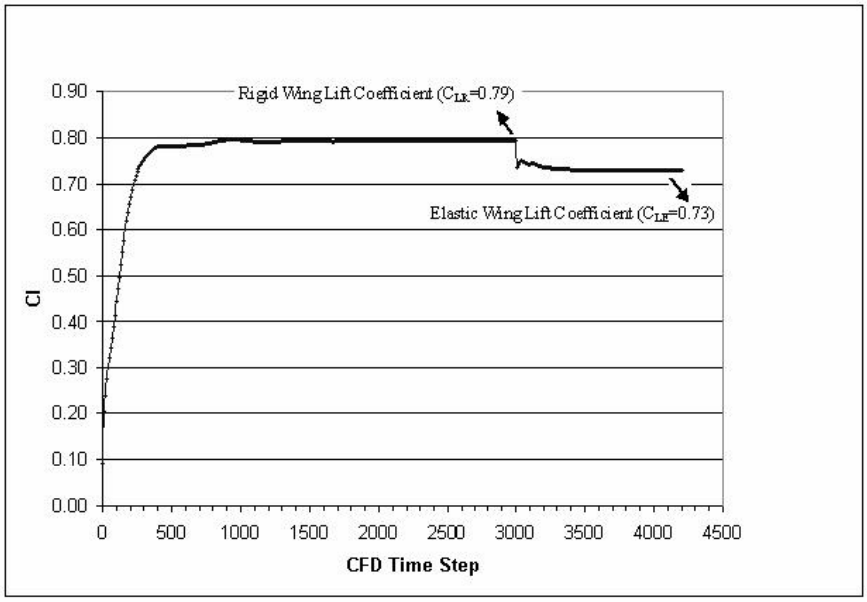

Figure 4.12 Lift Coefficients for Rigid and Elastic Wings.

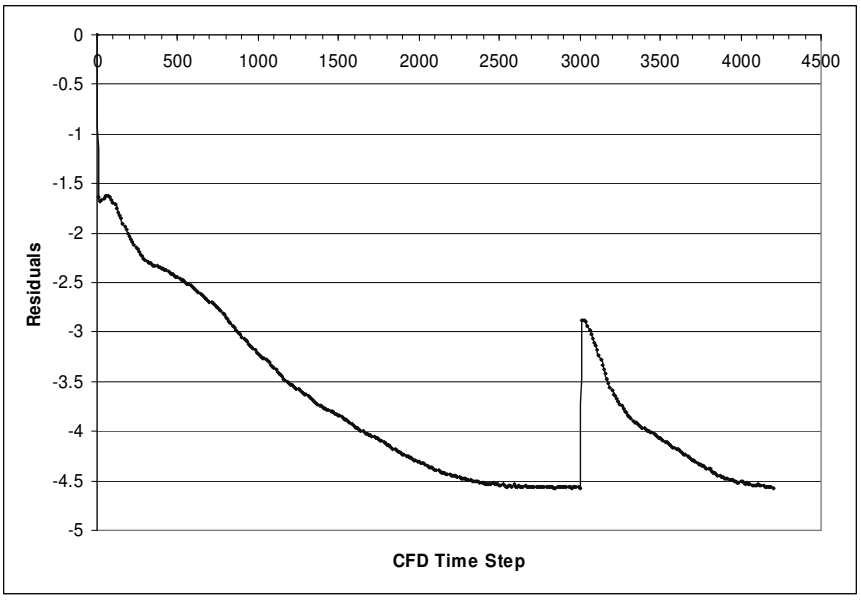

Figure 4.13 Convergence History for Rigid and Elastic Wings

The non-dimensional pressure contours over the rigid and elastic wings are given in Figures 4.14-4.15. A comparison of wind tunnel pressure coefficient data at six different span locations with that of rigid and elastic wings are given in Figure 4.16-4.21.

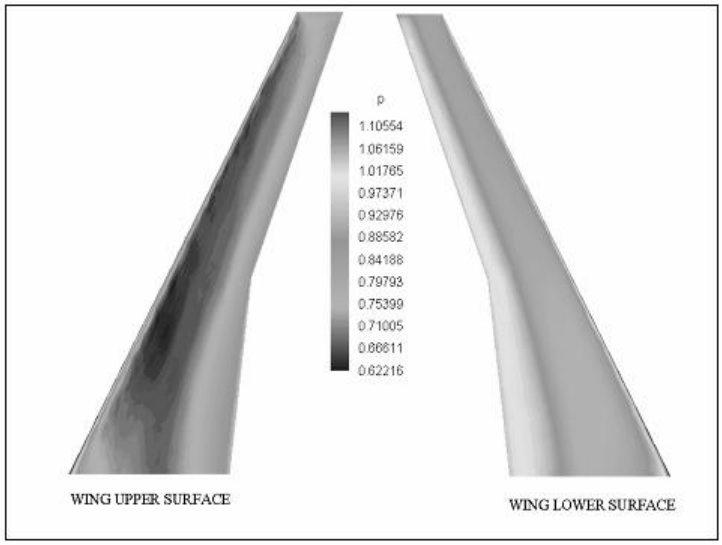

Figure 4.14 Non-dimensional Pressure Contours over Rigid Wing

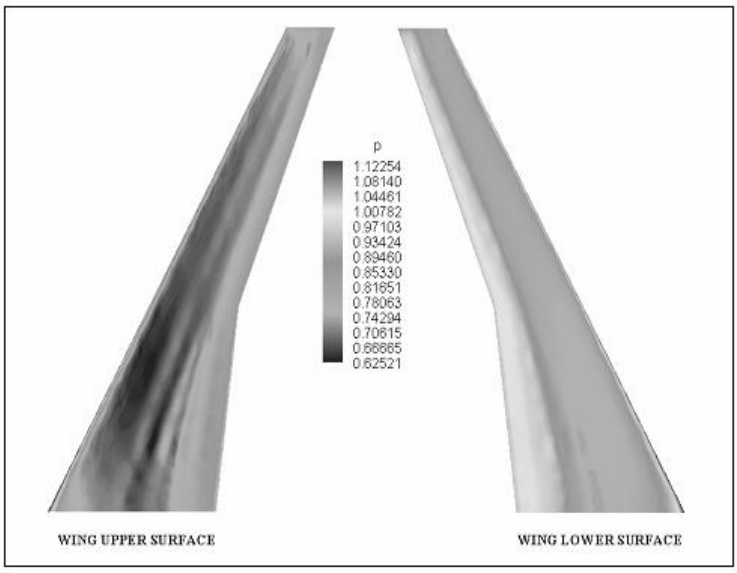

Figure 4.15 Non-dimensional Pressure Contours over Elastic Wing

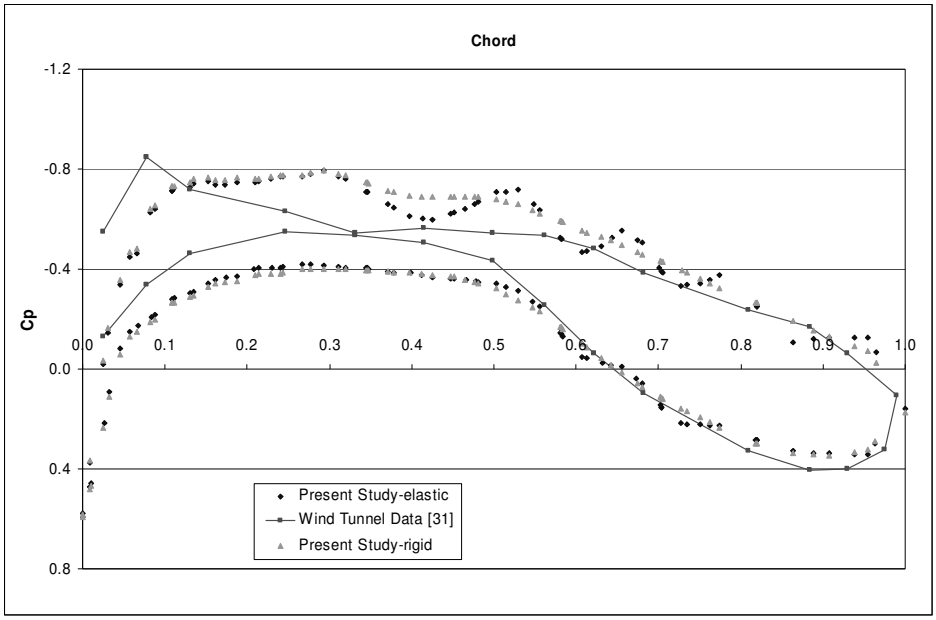

Figure 4.16 Pressure Coefficient Distributions at 23.4% Semispan

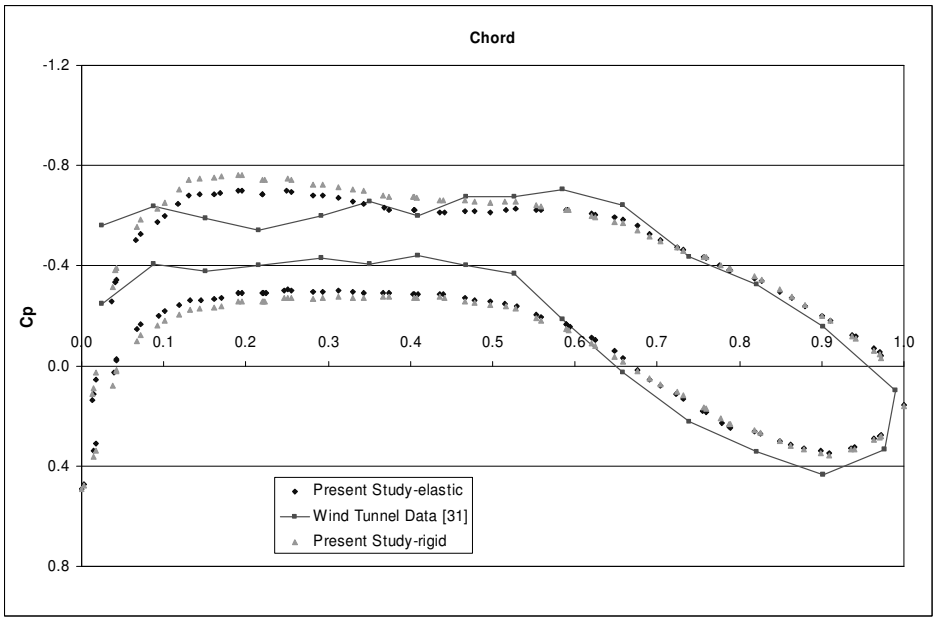

Figure 4.17 Pressure Coefficient Distributions at 47.6 % Semispan

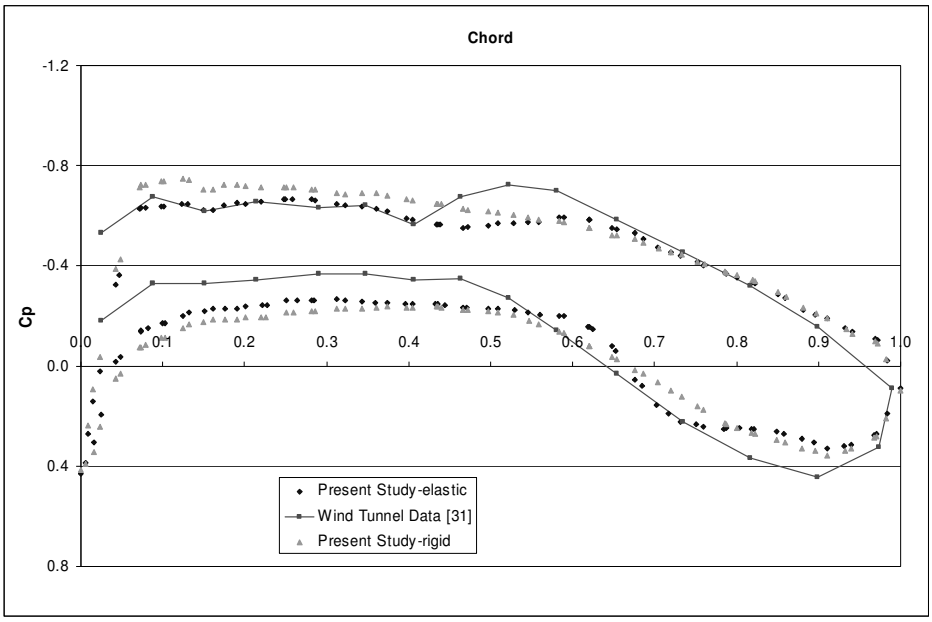

Figure 4.18 Pressure Coefficient Distributions at 59.9 % Semispan

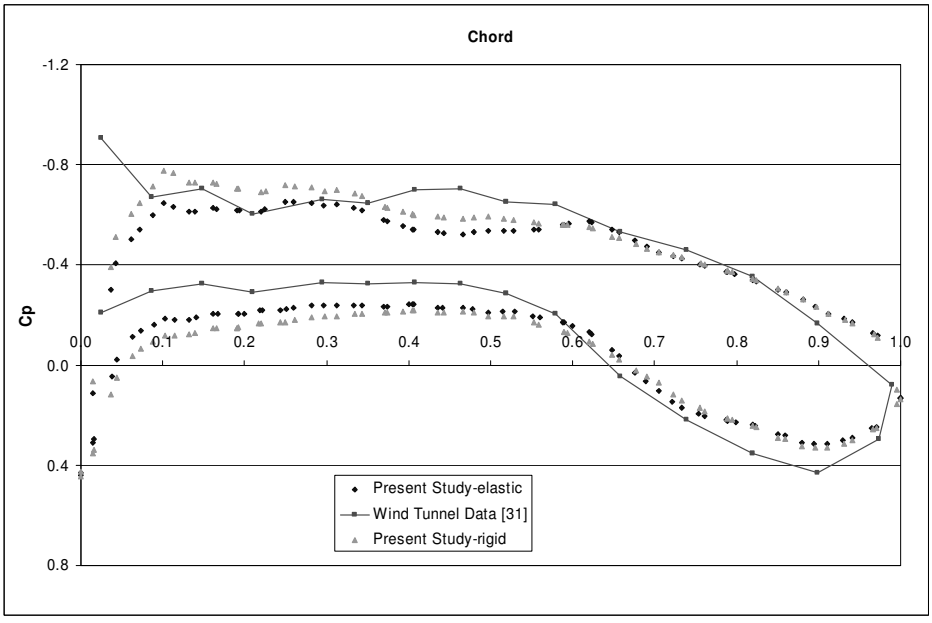

Figure 4.19 Pressure Coefficient Distributions at 70.7 % Semispan

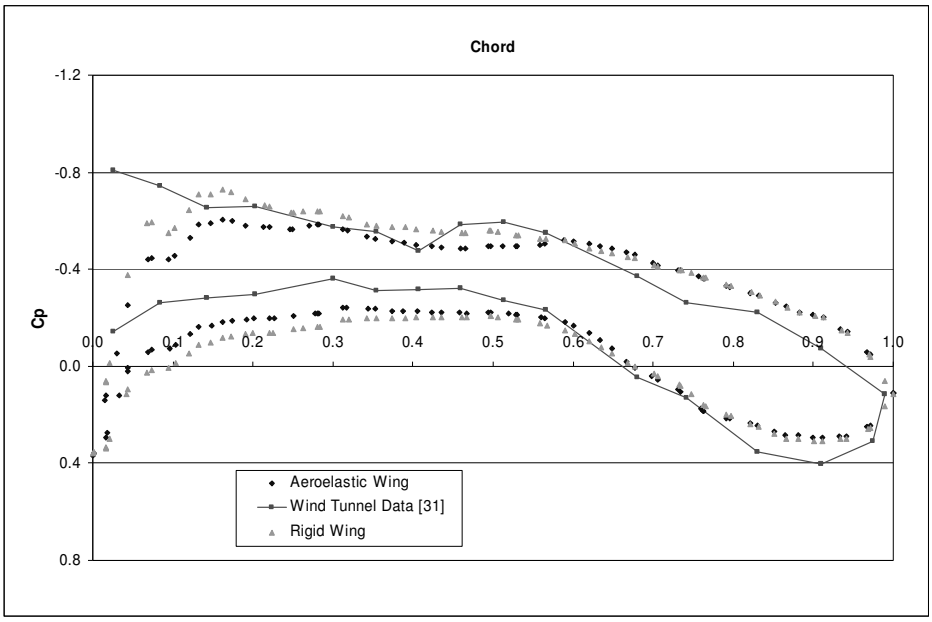

Figure 4.20 Pressure Coefficient Distributions at 87.1 % Semispan

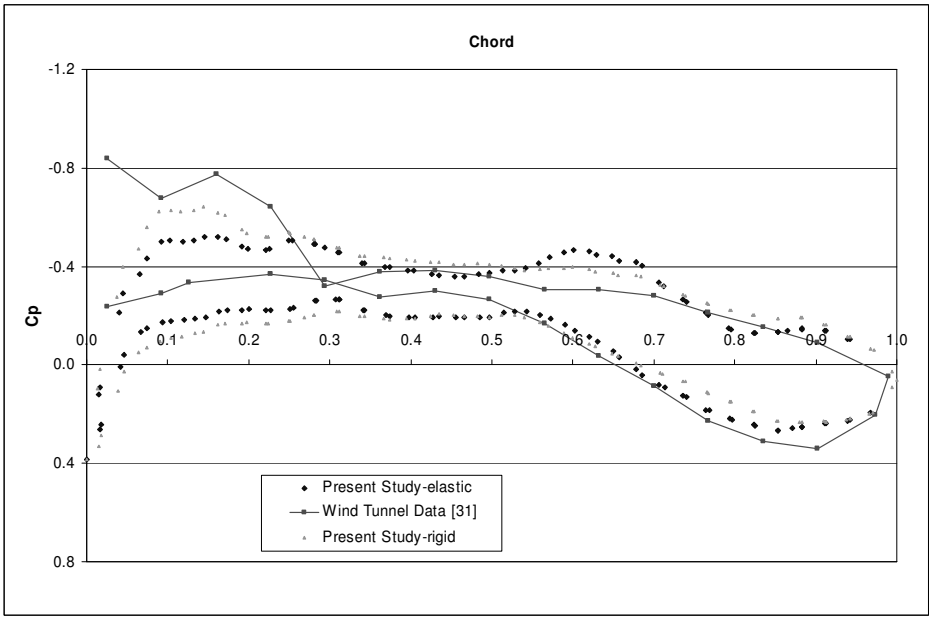

Figure 4.21 Pressure Coefficient Distributions at 97.2 % Semispan

In the present study, elastic and rigid wing pressure distributions are nearly the same at all spanwise sections. The elastic wing pressure distribution is below the rigid wing pressure distribution. The elastic wing pressure distribution is different from that of the wind tunnel model, but general trends of the curves are similar. This discrepancy in the results is expected because the effect of viscosity is neglected by using Euler Equations. Another influencing factor is that the fuselage geometry to which the wing is attached is not modeled in the present study. The high torsional rigidity of the present study wing model may also have some minor effect on the pressure distribution over the elastic wing. Three dimensional views of rigid and elastic wings are given in Figures 4.22-4.23.

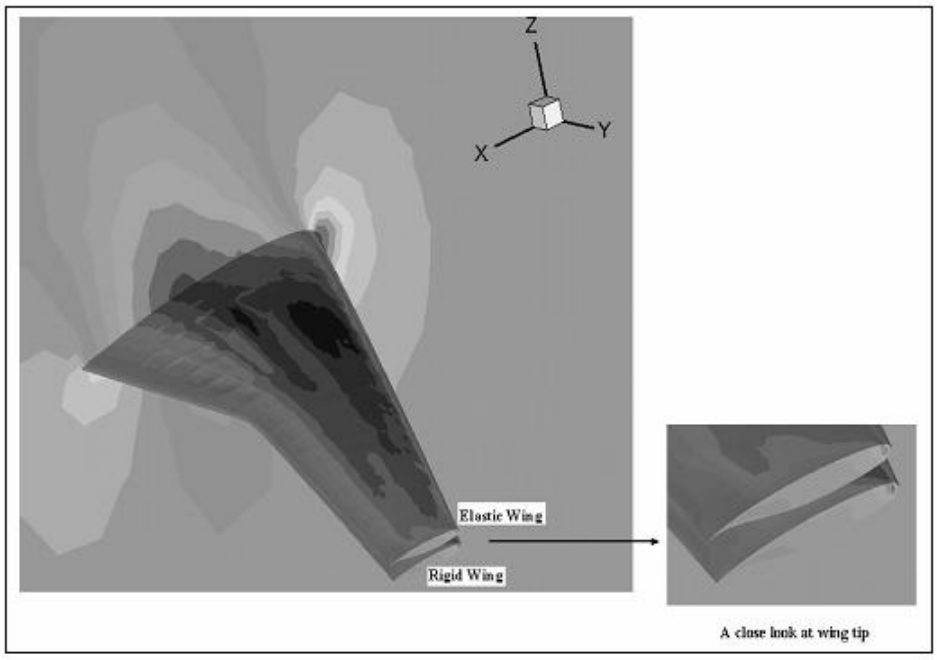

Figure 4.22 Initial and Equilibrium Positions of ARW-2

Figure 4.23 Initial and Equilibrium Positions of ARW-2 (View from Trailing Edge)

The front and rear spar shapes of wind-off (w.o.) ARW-2 and the same shapes at M_∞= 0.8, q_∞=100 psf and $\alpha=0^o$ are given by Byrdsong [30]. The difference between the two represents the effect of the flow. The comparison of rear and front spar shapes of the present study elastic wing with those of ARW-2 are given in Figure 4.24 and Figure 4.25. The wind-off shapes of the present study are the same as those of Byrdsong [30].

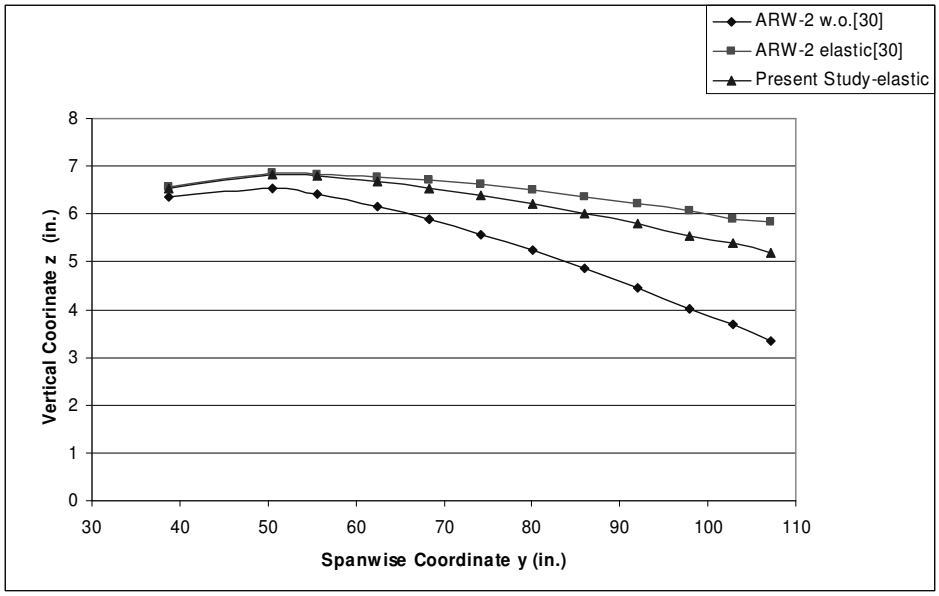

Figure 4.24 Comparison of Front Spar Shapes M=0.8 q_∞=100 psf $\alpha= 0^o$

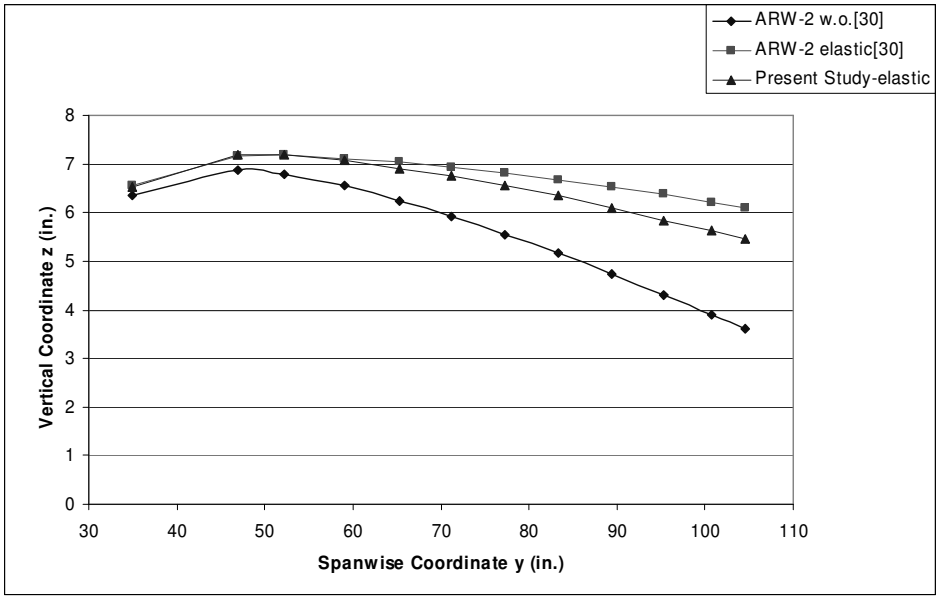

Figure 4.25 Comparison of Rear Spar Shapes M=0.8 q_∞=100 psf α= 0^o

The front spar and rear spar shapes predicted in the predicted study captures the general trend in that the rear spar is deflected more than the front spar. The shape of the front spar shows good agreement with that of Byrdsong [30] between y=38 in. and y=55 in. but the front spar shapes is different after y=55 in. and the discrepancy increases toward the tip of the wing. A percent error of 11 % occurs at y=107 in. Similarly the shape of the rear spar shows good agreement with that of Byrdsong [30] between y=35 in. and y=59 in. but difference in rear spar shapes increases towards the tip of the wing and a percent error of 10 % occurs at y=104 in. This error is acceptable and shows that the discrepancy in the torsional rigidity between our model and the wind tunnel model (Table 4.4) does not affect the results significantly. That is bending is more dominant than torsion as expected. (Our bending results are very close to those of wind tunnel model as seen in Table 4.3.

CHAPTER 5

CONCLUSION AND RECOMMENDATIONS

In this study a loosely coupled aeroelastic solution procedure has been developed, validated and applied to complex wing geometry. In this procedure the flow field over wing surfaces is solved using a 3-D Euler solver in a parallel computing environment and the static deformations of wing structures are solved using the commercial finite element solver, ANSYS. A grid deformation method is developed which takes the entire CFD domain as an isotropic elastic medium and deforms it based on the deformation of underlying wing structure. A matching discrete interface is defined and load and motion transfer are accomplished at this interface. Since the fluid and the structure grids show one-to-one correspondence at the interface, there was no need to use interpolating algorithms to transfer nodal structural displacements to fluid grid points, motion is transferred directly. Non-dimensional pressure values at fluid grid points at fluid/structure interface are made dimensional and applied directly to the nodes of the finite element models using SF and SFFUN commands of ANSYS.

A PERL script was written which called the structure, fluid and grid deformation solvers repeatedly until rms of structural displacements fall below a prescribed tolerance.

AGARD Wing 445.6 was modeled and solved with the present method and the results were compared with a numerical study. The wing was made up of laminated mahogany, which was modeled as an orthotropic material. All major trends of Cp

distribution over the elastic wing and leading edge and trailing edge displacements are captured using the developed computational aeroelastic procedure. A downwash occurs at the wing tip and as expected, bending deflection reduces the lift, lift coefficient of elastic wing turns out to be 12.5 % lower than that of rigid wing.

Elastic wing pressure coefficient distributions agree well with the results of Cai [25] except for a very narrow region at the leading edge. Elastic lift coefficient predicted by the present study is well suited to results of Cai [25]. Small differences exist at the predicted leading and trailing edge displacements, which comes from the structural modeling of the wing structure. Wing structure is modeled using 3-D finite elements in the present study, which fully describes the wing stiffness as compared to Cai [25] modal structural equations.

As another test case, ARW-2 whose static deformations are measured previously in a wind tunnel is studied for its static aeroelastic characteristics. Since the composite wing skin material properties of ARW-2 was not well defined, an isotropic finite element model of the wing is prepared as a part of the present study based on the torsional and bending stiffness distributions of ARW-2. The wing box structure was modeled using shell and beam elements. The bending stiffness of isotropic wing model was close to ARW-2 but torsional stiffness values did not match. The location of the isotropic wing elastic axis matched with that of ARW-2 at wing sections away from the wing root. Nevertheless the static aeroelastic characteristics of the isotropic wing model was solved and compared with wind tunnel data. In the present study elastic and rigid wing pressure distributions differ slightly. The elastic wing pressure distribution is slightly below the rigid wing pressure distribution. Pressure coefficient distribution over the elastic wing is different from the wind tunnel measurements. Error is present in the pressure distribution of elastic wing; this error is expected since the effect of viscosity is neglected using Euler equations. The discrepancy in the wing torsional stiffness characteristics also affects the elastic wing pressure distribution.

Rear and front spar shapes of elastic wing predicted by the present study captured the general trends, the wing bends up and there is downwash at the tip of the wing as expected. But displacements of the wing rear and front spars are less when compared to wind tunnel model. This is expected since the isotropic wing model has a higher torsional rigidity when compared to ARW-2. Besides the discrepancies in the results, the study on the ARW-2 shows that the present method is applicable to complex built-up wings.

In the future a finite element code can be written and embedded into the flow solver for mesh deformation calculations based on the idea used in the present study; this code can be made parallel which will speed up the grid deformation calculations which take about 80 % of the computational time for a single aeroelastic iteration.

REFERENCES

1. Bisplinghoff, Raymond.L., Ashley, H., Halfman, R.L., *Aeroelasticity,* Dover Publications, Inc., Mineola, New York, Dover Edition,1996, pp 1-13.

2. Dowell, E.H., Curtiss, H.C., Scanlan, R.H., and Sisto, F., *A Modern Course in Aeroelasticity,* 2nd ed., Kluwer Academic, Boston, MA, 1989, pp 3-50.

3. Guruswamy, G.P**., "A Review of Numerical Fluids/Structures Interface Methods for Computations Using High-Fidelity Equations",** Computers and Structures ,Vol. 80, 2002, pp 31-41.

4. Zienkiewicz O.C.,The Finite Element Method, McGraw-HILL Limited, London, 1977.

5. Bennett, R.M., Edwards J.W., **"An Overview of Recent Developments in Computational Aeroelasticity",** AIAA 98-2421, Fluid Dynamics Conference, 29th, Albuquerque, NM, June 15-18, 1998.

6. Felippa, C.A., Park,K.C., Farhat, C., **" Partitioned Analysis of Coupled Mechanical Systems",** Computational Methods in Applied Mechanics and Engineering, Vol. 190, 2001, pp 3247-3270.

7. Piperno, S., Farhat, C., Larrouturou, B., **"Partitioned Procedures for the Transient Solution of Coupled Aeroelastic Problems Part I: Model Problem, Theory and Two-Dimensional Application",** Computational Methods in Applied Mechanics and Engineering, Vol. 124, 1995, pp 79-112.

8. Piperno, S., Farhat, C., Larrouturou, B., **"Partitioned Procedures for the Transient Solution of Coupled Aeroelastic Problems Part II:Energy Transfer Analysis and Three Dimensional Application",** Computational Methods in Applied Mechanics and Engineering, Vol. 190, 2001, pp 3147-3170.

9. Felker, F.F., **"A New Method for Transonic Static Aeroelasticity Problems" ,**AIAA-92-2123, AIAA Dynamics Specialists Conference, Dallas, TX, April 16, 17, 1992.

10. Felker, F.F., **"Direct Solution of Two-Dimensional Navier-Stokes Equations for Static Aeroelasticity Problems",** AIAA Journal Vol.31 No.1, January 1993.

11. Bendiksen O.O., **"A New Approach to Computational Aeroelasticity",** AIAA-91-0939, AIAA/ASME/ASCE/AHS/ASC Structures, Structural Dynamics, and Materials Conference, 32nd, Baltimore, MD, April 8-10, 1991.

12. Schuster M.D., Vadyak, J., Atta E., **"Static Aeroleastic Analysis of Fighter Aircraft Using A Three Dimensional Navier-Stokes Algorithm ",** AIAA-90-0435, Aerospace Sciences Meeting, 28th, Reno, NV, Jan. 8-11, 1990.

13. Guruswamy.G.P., Byun C., **"Fluid-Structural Interactions Using Navier-Stokes Flow Equations Coupled with Shell Finite Element Structures",** AIAA-93-3087 AIAA 24th Fluid Dynamics Conference July 6-9, 1993, Orlando,FL.

14. Guruswamy.G.P., Byun C., **"Direct Coupling of Euler Flow Equations with Plate Finite Element Structures",** AIAA Journal, Vol.33, No. 2.

15. MacMurdy D.E., Gurswamy G.P., Kapania R.K., **"Static Aeroelastic Analysis of Wings Using Euler/Navier-Stokes Equations Coupled with Wing-Box Finite Element Structures", AIAA-94-1587,** AIAA/ASME/ASCE/AHS/ASC

Structures, Structural Dynamics, and Materials Conference, 35th, Hilton Head, SC, Apr. 18-20, 1994.

16. Robinson, A.B, Batina, T.J., Yang, Y.Y.H., **" Aeroelastic Analysis of Wings Using the Euler Equations with a Deforming Mesh",** Journal of Aircraft, Vol.28, No.11, November 1991.

17. Farhat, C., Degand, C., Koobus, B., Lesoinne, M., **"Torsional Springs for Two-Dimensional Dynamic Unstructured Fluid Meshes",** Computational Methods in Applied Mechanics and Engineering, Vol.163, 1998, pp 231-245.

18. Degand, C., Farhat, C., **"A Three-Dimensional Torsional Spring Analogy Method for Unstructured Dynamic Meshes",** Computers and Structures Vol. 80,2002, pp 305-316.

19. Newman III, J.C.,Newman, P.A., Taylor III, A.C., Hou, J.C., "**Efficient Nonlinear Static Aeroelastic Wing Analysis**", Computers & Fluids Vol.28, 1999 pp 615-628.

20. Allison, D.O., Cavallo, P.A., "**Static Aeroelastic Predictions for a Transonic Transport Model Using an Unstructured-Grid Flow Solver Coupled With a Structural Plate Technique**" , NASA/TP-2003-212156.

21. Yates E.C. "**AGARD Standard Aeroelastic Configurations for Dynamic Response**", AGARD Report No.765, Meeting of the Structures and Materials Panel at Oberammergau, Germany, September,8-13,1995.

22. Lee-Rausch M.E. Batina J., "**Calculation of AGARD Wing 445.6 Flutter Using Navier-Stokes Aerodynamics**", AIAA 93-3476.

23. Sadeghi M., Yang S., Liu F., Tsai H.M., "**Parallel Computation of Wing Flutter with a Coupled Navier-Stokes/CSD Method**", AIAA 2003-1347, 41st Aerospace Sciences Meeting and Exhibit, Reno, Nevada, Jan. 6-9, 2003.

24. Li Z., "**Parallel Computation of 3D Unsteady Compressible Euler Equations with Structural Coupling**", MSc. Thesis, IUPUI , 2002.

25. Cai J., Liu F., Tsai H.M., Wong A.S.F., "**Static Aero-elastic Computation with a Coupled CFD and CSD Method**", AIAA 2001-0717, Aerospace Sciences Meeting and Exhibit, 39th, Reno, NV, Jan. 8-11, 2001.

26. Murrow, H.H., Eckstrom C.V., "**Drones for Aerodynamic and Structural Testing (DAST) – A Status Report**" Journal of Aircraft Vol.16, No.8, August 1979.

27. Seidel A.D., Sanford M.C., Eckstrom C.V., "**Measured Unsteady Transonic Aerodynamic Characteristics of an Elastic Supercritical Wing**" Journal of Aircraft Vol. 24, No.4, April 1987.

28. Seidel A.D., Eckstrom, C.V., Sanford, M.C., "**Transonic Region of High Dynamic Response Encountered on an Elastic Supercritical Wing**" Journal of Aircraft Vol.26 No.9, September 1989.

29. Eckstrom C.V., Seidel A.D., Sanford M.C., "**Unsteady Pressure and Structural Response Measurements on an Elastic Supercritical Wing**" Journal of Aircraft Vol.27 No.1, January 1990.

30. Brydsong, T.A., Richard R.A., Sanford M.C., "**Close-Range Photogrammetric Measurements of Static Deflections for an Aeroelastic Supercritical Wing**" NASA TM-4194 1990.

31. Sanford C.M., Seidel A.D. Eckstrom V.C., "**Steady Pressure Measurements on an Aeroleastic Research Wing (ARW-2)"** NASA-TM-109046 February 1994.

32. Farhat C., Geuzaine P., Brown G., "**Application of Three-Field Nonlinear Fluid-Structure Formulation to the prediction of the Aeroelastic Parameters of an F-16 Fighter**" Computers and Fluids Vol.32, 2003, pp 3-29.

33. Beckert A. "**Coupling Fluid (CFD) and Structural (FE) Models Using Finite Interpolation Elements"** Aerospace Science and Technology Vol.4, 2000, pp 13-22.

34. Farhat C., Lesoinne M., " **Two Efficient Staggered Algorithms for the Serial and Parallel Solution of Three-Dimensional Nonlinear Transient Aeroelastic Problems"** Comput. Methods Appl. Mech. Engrg., Vol.182, 2000, pp 499-515.

35. Bruner C.W.S., "**Parallelization of the Euler Equations on Unstructured Grids**" , PhD Thesis,1996, Virginia Polytechnic Institute and State University.

36. Gönç L.Ö., Tuncer İ.H., AK M.A.A., Sümer B., Başoğlu O., Işık T., " **Tübitak-SAGE'de Geliştirilen Sayısal Akışkanlar Mekaniği Yetenekleri"** Kayseri V. Havacılık Sempozyumu, 13-14 Mayıs 2004.

37. Ansys Inc Online Help Documentation.

38. Cook R.D., Malkus D.S., Plesha M.E., Concepts and Applications of Finite Element Analysis, Third Edition, John Wiley & Sons, New York,1989.

39. Batina J.T., "**Unsteady Euler airfoil Solutions Using Unstructured Dynamic Meshes",** AIAA 89-0115, AIAA 27th Aerospace Sciences Meeting, Reno, Nevada, January 9-12, 1989.

40. Farhat C., Lesoinne M.,LeTallec P., "**Load and Motion Transfer Algorithms for Fluid/Structure Interaction Problems with Non-Matching Discrete Interfaces: Momentum and Energy Conservation, Optimal Discretization and Application to Aeroelasticity**", Computer Methods in Applied Mechanics and Engineering Vol.157, 1998 pp 95-114.

41. Smith M.J., Hodges D.H., Cesnik C.E.S., "**Evaluation of Computational Algorithms Suitable for Fluid-Structure Interactions**", Journal of Aircraft Vol.37, No.2, March-April 2000.

42. Maman N., Farhat C., "**Matching Fluid and Structure Meshes for Aeroelastic Computations: A Parallel Approach**", Computers and Structures Vol.54 No.4 pp 779-785, 1995.

43. Yosibash Z., Kirby R.M., Myers K., Szabo B., Karniadakis G., "**Higher-Order Finite Elements for Fluid-Structure Interaction Problems**", AIAA 2003-1729, 44th AIAA/ASME/ASCE/AHS Structural Dynamics and Materials Conference 7-10 April 2003, Norfolk, Virginia.

44. Kolonay, R.M., "Computational Aeroelasticity", RTA-NATO The Applied Vehicle Technology Panel, 25-29 March 2002, Ankara, TURKEY.

45. Sanford M.C., Seidel D.A., Eckstrom C.V., "Geometrical **and Structural Properties of an Aeroelastic Research Wing (ARW-2)"** NASA TM-4110 1989.

APPENDIX A

ANSYS INPUT FILE FOR DEFINING THE MATERIAL PROPERTIES OF CFD COMPUTATIONAL DOMAIN

! Call the previously created CFD Domain model database

```
RESUME,arwcd13t,db,C:\12t\arw_10t\,0,0
! Define number of boundary nodes
numnode=3047
! Define number of elements
enum=297824
! Define constant C
C=50000000
! Define constant n
n=2
! Enter to the Preprocessor
/PREP7
! Open an array called “esize” with dimensions 297824x1
*DIM,esize,array,enum,1,1
! Loop over the elements and get their volumes
*do,k,1,enum
*get,esize(k),elem,k,volu
*end do
! loop over the elements define the material property for each element
*do,l,1,enum
MP,EX,l,A/(esize(l)**n)
MP,PRXY,l,0.3
*end do
*do,m,1,enum
Emodif,m,mat,m
*end do

FINISH
```

APPENDIX B

PERL SCRIPT

```
#!/usr/bin/perl

$iternum="iternum.dat";
$set3d='/home/bsumer/set3d/set3d-V11';
$input1="set3d_ansys_structural.txt";
$input2="ansys_str_set3d.txt";
$output1="ansys1.out";
$output2="ansys2.out";
$arg="surface.dat";
$tol=0.00001;
$it= 1; $go=1;
open (DAT,">$iternum")  || die ("iternum.dat could not be opened!");
print DAT "$it";
system("mkdir -p rc") ;

#  Initialize the file
open (GO,">.go");
print GO "$go";
close GO;
# assign an initial rms value

while ($go == 1 ) {
  print " ITERATION :   $it\n";
  system("ansys61 -m 2000 -db 750 -b -p ansys -i $input1 -o $output1") ;
  system("ansys61 -m 2000 -db 750 -b -p ansys -i $input2 -o $output2");
  system("$set3d > out.dat");
  system("cp ansys1.out   ./rc/a1-$it.dat");
  system("cp ansys2.out   ./rc/a2-$it.dat");
  system("cp out.dat   ./rc/out-$it.dat");
  system("cp arwstr13t.rst   ./rc/rst-$it.dat");
  system("cp rms.txt   ./rc/rms-$it.dat");
  system("cp fsd.txt   ./rc/fsd-$it.dat");
  system("cp rsd.txt   ./rc/rsd-$it.dat");
  $it  += 1;
  open (DAT,">$iternum")  || die ("iternum.dat could not be opened!");
  print DAT "$it";
  $at=$it-1;
 # print "$at";
  open (rmsf,"<rms.txt")  || die ("rms.txt could not be opened!");
```

```
 $rmsf=<rmsf>;
 close (rmsf);
 if ($at==1) {
$deltarms=$rmsf;
 }
 else {
 $deltarms=$rmsi- $rmsf;
 }
 if (abs($deltarms) <=$tol) {
 $go=0;
 }
 else {
 $go=1;
 }
  print "$deltarms";
  $rmsi=$rmsf;
  print "$rmsi"
}
```

APPENDIX C

ANSYS INPUT FILE FOR STRUCTURAL ANALYSIS

! this file is called by PERL program "ansys.pl" at every aeroelastic iteration
! until convergence

set3d_ansys_structural.txt :

! Call the previously created structural model database

RESUME ,arwstr29t2 ,db , /disk/bsumer/ARW29t,0,0

/FILNAME,arwstr29t2,1

! Enter to the preprocessor module.
/PREP7
allsel,all

! Set parameter "gamma"
gamma=1.132

! Set parameter "Po"
Po=(1.92-0.88) ! (Psi) 1.92 from nasatm109046 pg 72 0.88 from prerun

! Set parameter "a"
a=Po*gamma

! Set parameter numnode
numnode=5661

! Define an array called pressure with dimensions 5661x4
*DIM,pressure,ARRAY,numnode,4,1, , ,

! Define an array called P with dimensions 5661x1
*DIM,P,ARRAY,numnode,1,1, , ,

! Read file "pressure.dat" written by SET3d, which contains pressure values at !interface nodes in x,y,z,P format.
*VREAD,pressure(1,1),'pressure','dat',,jik,4,numnode
(4f20.10)
! Loop over interface nodes and dimensionalise pressure values at the interface !nodes

```
*do,i,1,numnode,1
P(i)=pressure(i,4)*(-a)
*enddo
```

!Use sffun and sf commands to apply pressure values on interface nodes.
! P array contains pressure values for 5661 nodes in an ordered fashion, the !first pressure value is for node number 1 and the last pressure value is for !node number 5661

```
sffun,pressure,P(1),,
sf,all,pressure
CMSEL,S,WING_INNER_AREAS
ALLSEL,BELOW,AREA
SFEDELE,all,1,PRES
allsel,all
```

! close the preprocessor

```
FINISH
```

! enter to solution module

```
/SOL

/STATUS,SOLU
```

! solve the model

```
SOLVE
```

! close solution module

```
FINISH
```

! enter to postprocessor module

```
/POST1
```

! Open an array called "disp" with dimensions 5661x3

```
*DIM,disp,array,numnode,3,1
```

!Loop over interface nodes and get calculated displacement value (ux,uy and !uz) of each node and store them to array "disp".

```
*do,k,1,numnode ,1
 *get,disp(k,1),NODE,k,U,X,,
 *get,disp(k,2),NODE,k,U,Y,,
 *get,disp(k,3),NODE,k,U,Z,,
*enddo
```

! Open a file called nwalldisp and write the calculated nodal displacements !stored to disp array in ux,uy,uz order. Obtained displacements will be used as !displacement type boundary condition in Mesh Deformation Analysis

```
*CFOPEN,'nwalldisp',' ',' '
*VWRITE,disp(1,1),disp(1,2),disp(1,3), , , , , , ,
(3f20.10)
*CFCLOS
```

! calculates the root mean square of nodal displacements in z-direction

```
 *DIM,r1,array,numnode,1,1
 *do,i,1,numnode,1
  r1(i)=disp(i,3)*disp(i,3)
 *enddo
  sum=0
 *do,n,1,numnode,1
  sum=sum+r1(n)
 *enddo
rms=sqrt(sum/5661)
```

! opens a text file "rms.txt" and writes the calculated rms value to this file.

```
  *CFOPEN,'rms.txt',' ',' '
  *VWRITE,rms
  (1f20.10)
  *CFCLOS

  *CFOPEN,'sum.txt',' ',' '
  *VWRITE,sum
  (1f20.10)
  *CFCLOS
```

! Opens an array called fsd and stores the front spar deflections in z-direction
! at 14 different locations

```
 *DIM,fsd,ARRAY,14,1,1, , ,

  KSEL,S, , ,    1581
  NSLK,S
  *get,n1,node,0,num,max
  *get,fsd1,NODE,n1,U,Z,,
  fsd(1)=fsd1
  KSEL,S, , ,   1590
  NSLK,S
  *get,n2,node,0,num,max
*get,fsd2,NODE,n2,U,Z,,
  fsd(2)=fsd2
  KSEL,S, , ,1602
```

```
NSLK,S
*get,n3,node,0,num,max
*get,fsd3,NODE,n3,U,Z,,
fsd(3)=fsd3
KSEL,S, , ,1608
NSLK,S
*get,n4,node,0,num,max
*get,fsd4,NODE,n4,U,Z,,
fsd(4)=fsd4
KSEL,S, , ,1618
NSLK,S
*get,n5,node,0,num,max
*get,fsd5,NODE,n5,U,Z,,
fsd(5)=fsd5
KSEL,S, , ,1623
NSLK,S
*get,n6,node,0,num,max
*get,fsd6,NODE,n6,U,Z,,
fsd(6)=fsd6
KSEL,S, , ,1635
NSLK,S
*get,n7,node,0,num,max
*get,fsd7,NODE,n7,U,Z,,
fsd(7)=fsd7
KSEL,S, , ,1641
NSLK,S
*get,n8,node,0,num,max
*get,fsd8,NODE,n8,U,Z,,
fsd(8)=fsd8
  KSEL,S, , ,1648
NSLK,S
*get,n9,node,0,num,max
*get,fsd9,NODE,n9,U,Z,,
fsd(9)=fsd9
  KSEL,S, , ,1661
NSLK,S
*get,n10,node,0,num,max
*get,fsd10,NODE,n10,U,Z,,
fsd(10)=fsd10

 KSEL,S, , ,1664
NSLK,S
*get,n11,node,0,num,max
*get,fsd11,NODE,n11,U,Z,,
fsd(11)=fsd11
```

```
   KSEL,S, , ,1676
NSLK,S
*get,n12,node,0,num,max
*get,fsd12,NODE,n12,U,Z,,
fsd(12)=fsd12
  KSEL,S, , ,1680
NSLK,S
*get,n13,node,0,num,max
*get,fsd13,NODE,n13,U,Z,,
fsd(13)=fsd13
  KSEL,S, , ,1484
NSLK,S
*get,n14,node,0,num,max
*get,fsd14,NODE,n14,U,Z,,
fsd(14)=fsd14
```

!Writes calculated front spar nodal displacements in z-direction to fsd.txt file

```
*CFOPEN,'fsd.txt',' ',' '
*VWRITE,fsd(1)
(1f20.10)
 *CFCLOS
```

! Opens an array called rsd and stores the rear spar deflections in z-direction !at 14 different locations

```
*DIM,rsd,ARRAY,14,1,1, , ,

KSEL,S, , ,    1579
NSLK,S
*get,n15,node,0,num,max
*get,rsd1,NODE,n15,U,Z,,
rsd(1)=rsd1

KSEL,S, , ,   1592
NSLK,S
*get,n16,node,0,num,max
*get,rsd2,NODE,n16,U,Z,,
rsd(2)=rsd2

KSEL,S, , ,1600
NSLK,S
*get,n17,node,0,num,max
*get,rsd3,NODE,n17,U,Z,,
rsd(3)=rsd3
```

```
KSEL,S, , ,1605
  NSLK,S
  *get,n18,node,0,num,max
  *get,rsd4,NODE,n18,U,Z,,
  rsd(4)=rsd4

  KSEL,S, , ,1616
  NSLK,S
  *get,n19,node,0,num,max
  *get,rsd5,NODE,n19,U,Z,,
  rsd(5)=rsd5

  KSEL,S, , ,1626
  NSLK,S
  *get,n20,node,0,num,max
  *get,rsd6,NODE,n20,U,Z,,
  rsd(6)=rsd6

 KSEL,S, , ,1633
  NSLK,S
  *get,n21,node,0,num,max
  *get,rsd7,NODE,n21,U,Z,,
  rsd(7)=rsd7

  KSEL,S, , ,1646
  NSLK,S
  *get,n22,node,0,num,max
  *get,rsd8,NODE,n22,U,Z,,
  rsd(8)=rsd8


KSEL,S, , ,1651
  NSLK,S
  *get,n23,node,0,num,max
  *get,rsd9,NODE,n23,U,Z,,
  rsd(9)=rsd9

    KSEL,S, , ,1659
  NSLK,S
  *get,n24,node,0,num,max
  *get,rsd10,NODE,n24,U,Z,,
  rsd(10)=rsd10


   KSEL,S, , ,1667
```

```
NSLK,S
*get,n25,node,0,num,max
*get,rsd11,NODE,n25,U,Z,,
rsd(11)=rsd11

KSEL,S, , ,1674
NSLK,S
*get,n26,node,0,num,max
*get,rsd12,NODE,n26,U,Z,,
rsd(12)=rsd12

  KSEL,S, , ,1683
NSLK,S
*get,n27,node,0,num,max
*get,rsd13,NODE,n27,U,Z,,
rsd(13)=rsd13


  KSEL,S, , ,1488
NSLK,S
*get,n28,node,0,num,max
*get,rsd14,NODE,n28,U,Z,,
rsd(14)=rsd14
```

!Writes calculated rear spar nodal displacements in z-direction to rsd.txt file

```
 *CFOPEN,'rsd.txt',' ',' '
*VWRITE,rsd(1)
(1f20.10)
 *CFCLOS
```

APPENDIX D

ANSYS INPUT FILE FOR CFD GRID DEFORMATION ANALYSIS

! Call the previously created Computational Domain Database

RESUME,arwcd29t_mpok,db,/disk/bsumer/ARW29t,0,0
/FILNAME,arwcd29t_mpok,1

! set the number of boundary nodes
numnode=5661

!set the number of field elements
enum=330941

!set the number of field nodes
na=59307

/CONFIG,NOELDB,1
/PREP7
! open an array called "disp" with dimensions 5661x3
*DIM,disp,ARRAY,numnode,3,1, , ,

! read the file "nwalldisp" and store it into "disp" array
*VREAD,disp(1,1),'nwalldisp',,,jik,3,numnode
(3f20.10)
! assign displacements to boundary nodes.
*do,m,1,numnode,1

NSEL,S, , ,m

D,all, ,disp(m,1), , , ,UX, , , , ,

D,all, ,disp(m,2), , , ,UY, , , , ,

D,all, ,disp(m,3), , , ,UZ, , , , ,

*enddo

```
allsel,all

FINISH
```

! Enter to Solution Module.

```
/SOL

ANTYPE,0

OUTRES,ERASE

OUTRES,NSOL,LAST


EQSLV,PCG,1E-4

SOLVE
```

! Open an array called "ndisp" with dimensions 59307x3 and store the nodal !displacement values into this array

```
*DIM,ndisp,array,na,3,1        ! opens an array called na

*do,k,1,na ,1

*get,ndisp(k,1),NODE,k,U,X,,

*get,ndisp(k,2),NODE,k,U,Y,,

*get,ndisp(k,3),NODE,k,U,Z,,

*enddo
```

! Open a file called "ndisp.dat" and write the nodal displacement values

```
*CFOPEN,'ndisp','dat',' '

*VWRITE,ndisp(1,1),ndisp(1,2),ndisp(1,3), , , , , , ,
(3f20.10)

*CFCLOS

FINISH
```